MODELING OF THE HAWKMOTH WING AND ITS IMPLEMENTATION IN A FOUR-BAR FLAPPING WING MECHANISM

A THESIS SUBMITTED TO
THE GRADUATE SCHOOL OF NATURAL AND APPLIED SCIENCES
OF
MIDDLE EAST TECHNICAL UNIVERSITY

BY

AYTEK ALTUGA ÖKMEN

IN PARTIAL FULFILLMENT OF THE REQUIREMENTS
FOR
THE DEGREE OF MASTER OF SCIENCE
IN
AEROSPACE ENGINEERING

FEBRUARY 2022

Approval of the thesis:

MODELING OF THE HAWKMOTH WING AND ITS IMPLEMENTATION IN A FLAPPING WING MECHANISM

submitted by **AYTEK ALTUGA ÖKMEN** in partial fulfillment of the requirements for the degree of **Master of Science in Aerospace Engineering, Middle East Technical University** by,

Prof. Dr. Halil Kalıpçılar
Dean, Graduate School of **Natural and Applied Sciences** _____

Prof. Dr. Serkan Özgen
Head of the Department, **Aerospace Engineering, METU** _____

Prof. Dr. Dilek Funda Kurtuluş
Supervisor, **Aerospace Engineering, METU** _____

Assist. Prof. Dr. Kutluk Bilge Arıkan
Co-Supervisor, **Mechanical Engineering, TEDU** _____

Examining Committee Members:

Prof. Dr. Ozan Tekinalp
Aerospace Engineering, METU _____

Prof. Dr. Dilek Funda Kurtuluş
Aerospace Engineering, METU _____

Assist. Prof. Dr. Kutluk Bilge Arıkan
Mechanical Engineering, TEDU _____

Assist. Prof. Dr. Ali Emre Turgut
Mechanical Engineering, METU _____

Assoc. Prof. Dr. Munir Elfarra
Aerospace Engineering, Yıldırım Beyazıt University _____

Date: 07.02.2022

I hereby declare that all information in this document has been obtained and presented in accordance with academic rules and ethical conduct. I also declare that, as required by these rules and conduct, I have fully cited and referenced all material and results that are not original to this work.

Name, Last Name: Aytek Altuga Ökmen

Signature:

ABSTRACT

MODELING OF THE HAWKMOTH WING AND ITS IMPLEMENTATION IN A FLAPPING WING MECHANISM

Ökmen, Aytek Altuga
Master of Science, Aerospace Engineering
Supervisor: Prof. Dr. Dilek Funda Kurtuluş
Co-Supervisor: Asst. Prof. Dr. Kutluk Bilge Arıkan

February 2022, 105 pages

The main aim of this study is to accurately model the wing of a hawkmoth (Manduca sexta) to implement it in a flapping wing mechanism for a micro aerial vehicle (MAV). The wing is first modeled in ANSYS/SpaceClaim then the model is verified by performing modal analysis on the finite element model (FEM) of the wing in ANSYS/Mechanical. Grid refinement study is performed on the FEM. Results of the modal analysis of the modeled wing are compared to literature results and it is seen that both results are in good agreement. A simple planar four-bar mechanism is designed in the flexible multibody dynamics program ADAMS. The mechanism can perform a figure of eight shape when it is moving which mimics the flapping motion of the hawkmoth. FEM model of the wing is implemented to the mechanism as a flexible body and flapping simulations in vacuum conditions are conducted.

Keywords: Flapping wing, micro aerial vehicle, finite element analysis, modal analysis, flapping mechanism, flexible multibody dynamics

ÖZ

ATMACA GÜVESİ KANADININ MODELLENMESİ VE KANAT ÇIRPMA MEKANİZMASINDA UYGULANMASI

Ökmen, Aytek Altuga
Yüksek Lisans, Havacılık ve Uzay Mühendisliği
Tez Yöneticisi: Prof. Dr. Dilek Funda Kurtuluş
Ortak Tez Yöneticisi: Dr. Kutluk Bilge Arıkan

Şubat 2022, 105 Sayfa

Bu çalışmanın temel amacı, kanat çırpan mikro insansız hava aracının kanat çırpma mekanizmasında kullanılmak üzere bir atmaca güvesi (Manduca sexta) kanadını gerçekçi bir biçimde modellemektir. Kanat ilk olarak ANSYS/SpaceClaim programında modellenmiştir. Daha sonra ANSYS/Mechanical programında kanadın sonlu eleman modeli (FEM) üzerinde modal analiz yapılmış ve model doğrulanmıştır. Kanadın sonlu eleman modeli üzerinde ağ iyileştirme çalışması yapılmıştır. Gerçekleştirilen modal analiz sonuçlarının literatürdeki sonuçlarla örtüştüğü gözlemlenmiştir. Esnek çoklu cisim dinamikleri programı ADAMS kullanılarak basit bir düzlemsel dört çubuk mekanizması tasarlanmıştır. Tasarlanan kanat çırpma mekanizması atmaca güvesinin kanat çırparken yaptığı sekiz şeklini taklit edebilmektedir. Tasarlanan kanat modeli esnek cisim olarak mekanizma ile birleştirilmiş ve vakum koşullarında kanat çırpma simulasyonları gerçekleştirilmiştir.

Anahtar Kelimeler: Çırpan kanat, mikro insansız hava aracı, sonlu eleman analizi, modal analiz, kanat çırpma mekanizması, esnek çoklu cisim dinamikleri

To my parents…

ACKNOWLEDGMENTS

I would like to sincerely thank my thesis advisor Prof. Dr. Dilek Funda Kurtuluş, for her guidance and never-ending support during my studies. I feel tremendously lucky to be able to work with her because of her limitless knowledge and experience.

I am extremely grateful for having Asst. Prof. Dr. Kutluk Bilge Arıkan as my co-advisor who offered his support whenever I needed it.

My genuine love from the bottom of my heart goes to my parents, Zinet and Serdar. I would not be able to be where I am without their unconditional love and support. I thank them for always believing in me whatever I do.

I would like to also extend my thanks to my friends, Özgün, Tawfiq and Mürvet, with whom I had the pleasure of working with in the Aerodynamics lab, for their companionship and help.

Additionally, I wholeheartedly thank my friends Salih, Güneş, Batıhan, Artun, Tan, Efe and Hazel for motivating me whenever I felt overwhelmed.

I present my gratitude and thanks to my uncle, who persuaded me to pursue graduate studies in aerospace engineering. Finally, I would like to commemorate my late grandfather, who sparked my interest in aviation.

This work is supported by TUBITAK 116M273 project.

TABLE OF CONTENTS

LIST OF TABLES

TABLES

LIST OF FIGURES

FIGURES

CHAPTER 1

INTRODUCTION

Technological advancements such as the development of micro-electro-mechanical systems (MEMS) and smaller state-of-the-art cameras, sensors, and controllers combined with modern materials such as piezoelectric materials or lightweight polymers, etc. contributed to the development of unmanned aerial vehicles (UAVs) over time. Previously mentioned technological advancements along with new modern requirements paved the way for smaller UAVs called micro aerial vehicles (MAVs) to appear. MAVs are much smaller in size and weigh a lot less than conventional UAVs.

The importance of micro aerial vehicles (MAVs) is growing rapidly day by day in the world especially in the last couple of decades. MAVs can be used for various tasks such as but not limited to intelligence, surveillance, reconnaissance, search and rescue (disaster relief) as well as entertainment (toys, action cameras for extreme sports, etc.). Their quickly increased importance is mainly caused by these vast and diverse areas of applications.

MAV research started around the late 1990s and grew hastily with no chance of stopping or slowing down in near future. There are three different types of MAVs which are fixed-wing, rotary-wing, and flapping wing (ornithopter). This classification is based on means of lift and thrust generation differences among MAVs [1].

Fixed-wing MAVs have a longer range and speed compared to rotary-wing MAVs. However, the maneuverability of the rotary-wing MAVs is higher than the fixed-wing MAVs. Rotary wing MAVs can hover as well while fixed-wing MAVs cannot perform hovering. Flapping wing MAVs (FWMAVs) have a greater range than

rotary-wing MAVs and better maneuverability than fixed-wing MAVs. FWMAVs can perform hovering as well.

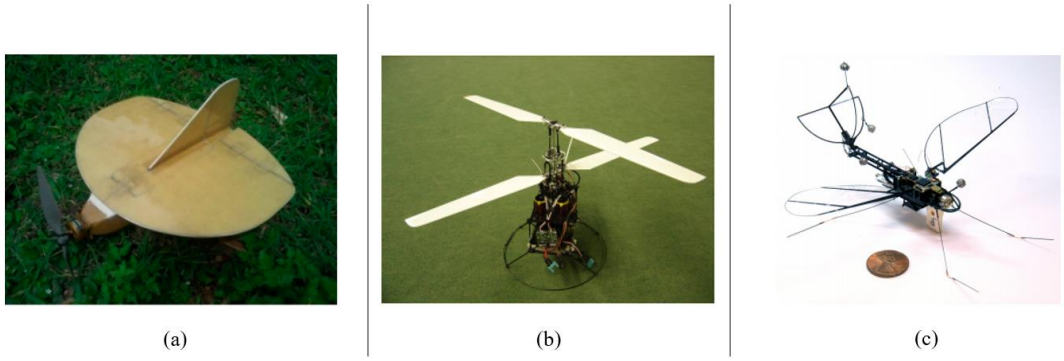

Figure 1.1: (a) Fixed Wing MAV [2] (b) Rotary Wing MAV [3] (c) Flapping Wing MAV [4]

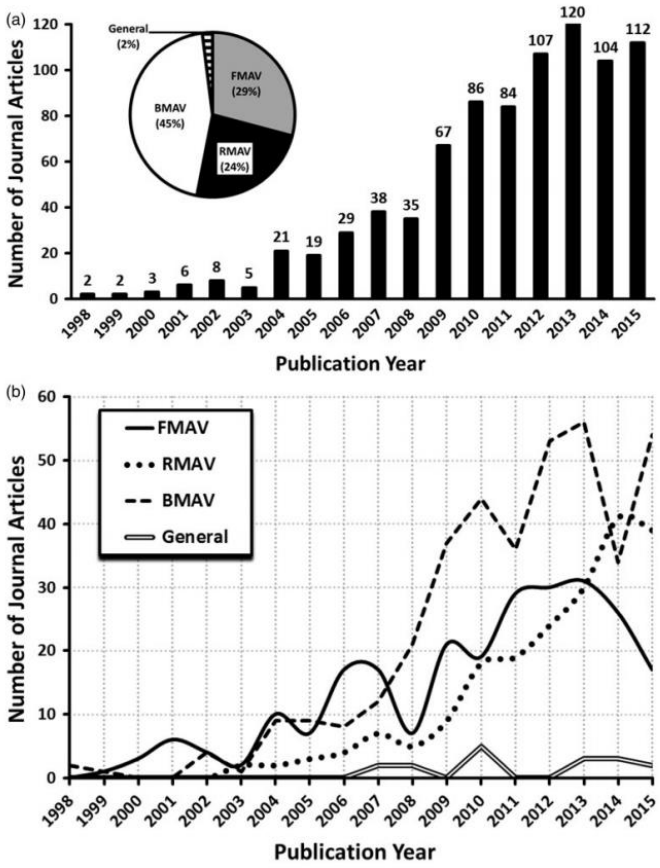

Figure 1.2: (a) Total MAV Journals Published (b) Distribution of Journals by MAV Type [1]

In figure 1.2, MAV types are abbreviated as FMAV (fixed-wing MAV), RMAV (rotary MAV), and BMAV (biomimetic MAV). The increase in the number of journals published about MAVs as time passes is clear in figure 1.2a. From figure 1.2b, it is seen that early MAV research is focused on fixed-wing MAVs, but it has shifted significantly to flapping wing MAVs over the years. Also, an increase in rotary MAV research is seen in figure 1.2b along with a recent decrease in fixed-wing MAV research.

1.1 Flapping Wing Micro Aerial Vehicles (FWMAVs)

FWMAVs' ability to hover and extreme maneuverability at low speeds combined with their low visibility and lightweight make them excellent candidates for indoor use where stealth and obstacle avoidance is crucial [5]. Despite having advantages over both fixed and rotary-wing MAVs, the flapping-wing is the hardest MAV type to model, design, and manufacture. They require an intricate interdisciplinary design and manufacturing process consisting of aerodynamics, propulsion, control, material science, and sensor fusion, etc. Table 1.1 lists the specifications of flapping wing MAVs.

Table 1.1: FWMAV Properties [6]

Specification	**Requirement**	**Details**
Size	<15.24 cm	Max. dimension
Weight	~100 g	Gross take-off weight
Range	1-10 km	Operational range
Endurance	60 min	Loiter time on station
Altitude	<150 m	Operational ceiling
Speed	15 m/s	Max. flight speed
Payload	20 g	Mission dependent
Cost	$1500	Max. cost (2009 USD)

Since designing and manufacturing FWMAVs require knowledge and experience in different areas to stay within the design requirements presented in table 1.1, research about them is also dispersed throughout these said areas. Different research categories about FWMAVs can be listed in five different topics, which are: aerodynamics, guidance, navigation and control, flapping mechanism, structure and materials, and system design. The distribution of the number of published journal articles between 1998 to 2015 in these areas can be seen in the figure below.

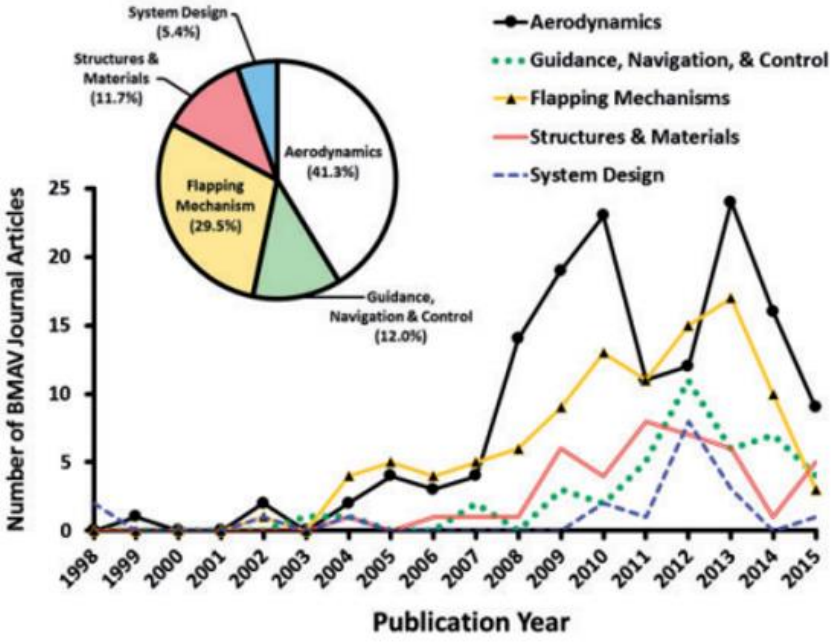

Figure 1.3: Distribution of Different Research Areas for FWMAVs [1]

By looking at figure 1.3, it can be said that the research about FWMAVs is focused mainly on aerodynamics by a considerable margin. That is because unsteady aerodynamics come into play rather than steady aerodynamics when flapping motion is involved. Involvement of unsteady aerodynamics presents more difficult challenges, such as but not limited to lower Reynolds (Re) numbers, time-dependent flows, etc., to overcome for FWMAV to successfully operate as desired.

Overall, the second-highest researched topic is the flapping mechanism. This relatively high interest in flapping mechanism research can be tied to the complex

aerodynamics of flapping as well. To properly mimic the flapping motion and achieve similar aerodynamic forces, this subject is researched extensively.

Guidance, navigation, and control are other critical research areas for FWMAVs. Since they are mainly used in indoor environments, stability and obstacle avoidance is the utmost concern as previously mentioned.

It can also be said that structure and materials are increasingly important subjects. Initially few studies are published but recently it has increased dramatically. The main research point of structures and materials is aeroelasticity. Effects of different advanced and lightweight materials, such as but not limited to piezoelectrics and polymers and their overall contribution to FWMAV performance is studied.

Finally, another interesting point is that in recent years, system design articles are increased. Their main aim is to manufacture FWMAVs rather than focusing on one research area. By looking at the number of published journal articles about the system design area of FWMAVs in recent years, it can be concluded that focus is shifting towards fully functional FWMAVs, which can be used as final products, rather than individual subtopics.

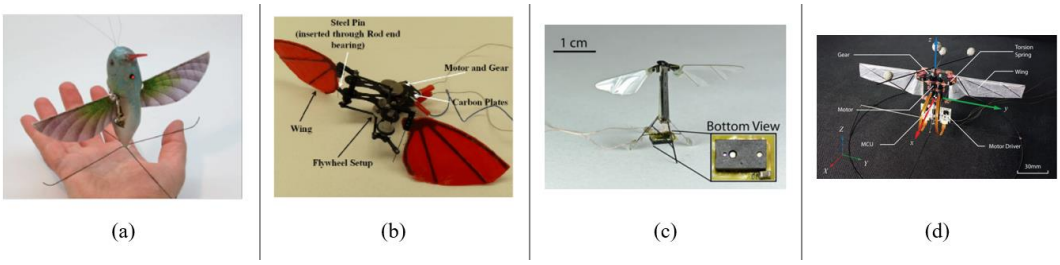

Figure 1.4: Different FWMAV Examples (a) [7] (b) [8] (c) [9] (d) [10]

1.2 Literature Survey

As explained previously, FWMAV design research focuses mainly on aerodynamics and flapping mechanisms. In addition to these two subjects, structures and materials are worth investigating as well. These three crucial subjects must be well understood before making any further attempts at FWMAV design.

In figure 1.5, two different types of aerodynamics, which are conventional and unsteady, are shown. Lift is produced by different means between steady and unsteady aerodynamics [11]. Flapping animals, especially insects, have flying regimes with significantly lower Reynolds numbers compared to planes and helicopters. As a result, the aerodynamic characteristics of flapping are very different from than aerodynamic characteristics of fixed wings [5].

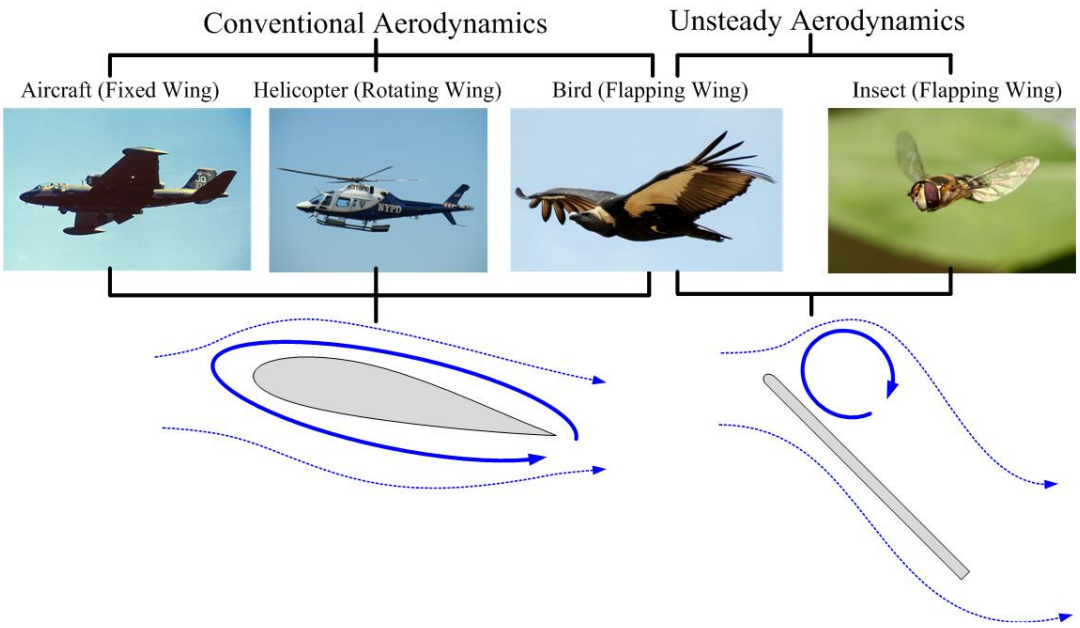

Figure 1.5: Vortex Formations of Fixed Wing and Flapping Wing Aerodynamics [12]

Generally, conventional aerodynamics has a flying regime of high Reynolds numbers and low angles of attack. For conventional aerodynamics, the circulation vortex is around the entire wing. Pressure on the bottom side of the wing is higher than the pressure on the upper side of the wing and lift is created because of this pressure difference between the two sides of the wing.

On the other hand, unsteady aerodynamics usually has a flying regime with significantly lower Reynolds numbers and high angles of attack. Circulation vortex forms at the front of the upper side of the wing and is called leading-edge vortex (LEV) which will be further discussed in the following chapter along with several other phenomena. The Leading-edge vortex creates a very low-pressure area above

the wing thus resulting in a suction force. Lift force is generated through this suction force [12].

1.2.1 Literature Survey of Aerodynamics

Since the generation of lift is completely different in flapping flight, the literature survey on aerodynamics focuses on unsteady and numerical studies in this section. Several studies about unsteady aerodynamics of symmetrical airfoils are examined [13], [14], [15], [16], [17], [18], [19]. Briefly, unsteady aerodynamics of cambered airfoils are examined [20]. Mathematical models of flapping flight aerodynamics and their applications are investigated as well. Weis-Fogh published a paper in which devises a way to estimate aerodynamic forces acting on an insect's wing [21]. Ellington explains flapping insect flight in detail in a broader sense with six different volumes, each focusing on a specific subject, which is the quasi-steady approach [22], morphological parameters [23], kinematics [24], aerodynamic mechanisms [25], vortex theory [26] and lift and power requirements [27].

Dickinson et al. [28] state that the aerodynamic performance of insects is a result of the interaction of three different mechanisms, which are delayed stall, rotational circulation, and wake capture. It is stated that delayed stall is dominant during translational motion of the wings, while the wings sweep the air with a large angle of attack. On the contrary rotational circulation and wake, capture is dominant generate aerodynamic forces during stroke reversals i.e. pronated from a supinated position of the wing or vice versa. A pair of mechanical wings modeled after Drosophila (fruit fly) and placed in mineral oil for force measuring, while flapping, via a load cell as an experimental setup. Measurements for aerodynamic forces are categorized in three different modes which are advanced mode, symmetrical mode, and delayed mode. It is also stated that two rotational mechanisms (rotational circulation and wake capture) are fundamental for adjusting the magnitude and direction of the aerodynamic forces during flight especially when maneuvering.

Challenges and difficulties in using numerical modeling of aerodynamic forces of flapping are presented and discussed by Shyy et al. [29]. Lift and power requirements for eight different insect species, including hawkmoth, are calculated by numerically solving Navier-Stokes equations. It is also stated that large insects with relatively small wingbeat frequencies have lower specific power ranges (18 to 39 $W.kg^{-1}$) than medium and large-sized insects with relatively higher wingbeat frequencies (39 to 61 $W.kg^{-1}$). Hawkmoths are considered to have small wingbeat frequencies in this study. It is pointed out that the main factor that contributes to power is aerodynamic force and specific power is proportional to the product of wingbeat frequency, the stroke amplitude, the wing length, and drag-to-lift ratio for insects with small wingbeat frequencies [30]. Enough lift force, which can carry the weight of an average insect, can be generated by a two-dimensional hovering motion using computational methods by Jane Wang [31]. A pair of counterrotating vortices are formed from leading and trailing edge vortices at the downside of the wing as a result of two-dimensional flapping motion.

FWMAV applications of flapping-wing flight are investigated briefly. An aerodynamic model and a control strategy are presented for FWMAV applications by Doman et al. in [32] and [33] respectively. Equations of motion of an insect with flapping wings are derived then linearized using the rigid body assumption by Sun et al. [34] to provide further insight for the mathematical model of the FWMAV. A proposed mathematical model is tested on four different insects (hoverfly, cranefly, dronefly, and hawkmoth) with differing masses (11-1648 mg) and flapping frequencies (26-157 Hz). For three flies with high wingbeat frequencies, the rigid body assumption is proven to be suitable. However, it is stated that for hawkmoth, which has a lower wingbeat frequency, rigid body assumption has yielded questionable results. Orlowski and Girard derived non-linear dynamics of FWMAVs [35]. Three cycles of flapping are simulated and the insect is modeled as three rigid bodies consisting of two wings and the abdomen. Mass of the wings and their inertial effects on the body are included in the model. Results are compared with a model without the inertial coupling between bodies. It is seen that considering the mass

effects of wings on the body is important for dynamics, stability, and control analyses.

The aerodynamics of a vertically ascending hawkmoth is studied by Nguyen et al. [36]. Wing kinematics, power requirement, and dynamic stability characteristics are taken into account when constructing the model. Wing kinematics for the model is obtained using the minimum required power assumption and artificial intelligence is used for rapid predictions of aerodynamic force and power required. The unsteady vortex lattice method is used for the training of artificial intelligence. As a result, it is found out that hawkmoths use larger flapping frequency and smaller rotation amplitude while ascending flight compared to hover. Another study is conducted by Lua et al. [37]. to understand the relation between wing stiffness and aerodynamic forces in hovering conditions. Force measurement and flow visualization are used for gathering data while a rigid hawkmoth wing model performs flapping and simple harmonic motion. After data is collected for a rigid wing, an experiment is performed again using hawkmoth wings with different stiffness values for two different motions. Hawkmoth flapping is conducted at Re= 7254 and has a reduced frequency of 0.26 while simple harmonic motion is conducted between Re= 7254 and 11700 with a reduced frequency of 0.25. Results show that rigid wings generate aerodynamic forces mainly by the acceleration of the wing and leading-edge vortex (LEV) formation at the upper surface of the wing. It is stated that wake vortices from previous flapping have minor effects. A critical stiffness constant is introduced for flexible wings. Flexible wings with stiffness constants above the critical value can generate almost the same amount of lift as the rigid wings. This makes using flexible wings in FWMAV applications beneficial in terms of lightweight.

Chu et al. investigate the aerodynamics of a wing performing figure of eight flapping motions [38]. Fluid-structure interaction (FSI) and computational fluid dynamics (CFD) simulations are used. Two main variables are identified for obtaining the figure of eight motion, which are initial pitch angle and input link angle, and effects of their variance are investigated. Initial pitch angle values are between 0^o and 330^o with increments of 30^o and input link angles are 30^o, 45^o, and 60^o. Material for the

wing is chosen as balsa wood and has Young's modulus of 3.4 GPa. Results of the study show that the highest lift coefficient value occurs at 90^o initial pitch angle and a higher input link angle generates higher lift. Also, pressure distribution and von Mises stress of the wing are shown. Bhat et al. investigate the effects of different flapping motion profiles as waveforms on insect wing aerodynamics [39]. Rather than using simple harmonic motion for flapping, sweep and pitch motion waveforms are used on a fruit fly wing platform with constant frequency and amplitude. Physical experiments are conducted in a mineral oil tank for measuring forces and torques. It is seen that sweep waveform influences overall lift coefficient whereas pitch waveform influences instantaneous lift coefficient only during stroke reversal. With wider sweep and pitch rates, the possibility of passive pitching of the wing is increased. Kang et al. investigated how flexibility affects the aerodynamics of flapping wings [40]. Effects of chordwise, spanwise, and isotropic flexibility are investigated. Different forces are defined as functions of Reynolds number (Re), reduced frequency (k), and Strouhal number (St). A relationship between propulsive force and maximum wingtip deformation parameter (γ) is found. This wingtip deformation parameter is defined as a function of density ratio, Strouhal number, reduced frequency, the natural frequency of the wing, flapping frequency, and flapping amplitude. It is stated that maximum lift force is obtained when the wing's flapping frequency is close to its natural frequency but optimal lift force is obtained when the wing is flapping with approximately half of its natural frequency.

Ellington and Willmott used high-speed videography for recording hawkmoths whilst they hover or during forwarding flight with speeds up to 5 m/s [41]. After successfully understanding the kinematics of hovering and forward flight of the hawkmoths their aerodynamic consequences are investigated by calculating mean lift coefficients [42]. Kurtuluş et al. [43] used a simplified geometry instead of complex geometries of insect and birdwings to understand unsteady aerodynamics and vortex formation mechanisms during flapping motion. A laminar flow with a Reynolds number of 1000 is assumed for investigating vortex topology. Numerical simulations, laser sheet visualizations, and particle image velocimetry are performed.

1.2.2 Literature Survey of Wing Morphology

Effects of wing shape, material, and flexibility on aerodynamics are investigated briefly in this section since it greatly alters the aerodynamic performance outcome of flapping motion. Hu et al. investigated the benefits of using flexible membrane airfoils at low Reynolds numbers for FWMAV applications as compared to using conventional rigid airfoils [44]. Aerodynamic force measurements revealed that flexible membranes have better aerodynamic performance compared to rigid membranes at low Reynolds numbers. The reasons for the better aerodynamic performance of flexible membranes are stated as the ability to change camber, better adapting to different flow conditions for balancing the pressure difference between upper and lower surfaces thus preventing flow separation on the upper surface and trailing edge deflection which results in reducing the effective angle of attack thus delaying stall. Wing flexibility and wing oscillations are considered as lift enhancing mechanisms at low Reynolds numbers by Cleaver et al. [45]. Experimental results yielded a significant difference between lift coefficients (C_L) of a flexible wing and a rigid wing which are 2.77 and 1.38 respectively with both wings having the same aspect ratio (AR) of 3. Flexibility effects are further investigated by Agrawal and Agrawal by experimentally measuring the static-load deformation characteristics of a hawkmoth wing [46]. A bio-inspired wing is designed using finite element analysis (FEM) and an optimized solver helped the static load of the designed wing to match with the static load of the biological wing. A flexible wing is then manufactured using different materials like carbon, nylon, and rubber for obtaining different vein stiffnesses whereas latex is used for the wing membrane. Results show that an increase in thrust in flexible wings compared to rigid wings.

A finite element solver is used by Ramamurti and Sandberg to compute unsteady flow past flapping Drosophila wings, results of this study verify the hypothesis of Dickinson [47]. Bai et al. proposed a new bionic flapping motion, also based on Drosophila, for designing and manufacturing FWMAVs [48]. The numerical method is presented and a CFD solver is employed for solving the proposed numerical method. Obtained results from the proposed method are compared with

Dickinson's results in three modes i.e., advanced mode, symmetrical mode, and delayed mode, and seen that they are in good agreement.

Yoon et al. [49] studied the effects of camber on unsteady aerodynamic characteristics of FWMAV wings. A three-dimensional (3D) fluid-structure interaction (FSI) solver is developed to accurately model deforming wing and its geometry. By analyzing the aeroelastic effects, the significant impact of passive twisting motion on the aerodynamic performance of cambered wings is shown. Three flapping frequencies are chosen as 20, 24, and 28 Hertz (Hz). A flapping frequency of 24 Hz is chosen as the normal operating condition. Wings have a minimum camber angle of 5^o and a maximum camber angle of 25^o with increments of 2.5^o. Results show that maximum thrust occurs at a camber angle of 12.5^o and it is 9% more efficient compared to a flat wing thus proving that camber increases the aerodynamic performance of an FWMAV wing. Reid et al. [50] have approached wing morphology in a more general sense. It is discussed that wing deformation, which influences the flight of the insect, is directly related to vibration spectra and mode shapes of the wing. The main aim of this study is to create an artificial insect wing that is isospectral and isomodal to a biological insect wing. Experimental modal analyses are conducted on hawkmoths. Then, artificial hawkmoth wings are created by using additive manufacturing and heat molding. Results of the study show that there is an acceptable difference of 7% and 16% for the first two natural frequencies respectively between artificial and biological wings thus paving the road for designing and manufacturing more advanced artificial wings. Shahzad et al. [51] further investigated the wing morphology of the hawkmoths focusing on flexibility's effect on its wing's overall aerodynamic efficiency at Re=400 numerically. Forewing shapes are defined by three different values for the radius of the first moment of wing area, which are $\bar{r}_1$=0.43, 0.53, and 0.63, and four different aspect ratios (AR), which are AR=1.5, 2.96, 4.5 and 6. The stiffness of the hawkmoth wing is individually distributed into 12 different constructed forewings. Then immersed boundary method is used for solving 3D, viscous and incompressible Navier-Stokes equations coupled with a non-linear finite element solver for FSI simulations. Numerical results show that chordwise and spanwise deformations and wingtip deformation are

directly proportional with aspect ratio. Also for the first three aspect ratio values of 1.5, 2.96, and 4.5, it is observed that lift is increased by up to 39%, 18%, and 17.6% respectively with flexibility effects for all three $\bar{r}_1$ values. It is concluded that out of 12 different wing shapes defined, all can be used for FWMAVs except 2 which are $\bar{r}_1$=0.53, and 0.63 with an aspect ratio of AR=6 since they produce negative lift because of rapid pitch down rotation and lower stroke angular velocity.

Sims et al. [52] conducted a morphological study on hawkmoth wings. The geometry of a wing is captured using computed tomography (CT) and frequency data is collected by using laser vibrometry both in air and in a vacuum. The finite element (FE) model is constructed to find the natural frequencies of the wing. Results of experimental and numerical results are compared for obtaining an accurate model of the hawkmoth wing. The effects of wing venation and wing camber on the wing's natural frequencies are presented and discussed. O'Hara and Palazotto also studied structural properties such as average mass, area, shape, size, and camber of hawkmoth wings [53]. Further emphasis is placed on the venation and membrane of the wing. Their material properties i.e., elastic modulus are measured. Data gathered from the morphological study is aimed at forming a basis for future biomimetic wing applications. A fluid-structure interaction (FSI) based analysis, for both rigid and flexible wings, is performed by Nakata and Liu for measuring the aerodynamic performance of a hovering hawkmoth [54]. Measurements are evaluated in terms of aerodynamic force, power and efficiency. It is revealed that by bending of the flexible wing, leading-edge vortex (LEV) breakdown is delayed and wing bending and twist enhance the aerodynamic force just before stroke reversal. It is also stated that hovering efficiency is increased in flexible wing due to wing twist. Wing stiffness effects on aerodynamic performance are further studied by altering different parameters such as Young's modulus and thickness to see changes in aerodynamic performance. It can be deduced that aerodynamic efficiency is higher in flexible wings than rigid wings as a result of wing deformation while flapping.

1.2.3 Literature Survey of Flapping Mechanisms

The four-bar mechanisms are mostly preferred for flapping-wing mechanisms since they are rather simple. For this reason, literature survey on flapping mechanisms mainly focuses on four-bar mechanisms. Three main subjects focused on while designing and optimizing the mechanism are aerodynamics, oscillator dynamics, and actuators. A design framework is proposed by Analooee and Ghayour [55]. It consists of three different flowcharts for determining the dimensions of the mechanism's links and one flowchart for mechanical design adding up to a total of four algorithms. A force determination analysis, which is a part of a mechanical design algorithm, is conducted by a MATLAB code based on the superposition principles of D'Alembert. A flapping wing mechanism is designed and manufactured by using the proposed framework as a result. A resonance-based four-bar mechanism is developed by Khan and Agrawal [56]. Maximum aerodynamic efficiency is intended and the mechanism is driven by conventional motor and gearbox Torsion springs are used for mimicking the pitching motion of wings passively. Burgess et al. compared fixed wings, bird flapping, and insect flapping in terms of mechanism movement, joint types, actuators, and control algorithms [57]. They designed a mechanism with ball bearings to achieve pitching. Relation between wingbeat frequency and power is observed and it is seen that they are directly proportional. To further gain an insight, another control method is observed [58].

An insect scale flapping wing mechanism (FWM) inspired by hawkmoths is introduced by Moses et al. [59]. The designed mechanism has dimensions of 21x24x11 millimeters (mm) and weighs 1.2 grams (g) which are both well within the limits of requirements for FWMAVs explained in Table 1. The mechanism requires 402 milliwatts (mW) to generate enough lift and results show that it can produce 1.3 gram-force of lift at a flapping frequency of 21.6 Hz which means it is capable of lifting itself.

To mimic insect flapping more accurately, the figure of eight motion of the wingtip is deemed crucial. Lemniscate (figure of eight) mechanism is found in a reference

that lists different types of mechanisms [60]. Lemniscate mechanism is a planar four-bar mechanism. It can perform pitching and plunging motions of the wing while performing a figure of eight shape. After encountering the lemniscate mechanism, the literature survey of flapping-wing mechanisms is mainly focused on four bar-type mechanisms. Because they are simple to design, manufacture, and test, it is seen that they are vastly used in flapping-wing mechanisms. A spherical four-bar flapping mechanism, which can achieve the desired figure of eight shape, is designed by Rehmat et al. [61]. The spherical shape of the mechanism is inspired by the human shoulder joint which is called a ball and socket type joint. Several different mechanism layouts, with differing link lengths and angles, are evaluated and the optimal one is chosen as a result. Spherical four-bar mechanisms are much more complicated than planar four-bar mechanisms. If the axes of four linkages of the mechanisms don't coincide, its mobility is limited. To overcome this problem linkages of the mechanism are placed in two concentric spheres. A wing manufactured from balsa wood and aluminum linkages are used in the flapping mechanism. Data acquisition at a 10 kHz sampling rate is preferred and low-pass Butterworth is used for filtering the signals above 50 Hz. Finally, high-speed cameras are used for imaging and experimental and numerical values are compared. Eventually, it is seen that both results are in good agreement with each other.

A simple planar four-bar mechanism that can draw the figure of eight shape is designed by Zbikowski et al. [62]. Four bar mechanism used in the study is a double-rocker Watt mechanism. The mechanism is designed to operate at 20 Hz and actuated by a simple DC motor. Two separate four-bar linkages and a gearbox is used to actuate two wings by Nguyen et al. [63]. Additional to the two flapping wings, a pair of fixed wings are placed aft of the flapping ones. The designed mechanism is bulky which intends to mimic the thorax (abdomen) of the insects. To shed weight, gears are manufactured from carbon fiber. Mechanism motion is similar to Weis-Fogh's "clap and fling" mechanism [21].

The flapping motion of the insect wing while hovering is observed by Phan et al. [64]. Along with the four-bar linkage, a pulley system is also included in the flapping

mechanism. By the addition of the pulley system, stroke amplitude is increased and flapping of the rhinoceros beetle is mimicked successfully. Wings are capable of pitching while flapping and using a flexible material as the wing membrane enabled the wings to mimic torsion as well. A double Scotch yoke mechanism is designed to achieve the desired figure of eight shape in a spherical plane, rather than in a flat plane, by employing the Lissajous curve [65]. Using a double Scotch yoke mechanism achieves a smoother flapping motion which results in reduced stress on the mechanism parts thus aerodynamic loads are highlighted as a result.

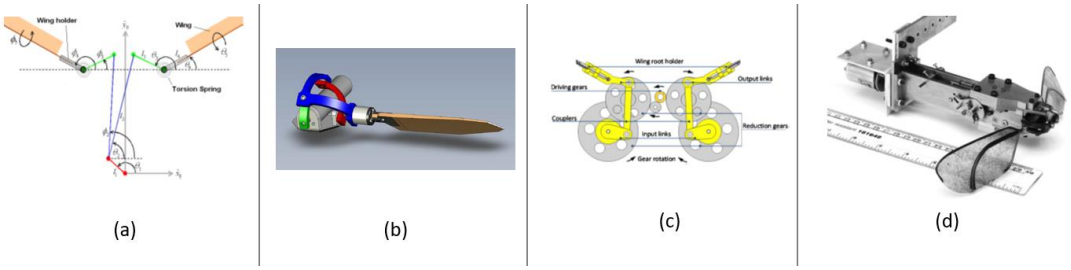

Figure 1.6: (a) Mechanism of Khan, Agrawal [56] (b) Mechanism of Rehmat et al. [61] (c) Mechanism of Nguyen et al. [63] (d) Mechanism of Zbikowski, Galinsky [65]

1.3 Purpose and Scope of Thesis

The main purpose of this thesis is to design a simple yet effective flapping wing mechanism for FWMAV applications and obtain numerical results from flapping simulations using an accurate insect wing model to act as a basis for further experimental and numerical work. Most flapping mechanisms encountered in literature are either not capable of mimicking the insect flapping accurately or overly complicated. In addition, the wings used in both numerical and experimental tests do not reflect the true nature of biological wings.

Mechanisms, which are not capable of correctly imitating the insect flapping, generally only perform plunging motion of the wing. Pitching and stroke reversal are generally ignored and the absence of these motions from flapping greatly constraints the aerodynamic performance of FWMAVs. Consequently, designing a mechanism

that is able to perform pitching and stroke reversal motions along with the plunging yields better overall aerodynamic performance.

On the other hand, sophisticated mechanisms, which are able to perform more than plunging, are excessively complex. By nature of FWMAVs, flapping mechanisms must be small in size, by addition of complexity factor to size limitations, it becomes very difficult to even manufacture such mechanisms. In this study, a mechanism that combines accurate flapping motion with a relatively simpler design than its counterparts is designed and simulated.

A wing model that closely resembles a real-life insect wing is used in numerical simulations for obtaining optimum results. Accompanying wing models with different features are simulated using the same mechanism for comparing results.

The current study is divided into six chapters and presented accordingly.

In chapter 1, general information about MAVs and FWMAVs is briefly explained, a literature survey about key points of the current study is presented and the purpose of the thesis is stated.

Chapter 2 explains flapping-wing flight in general. Wing morphology and kinematics are investigated. Stroke reversal motion is introduced as well. In wing morphology, the geometry of the wings and material and structural properties of wings are presented. Wing kinematics explained coordinate frames and plunging, pitching, and heaving motions, which occur during flapping. Finally, several phenomena which do not apply to conventional aerodynamics are explained.

Chapter 3 focuses on planar four-bar mechanisms. Their position, velocity, and acceleration analyses are presented. Flapping wing mechanism design is introduced and it is explained that it is able to perform a figure of eight motion, as a result of combining plunging, pitching and stroke reversal, which resembles natural insect flapping. Also, position, velocity, and acceleration analyses are performed on each link using flexible multibody dynamics software ADAMS in order to validate the mechanism’s movement.

In chapter 4, the construction of the wing model is explained in detail. The reason for choosing the hawkmoth as an inspiring specimen for the wing model is explained. Hawkmoth wing's geometrical and structural properties are given along with its wing kinematics. Next, a finite element model is created in ANSYS with previously introduced properties. Modal analysis is conducted on the finite element model of the wing and results are compared with literature results for model verification. Additionally, several different finite element models are constructed with different structural properties such as different materials and varying vein diameters. Modal analyses are performed again on these models and results are compared with the initial model's modal analysis results.

In chapter 5, constructed wing model is imported from ANSYS/Mechanical, the program used for modal analyses, to flexible multibody dynamics software ADAMS as a flexible part. The designed planar four-bar mechanism is coupled with the imported flexible wing in ADAMS and flapping simulations are conducted. Wing root and wingtip deflections are presented for different flapping cases. Other wing models with different attributes are imported as well and results are compared.

Chapter 6 includes the results and discussion about the overall study. Final remarks are presented in this chapter for the conclusion.

CHAPTER 2

FLAPPING WING FLIGHT

To develop FWMAVs, it is important to understand the flight mechanics of insects and birds which fly in a lower Reynolds number regime than usual. Animals with different flapping wings produce different aerodynamic forces depending on their structure. They need to endure fluid dynamics forces as well as inertial and elastic forces caused by sudden acceleration and deceleration of their mass [66]. Wing morphology and kinematics must be well understood to correctly translate the generated forces from biological wings to artificial wings of FWMAVs.

Properties like wingspan, chord length, aspect ratio, and wing camber are considered geometrical properties whereas flexibility of membrane, the rigidity of wing veins, density, etc. are considered structural properties. Geometrical and structural properties constitute the morphology of wings. In figure 2.1, different species of insects and birds can be seen with various geometrical and morphological wing features.

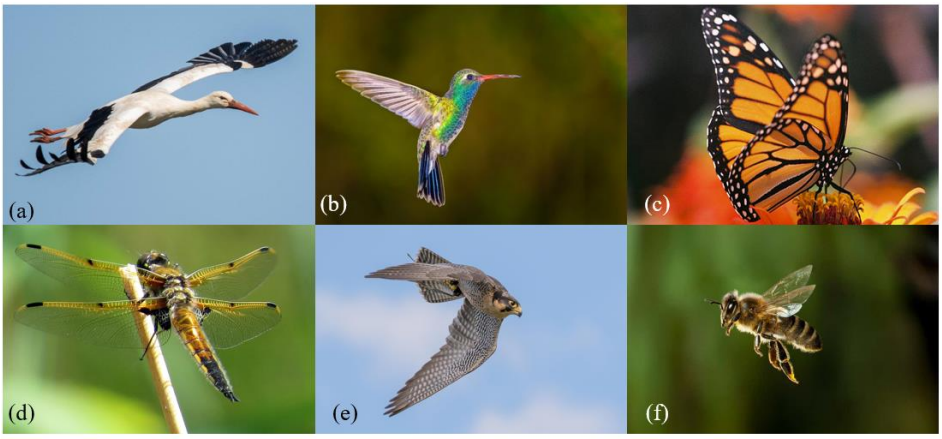

Figure 2.1: Examples of Flapping Wing Animals (a) Stork [67] (b) Hummingbird [68] (c) Monarch Butterfly [69] (d) Dragonfly [70] (e) Peregrine Falcon [71] (f) Honeybee [72]

2.1 Wing Morphology

The aerodynamic forces generated by insects via flapping depend heavily on the wing's morphology. The morphology of the wings can be separated into geometrical and structural properties. Geometrical properties include shape, length, area, etc. On the other hand, structural properties include but are not limited to the density, venation, and elasticity of the wing material.

2.1.1 Geometrical Properties

In this section, geometrical aspects of the insect wings are investigated in more detail. In figure 2.2, some geometrical parameters are given. The wing base is the location where the wing attaches to the body of the insect and it is also called a wing root. The farthest distance from the wing root is called the wingtip. The length from one tip of the wing to the other wing's tip is called span (b). The forward edge of the wing is called the leading edge and the aft edge is called the trailing edge. The straight distance between the leading edge and the trailing edge is called chord (c). The total area of two wings is denoted by (A) whereas the area of one wing is denoted by (S). One wing length (R) makes up half of the span.

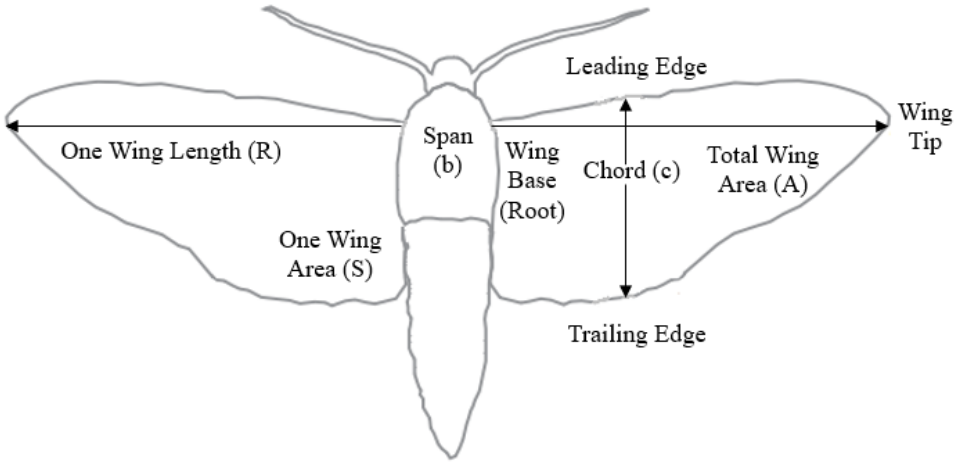

Figure 2.2: Geometrical Properties of Insect Wing [11]

It is clear from figure 2.2 that the chord length of the wing is not constant along the spanwise direction. The mean aerodynamic chord (M.A.C., denoted by $\overline{c}$) is calculated to express changing chord lengths with a single variable. The aspect ratio (AR) of a wing is the ratio of span to its mean chord. It is a dimensionless variable and it can be calculated by dividing the square of span (b^2) with total wing area (2S) shown in equation 1 below.

$$S = \int_0^R c dr = \bar{c}R \tag{1}$$

$$AR = \frac{b}{\bar{c}} = \frac{b^2}{2S} \tag{2}$$

In Table 2.1, which can be seen below, wing morphology data of various insect species capable of flight are given by Mao and Gang [64]. Mass of the insect (m), the mass of wing pair (m_w), wing length (R), mean aerodynamic chord ($\bar{c}$), and area of one wing (S) are given. Mass is given in milligrams (mg) whereas the ratio of the mass of wings to the mass of insect is given in percentage. On the other hand, lengths of one wing and mean aerodynamic chord is given in millimeters (mm) and the area of one wing is given in millimeter square (mm^2).

Table 2.1: Morphological Data of Various Insect Species [73]

Species	**m (mg)**	**m_w / m (%)**	**R (mm)**	**$\bar{c}$ (mm)**	**S (mm^2)**
Fruit Fly	0.72	0.24	2.02	0.67	1.36
Cranefly	11.4	4.29	12.7	2.38	30.18
Hoverfly	27.3	1.27	9.3	2.2	20.48
Dronefly	68.4	1.5	11.4	3.19	36.89
Ladybug	34.4	2.87	11.2	3.23	36.12
Honeybee	101.9	0.5	9.8	3.08	30.14
Bumblebee	175	0.52	13.2	4.02	54.9
Hawkmoth	1648	5.79	51.9	18.26	947.8

Insects given in table 2.1 can be categorized in four different orders which are Diptera, Coleoptera, Hymenoptera, and Lepidoptera. The fruit fly, cranefly, hoverfly, and dronefly are placed in Diptera order (two-winged flies and mosquitoes) and the ladybug is placed in Coleoptera order (beetles). Honeybee and bumblebee fall into Hymenoptera order (bees) and hawkmoth is placed in Lepidoptera order (moths).

Birds' wing aspect ratios are higher than insects' wing aspect ratios. However, insects fly in lower Reynolds numbers. Since it is very difficult to achieve enough lift in these conditions, insects flap with a higher frequency and use different flapping trajectories. It can be said that different flapping behaviors of birds and insects depend on species, body shape, and size which results in using aerodynamic forces (lift and drag) differently from each other [74].

Birds generate more lift with one stroke of the wing than insects. They tend to flap less and glide more whereas insects flap their wings more rapidly than birds. MAV design limitations given in table 1.1 might not be achievable when FWMAVs are based on bird flapping because of the difference between the means of aerodynamic force generation of birds and insects. Inevitably, flapping-wing MAVs must draw inspiration from insects.

In figure 2.3, a simple representation of insect flapping can be found. The line with arrows represents the trajectory of the wing for one flapping cycle. Half of the flapping cycle is called upstroke (when the wing is moving in an upwards direction) and the other half of the flapping cycle is called downstroke (when the wing is moving in a downwards direction). During the upstroke wing is supinated and during the downstroke wing is pronated. When the wing is pronated, it means that the bottom surface of the wing is facing downwards and when the wing is supinated, the bottom surface of the wing is facing upwards.

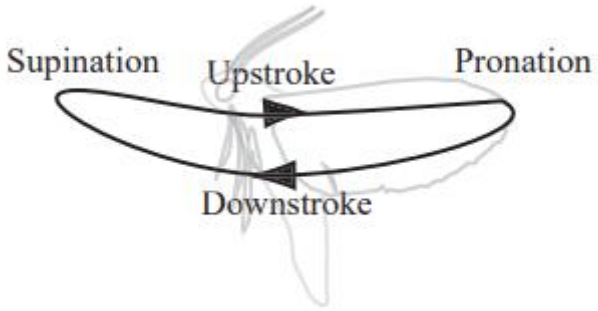

Figure 2.3: Insect Flapping [11]

One flapping cycle consists of three different wing movements. The first movement is called plunging (also known as heaving or feathering), where the wing moves up and down quickly with no rotation similar to flutter. The second motion is pitching, where the angle of attack of the wing changes with rotation and the wing becomes either supinated (during upstroke) or pronated (during downstroke). Wing's position change from supinated to pronated or vice versa is called stroke reversal. The third and final movement is called surging, where the wing leaps forwards along the stroke plane during flapping.

Upstroke consists of one translational (down to up) and one rotational (transition from pronation to supination) movement of the wing and downstroke vice versa, completing one flapping cycle. It is seen that insects can change their flapping characteristics, such as stroke plane and angle of attack, to hover or fly forwards [75].

2.1.2 Material and Structural Properties

Only invertebrates with wings are insects. Coincidentally their wings are significantly different than vertebrates with wings (birds). As a result, FWMAV applications based on insect wings require consideration of several crucial traits of the wings such as venation, flexibility, wing shape, size, and weight.

Two membranes and veins between membrane layers can be seen when an insect wing's cross-section is observed such as in figure 2.4 below. Vein profiles are generally elliptical. Veins do not only structurally support the thinner and more flexible membrane layers, but they also transport hemolymph (insect body fluid acting as blood) and provide housing for nerves.

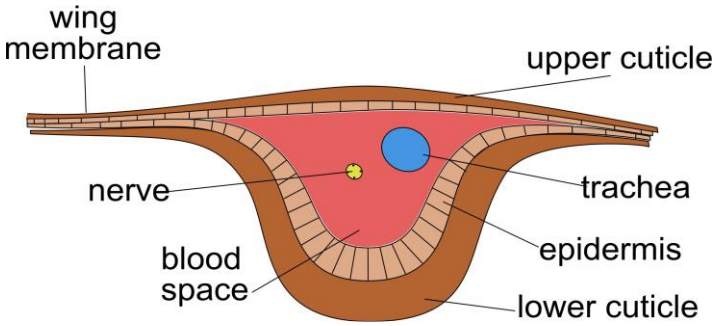

Figure 2.4: Cross Section of Insect Wing Vein [76]

Veins are spread through the wing in both spanwise and chordwise directions. As a result, wings look like they are separated into different regions by branched veins. This grouping, which can be seen in figure 2.5, on the wing makes identifying and naming membrane regions and veins very practical.

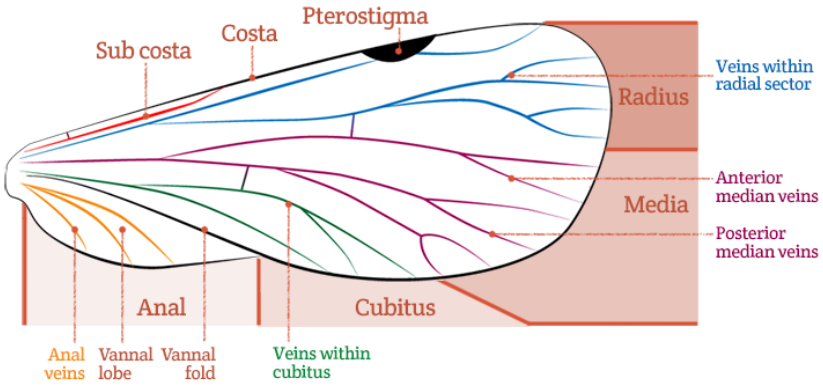

Figure 2.5: Venation Map [77]

The main regions of the wing are radius, media, cubitus, and anal regions whereas major veins are costa, sub-costa, radial, and medial veins. Veins that are located in cubitus and anal regions tend to have smaller root and tip diameters compared to veins in other listed regions. The leading edge of the insect wing is supported by a

costal vein, which is usually bigger in diameter than other veins. The trailing edge of the wing is called the anal region and usually, it is not supported by a vein.

Insects with complex vein structures can fold their wings backward. It is an important criterion for classifying insects along with several other criteria such as material and number of wings and whether wings are covered or exposed when wings are folded. The number of wings can be either two or four depending on insect species. Insects with two pairs of wings usually have better aerodynamic performance since their fore and aft wings are coupled. However, some species such as dragonflies can flap their four wings individually.

Insect wings are greatly deformed (especially wingtips) when flapping to generate required aerodynamic forces for hovering or flying forwards. These deformations depend heavily on the structural stiffness of the wings which is a function of wing material and geometry. Young's modulus or elastic modulus (E) and second area moment of inertia (I) define structural stiffness (EI). Young's modulus is the wing material's resistance whereas the second area moment of inertia is wing geometry's resistance to deformation. Young's modulus is calculated using the below equation:

$$E = \frac{\sigma}{\varepsilon} \tag{3}$$

σ denotes tensile stress and ε denotes extensional (shear) strain. Young's modulus is directly proportional to the material's rigidity. The second area moment of inertia is calculated with the below equation:

$$I = \frac{t^3 \bar{c}}{12} \tag{4}$$

In the above equation, t denotes thickness and $\bar{c}$ denotes the mean aerodynamic chord of the wing. From above equations 3 and 4, the total deformation of the wing can be found as:

$$\delta = \frac{FL^3}{3EI} \tag{5}$$

The above equation is used to find the end load on the cantilever beam with single fixed support. In this case, the wing's attachment point to the insect's body (wing

root) is deemed as support, and the wing is considered as a cantilever beam. F denotes force, L denotes length in equation 5.

Another important relation when considering material deformation is Poisson's ratio (ν) which can take any value between 0 and 0.5. High Poisson's ratio indicates that the material can greatly deform even when subjected to small forces. It is calculated with the below equation:

$$\nu = \frac{d\varepsilon_{trans}}{d\varepsilon_{axial}} \tag{6}$$

In equation 6, ε_{trans} is transverse strain, which is positive for transverse compression and negative for transverse tension, and ε_{axial} is axial strain, which is positive for axial tension and negative for axial compression.

2.2 Wing Kinematics

To accurately describe and understand the flapping motion of the wing, coordinate axes are used to define reference frames (or coordinate systems). It is important to clearly define different reference frames because forces and moments acting on one reference frame might be different according to another reference frame for the same body.

Four different coordinate systems, which are named earth-fixed, body-fixed, stroke plane frame, and wing frame, are defined for flapping motion. All four reference frames are orthonormal and right-handed. The earth-fixed coordinate system is denoted by axis names X_E, Y_E, Z_E and can be seen in figure 2.6a. It can be fixed to any arbitrary point on Earth where X_E-axis points north, Y_E-axis points inwards through the page, and the Z_E-axis points towards the center of the Earth at all times independent from the motion of the body.

The body-fixed coordinate system is fixed to the center of gravity of the insect, which is denoted by point O in figure 2.6b and changes orientation according to it, unlike the earth-fixed reference frame. To depict the body-fixed coordinate system more clearly in figure 2.6b, the insect is slightly tilted counter-clockwise with an angle of

χ, and orange color is used for depicting coordinate axes. X_B-axis runs parallel with the insect's body whereas Y_B-axis points towards the inside of the page, similar to its earth-fixed counterpart. Finally, Z_B-axis is perpendicular to X_B-axis at all times. Rotations around X_B, Y_B, and Z_B axes are named roll, pitch, and yaw and denoted by Euler angles ϕ, θ, and ψ respectively.

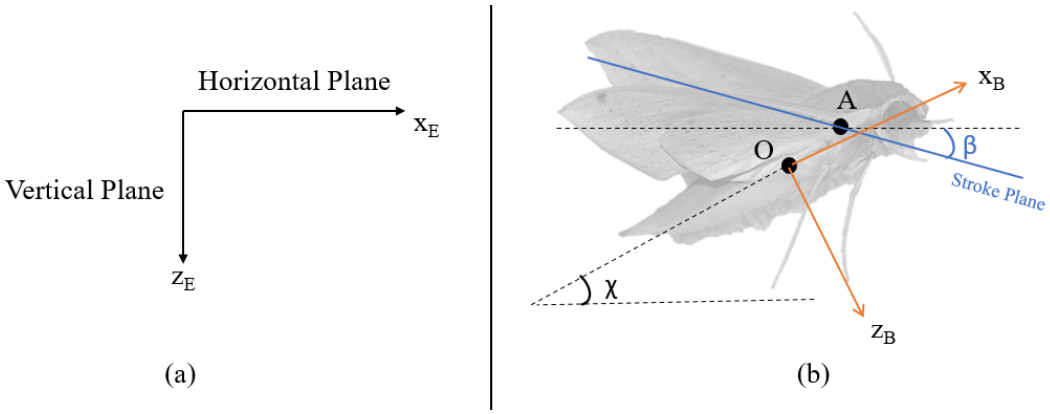

Figure 2.6: Earth-fixed (a) and Body-fixed (b) Coordinate Systems

The stroke plane is depicted in figure 2.6b with blue color. The angle β is used to distinguish the stroke plane frame from the earth-fixed frame since the wing completes a different type of motion compared to the body.

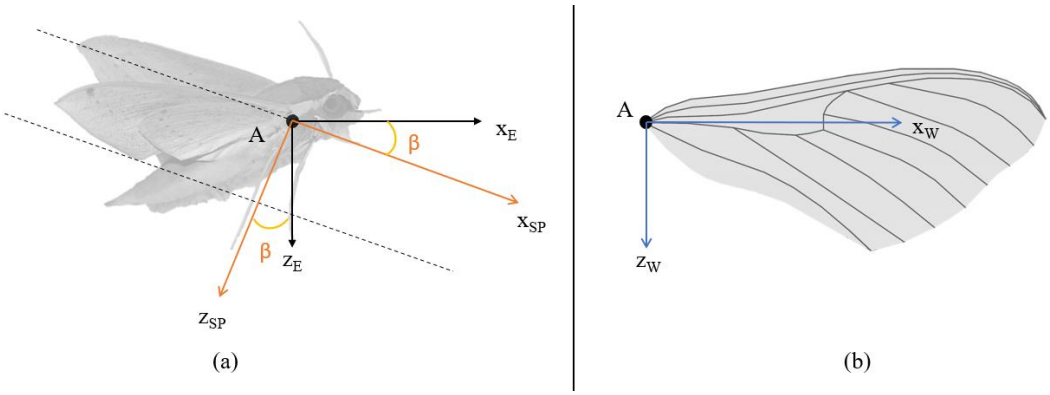

Figure 2.7: Stroke Plane Frame (a) and Wing Frame (b)

In figure 2.7a, the stroke plane frame is shown on the insect along with the earth-fixed frame for clearer demonstration. The stroke plane frame is aligned with the flapping trajectory of the wing. X_{SP}-axis points towards the downstroke direction of

the wing, Y_{SP}-axis is pointing inside of the page and Z_{SP}-axis is perpendicular to X_{SP}-axis similar to other Y and Z axes of reference frames.

The wing frame is shown in figure 2.7b, in which the wing shape shown is taken from the wing model constructed for this study, and it is fixed to point A, which is the root of the wing. X_W-axis lies along the span of the wing whereas Z_W-axis runs through the chord of the wing. Finally, Y_W-axis is pointing inwards from the page as well.

Three different motions, which are pitching, plunging, and surging, are previously introduced in Section 2.1.1. As an insect's wing undergoes flapping, these three motions occur simultaneously as a result of the wing's rotation around stroke plane frame axes. Pitching motion occurs around Y_{SP}-axis, plunging motion occurs around X_{SP}-axis and surging motion occurs around Z_{SP}-axis. Feathering angle (α), elevation angle (θ), and stroke positional angle (ϕ), which should not be confused with Euler angles, are used to denote pitching, plunging, and surging motions respectively and shown in figure 2.8.

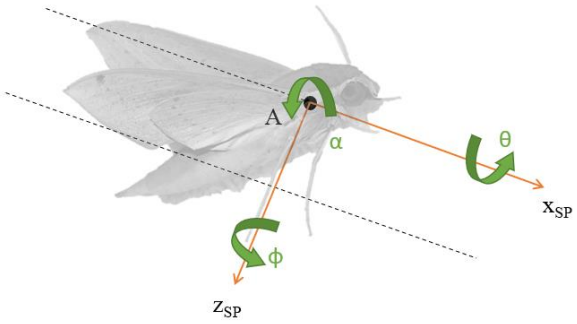

Figure 2.8: Stroke Plane Frame Angles

Figure 2.9, which uses various views from constructed wing model but without veins for simplification purposes, can be referred to further clarify stroke plane frame angles. Figure 2.9a features the wing's side view indicating a feathering angle (α), which is for the pitching motion, is the angle between the wing's bottom surface and positive x-direction of the stroke plane frame. Also, the leading-edge and trailing edge of the wing is clearly represented. In figure 2.9b, view from the top of the wing

is shown for surging motion and stroke positional angle (ϕ) is the angle between the leading edge of the wing and Y_{SP}-axis. Finally, in figure 2.9c front view of the wing is shown with wing root and wingtip labeled, where elevation angle (θ) is the angle between the bottom surface of the wing and y-direction of the stoke plane frame in the negative direction. Elevation angle is associated with the plunging motion of the wing.

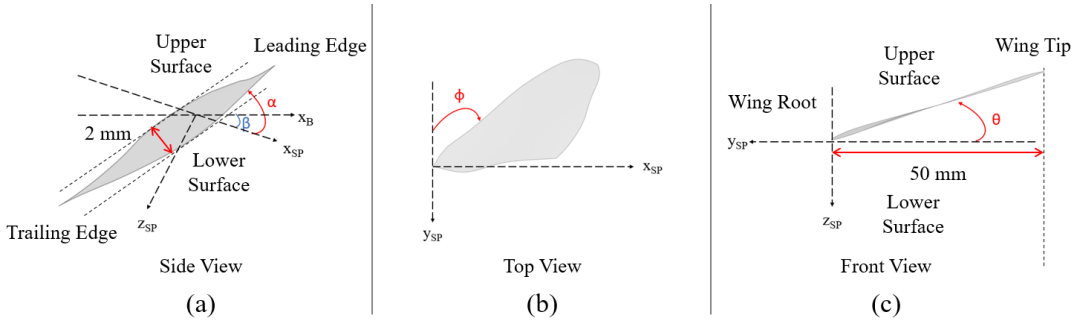

Figure 2.9: Side (a), Top (b), and Front (c) Views of the Stroke Plane Frame

The previously mentioned movements plunging and pitching motions are shown in figures 2.10a and 2.10b respectively. The side view of the wing model is used again to show the said motions and the earth-fixed coordinate system is located at the top left of the figure for reference. All three motions, including surging, are periodic (sinusoidal).

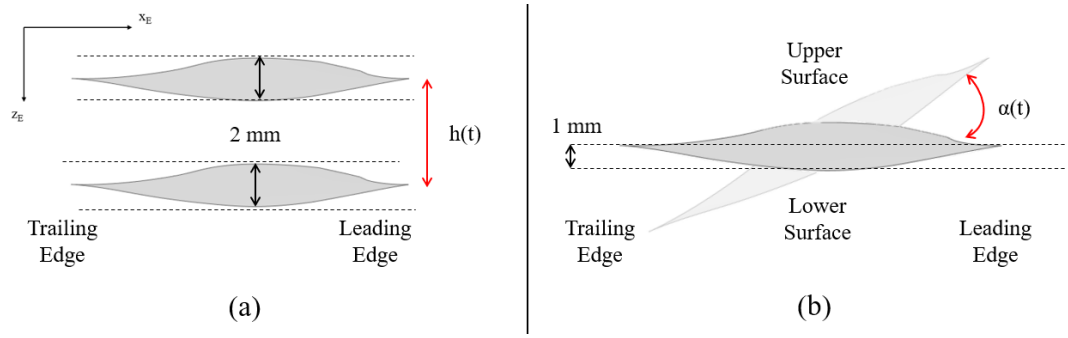

Figure 2.10: Plunging (a) and Pitching (b) of the Wing

The displacement equations non-dimensionalized by the mean aerodynamic chord are given below. For plunging:

$$x(t) = 0 \tag{7}$$

$$y(t) = hcos(k_{plunge}t + \phi_{plunge}) \quad (8)$$

For pitching:

$$x(t) = rcos(\theta + \alpha(t)) \quad (9)$$

$$y(t) = rsin(\theta + \alpha(t)) \quad (10)$$

$$\alpha(t) = \alpha_0 cos(k_{pitch}t + \phi_{pitch}) \quad (11)$$

Finally for surging:

$$x(t) = x_0 cos(k_{surge}t + \phi_{surge}) \quad (12)$$

$$y(t) = 0 \quad (13)$$

In above equations 7-13, h is the plunging amplitude, which is also given as h(t) in figure 2.10a, k values are reduced frequency for each motion, α_0 is the pitching amplitude, which is given as α(t) in figure 2.10b, r and θ are polar coordinates, x_0 is the surging amplitude and finally, ϕ are the phase angles for each motion. From equations 7 and 8, it can be deduced that plunging motion is strictly a vertical oscillation. Pitching motion is rotational since neither equation 9 nor 10 is equal to zero. Similarly, from equations 12 and 13 surging is a purely horizontal motion.

Reduced frequency k is found by:

$$k = \frac{\pi f \bar{c}}{U_\infty} \quad (14)$$

where f is the frequency, $\bar{c}$ is the mean aerodynamic chord and U_∞ is the freestream velocity. Two other critical variables considering the aerodynamic performance of the wings are Reynolds number and Strouhal number, which equations are given below respectively.

$$Re = \frac{\rho U_\infty \bar{c}}{\mu} \quad (15)$$

$$St = \frac{2kh}{\pi} \quad (16)$$

where ρ is the density of the air and μ is the kinematic viscosity of the air for Reynolds number.

2.3 Unsteady Aerodynamic Mechanisms

At the start of Section 1.2, it is explained that aerodynamic forces are generated through unsteady aerodynamics by flapping insects when compared to fixed-wing or rotary-wing aircraft, which use conventional aerodynamics. In this section, different mechanisms of unsteady aerodynamics which are used by insects when flapping are explained in more detail.

2.3.1 Clap and Fling Mechanism

The clap and fling mechanism can be divided into two different phases. During the clap, phase wings come closer and during the fling phase, wings move away from each other by rotating around the trailing edge.

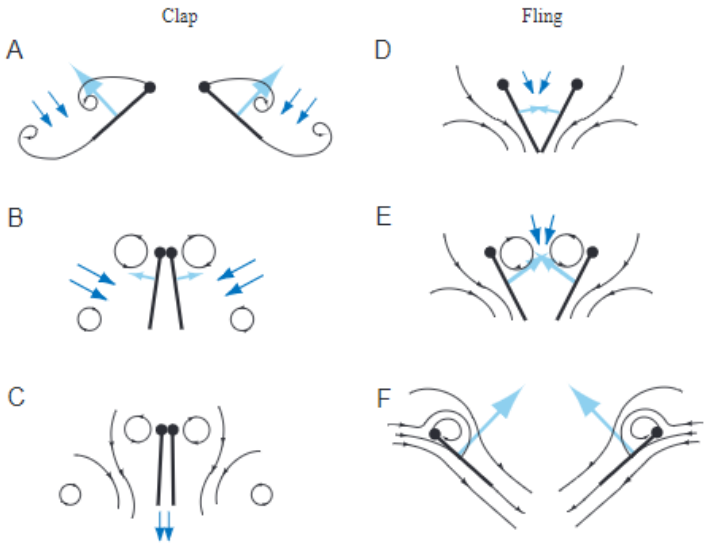

Figure 2.11: Clap (A-C) and Fling (D-F) Mechanism [11]

In figure 2.11, the mechanism is shown in detail. The left-hand side column of the figure demonstrates the clapping phase (A-C) and the right-hand side demonstrates

the fling phase (D-F). Black, dark blue, and light blue arrows indicate flow lines, induced velocity, and the net force acting on the wing respectively.

The clap starts with two wings moving towards each other and the first contact is made at the leading edges in figure 2.11a. After initial touch wings start to rotate around their corresponding leading edges. Due to this rotation trailing edges get closer and two counter-rotating vortices are shed. Vortices shed from trailing edges cancel each other out as shown in figure 2.11b. Finally in figure 2.11c, due to clapping air between wings bleed outwards.

Afterward, fling starts immediately by leading edges moving away from each other and air fills the space between wings in figure 2.11d. Leading edges' outwards movement increases the circulation around wings in figure 2.11e and stronger new leading-edge vortices form as shown in figure 2.11f. Coincidentally two mechanisms collaboratively increase the lift force generated by the insect flapping [11].

2.3.2 Leading Edge Vortex

As the angle of attack of the wing is increased flow over the wing separates after passing the leading-edge but reattaches before the trailing edge and flow separation occurs between the regions where flow detaches and reattaches. This low-pressure separation region creates a suction force. Subsequently, a leading-edge vortex appears in the separation zone in the upper surface of the wing. Generated lift is increased due to the wing's translational movement at high angles of attack since greater momentum facing downwards is exerted on the fluid. Leading-edge vortex is vital for insects because flapping motion occurs at high angles of attack.

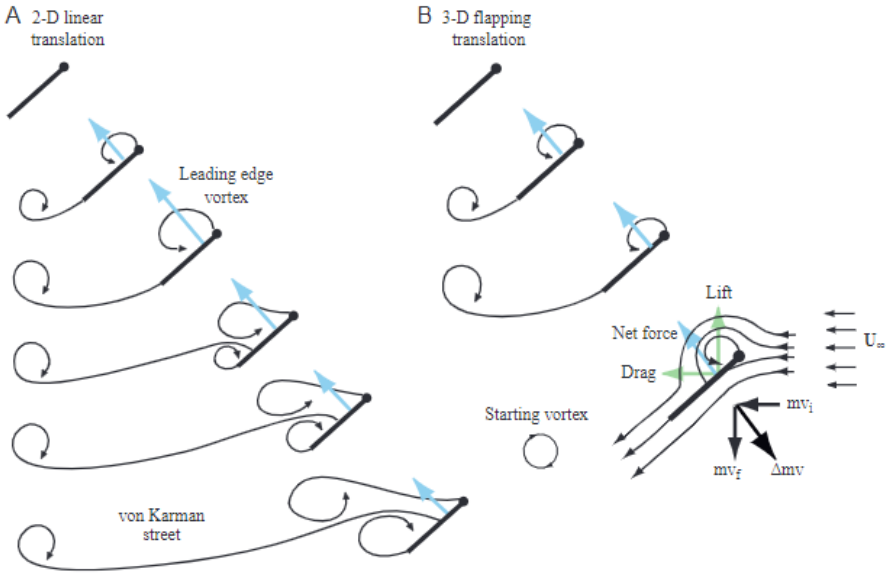

Figure 2.12: 2D LEV (A) and 3D LEV (B) Formation [11]

2D and 3D leading-edge vortex formations are shown in detail in figures 2.12a and 2.12b respectively. U_∞ is the freestream velocity, blue arrows indicate net aerodynamic force, and thin black arrows indicate flow directions in both figures whereas thick black and green arrows denote reactive aerodynamic forces on the wing and orthogonal lift and drag components respectively in figure 2.12b [11].

2.3.3 Wake Capture

This phenomenon, which is also known as wing-wake interactions, occurs as the wing reverses its stroke. In figure 2.13, a wing section is shown during stroke reversal in order to indicate the wake capture mechanism clearly. The net aerodynamic force acting on the wing is shown in light blue arrows, dark blue arrows indicate induced velocity direction and black arrows show flow directions with U_∞ being the freestream velocity.

Wing switches its motion from translation to rotation around its chordwise axis as shown in figure 2.13a. As the stroke is reversed vortices are shed from both leading and trailing edges in figure 2.13b. These vortices enhance the velocity field in the vicinity of the wing which can be seen in figures 2.13c. In figure 2.13d wing stops

then reverse stroke. Next, the wing encounters the velocity field which was previously enhanced by vortices shed by itself in figure 2.13e. Finally, in figure 2.13f, the process is ready to repeat itself again but in the opposite direction. This encounter between the wing and its wake increases the aerodynamic force [11].

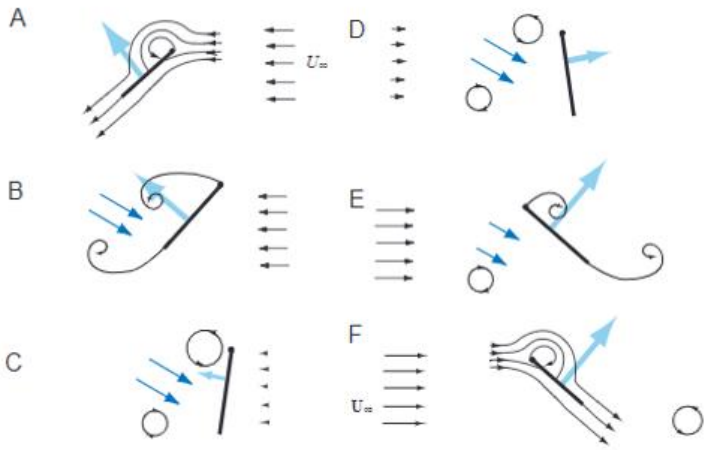

Figure 2.13: Wake Capture Mechanism [11]

2.3.4 Added Mass Effect

The final unsteady aerodynamic mechanism is named added mass effect. Unlike the previous three mechanisms, added mass effect's force is non-circulatory. While the wing flaps its velocity and acceleration change constantly. These continuous changes in the wing's movement affect the surrounding fluid, causing it to accelerate and decelerate along with the wing. Subsequently, this moving fluid changes the pressure around the wing and the force on the wing caused by the moving fluid is named added mass effect. Since this non-circulatory force is generally present with other circulatory forces, it is hard to measure them separately. To solve this problem, added mass force is usually assumed as quasi-steady and a time-invariant added mass coefficient is introduced when modeling [11].

CHAPTER 3

FOUR BAR MECHANISM

In addition to flapping-wing flight, another important point to understand in FWMAV design is mechanisms. They can be defined as a system of moving, rotating, and stationary parts working in harmony towards achieving a certain goal. The importance of mechanisms is first mentioned in section 1.1 and figure 1.3 shows that it is the most widely researched area in FWMAV related topics.

Flapping action is done with the help of a mechanism in all FWMAVs thus it is appropriate to assume the flapping mechanism is the heart of the FWMAVs. Flapping can be done in various ways depending on the species that the FWMAV is modeled after and it requires a suitable mechanism that can perform the desired flapping motion.

Since the FWMAVs are very complicated by nature, any kind of simplification is welcomed. Four bar mechanisms, also known as four-bar linkages, are generally regarded as the simplest movable closed-chain mechanisms. They consist of four bars or links and they are connected in a loop by four joints [78]. In addition to their simplicity, four-bar mechanisms prove to be very effective in terms of performance in FWMAV applications. As a result of these factors, four-bar linkages are the most widely used type of mechanism used in FWMAV applications.

There are three kinds of four-bar mechanisms, which are planar, spherical, and spatial. If the joints are configured in a way that allows the linkages to move parallelly, the mechanism is called a planar four-bar linkage which is the type of four-bar linkage used in the current study.

3.1 Planar Four-Bar Mechanisms

Planar four-bar linkages consist of four links and four joints and have one degree of freedom. Joints may be either revolute (denoted by R) or prismatic (denoted by P). Revolute joints make a rotational motion and prismatic joints make translational motion i.e., sliding. In figure 3.1, a simple four-bar linkage, which is also designed and used in the current study, is shown along with its component names. The ground is considered as link 1 and it is connected to both crank (link 2 in red) and rocker (link 4 in yellow). Link 3 in green is the coupler and in addition to four linkages, there are four revolute joints at both ends of the links, which are denoted by R in the mechanism.

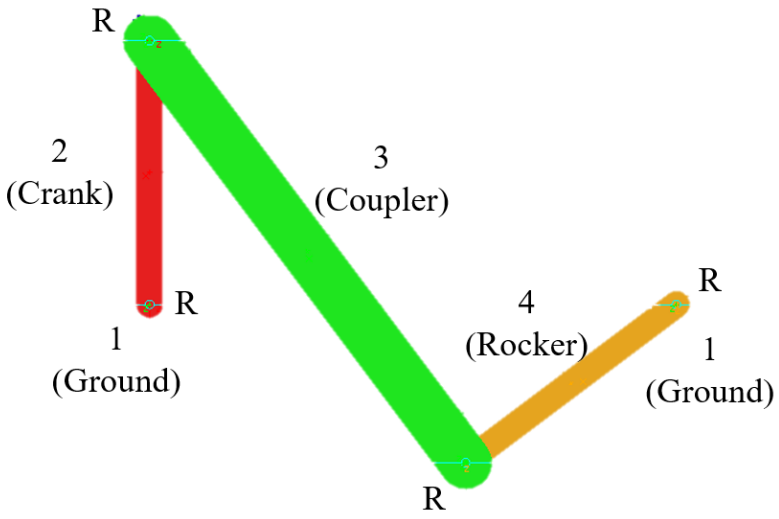

Figure 3.1: Four Bar Mechanism

There are four types of planar four-bar mechanisms which are

- Crank Rocker Mechanism: The link, which is fixed to the ground via a revolute joint, also capable of rotating 360 degrees is named crank (driving link). One end of the crank is fixed to the ground as stated and the other end is connected to the coupler link. The coupler link is the connector between the crank and rocker. Rocker link only moves back and forth in a confined space which depends on the link lengths. Usually, the rocker link is connected to the ground as well.

- Double Crank Mechanism: Both links connected to the ground are capable of full 360 degrees of rotation. In this mechanism, continuous motion is obtained and both links connected to the ground can act as cranks. This type of mechanism is also known as a drag link.
- Double Rocker Mechanism: Both links connected to the ground are not capable of doing a 360-degree revolution and only move between two points. No continuous motion is obtained in this type of mechanism since both links connected to the ground act as rocker links.
- Parallelogram Linkage: Lengths of both links fixed to the ground are equal, as well as the coupler link's length and the distance between ground points, are equal to each other. Continuous motion is possible in parallelogram linkage.

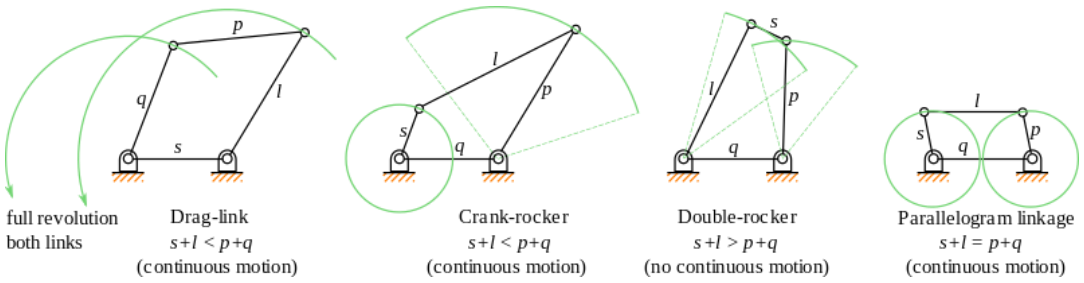

Figure 3.2: Types of Planar Four-Bar Mechanisms [79]

In figure 3.2, types of planar four-bar linkages are shown. Link names are given as *s*, *l*, *p*, and *q*. Letters *s* and *l* denote the shortest and longest links respectively and *p* and *q* denote the other two links. Green lines, circles, and arcs denote the movement of the associated link.

To obtain a smooth motion, the mechanism must operate effortlessly. Four bar mechanisms must satisfy Grashof's theorem to obtain the desired smooth motion. The theorem states that if the sum of the shortest and longest links' lengths is less than or equal to the sum of the other two links' lengths, then the shortest link can do a 360 rotation motion. The equation for Grashof's theorem is:

$$s + l \leq p + q \tag{17}$$

If the relation $s + l < p + q$ is satisfied, double crank (drag link), crank-rocker and double rocker mechanisms are obtainable depending on the link lengths. If the shortest link is fixed to the ground, then it is a double crank mechanism. If one of the links connecting to the rocker link is fixed, it is a crank rocker mechanism. Otherwise, if the link across the shortest link is fixed to the ground, a double rocker mechanism is obtained.

If the relation $s + l = p + q$ is satisfied parallelogram linkage is obtained. Since link lengths are equal in this type of mechanism, there are two critical points where the motion is unpredictable. These critical points occur when the driving link is at either 0^o or 180^o where the mechanism resembles a straight line. In situations where equation 17 is not satisfied such, that $s + l > p + q$, it is not possible to obtain a mechanism other than a double rocker.

3.2 Position, Velocity, and Angular Acceleration Analyses

Mechanism analysis can be done in a variety of ways. Three methods stand out, which are trigonometric analysis, analysis by complex numbers, and vector analysis. These widely used three methods help determine the position equation of the links and by differentiating the position equation once and twice, equations for velocity and acceleration equations are obtained respectively.

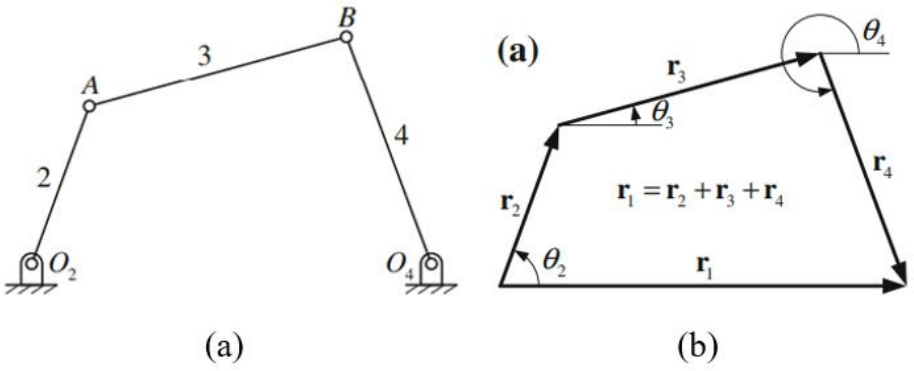

Figure 3.3: Four-Bar Mechanism (a) and Loop Closure Equation (b) [80]

Analyzing with complex numbers and vectors is easier when compared to trigonometric means since equations become too complicated and hard to solve when differentiated for velocity and acceleration analysis. Using complex numbers and vectors are similar as well. Both methods start with identifying the lengths and angles of links, which are both denoted in figure 3.3. Distance between fixed points O_2 and O_4 (r_1 or link 1) is known as the fixed link. θ_1 is the input angle and θ_3 is the output angle. As a result, a closed-loop vector equation is formed from a four-bar linkage.

Analyzing using complex numbers is also known as Raven's method. In this method, after obtaining the closed-loop equation for the mechanism vectors are replaced by complex numbers. Complex numbers of the closed-loop equation are expressed in exponential form and then converted into trigonometric form. The final step before solving for unknowns is separating the real and imaginary parts of the closed-loop equation [80].

3.2.1 Angular Position of Links

Since the lengths of the links r_1, r_2, r_3 and r_4 are known along with the position, velocity, and acceleration of the link 2 (input link or crank), $\theta_2, \omega_2, \alpha_2$ respectively, positions, velocities and accelerations of link 3 and 4 ($\theta_3, \omega_3, \alpha_3$ and $\theta_4, \omega_4, \alpha_4$ respectively) can be calculated.

To obtain angular positions of the links using Raven's method, consider the vector loop equation given in figure 23b:

$$r_1 = r_2 + r_3 + r_4 \tag{18}$$

Equation 18 expressed in complex exponential form is given as:

$$r_1 e^{i\theta_1} = r_2 e^{i\theta_2} + r_3 e^{i\theta_3} + r_4 e^{i\theta_4} \tag{19}$$

Expanding equation 19, the following equation in trigonometric form is obtained:

$$r_1(cos\theta_1 + isin\theta_1) = r_2(cos\theta_2 + isin\theta_2) + r_3(cos\theta_3 + isin\theta_3) + r_4(cos\theta_4 + isin\theta_4) \tag{20}$$

Two equation systems with two unknowns are obtained when real and imaginary components of equation 20 are separated:

$$r_1 cos\theta_1 = r_2 cos\theta_2 + r_3 cos\theta_3 + r_4 cos\theta_4 \quad (21)$$

$$r_1 sin\theta_1 = r_2 sin\theta_2 + r_3 sin\theta_3 + r_4 sin\theta_4 \quad (22)$$

From equations 21 and 22, two unknowns θ_3 and θ_4 can be obtained.

The angular positions of links are always the same with respect to each other if proportions of link lengths stay the same no matter the size of the mechanism [81].

Alternatively, angular positions can be found by the trigonometric method. Before constructing the loop closure equation, a line can be drawn between points O_4 and A to obtain two triangles, shown in figure 3.4.

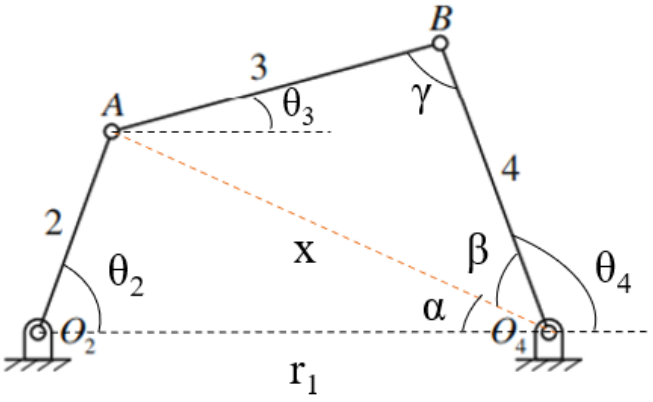

Figure 3.4: Trigonometric Method for Position Analysis

Since r_1, r_2 and θ_2 is known, cosine theorem can be applied in the AO_2O_4 triangle in order to find distance x and then angle α. Distance x is given by the following equation:

$$x^2 = r_1^2 + r_2^2 - 2r_1 r_2 cos\theta_2 \quad (23)$$

After finding x, angle α is given by:

$$\alpha' = cos^{-1}\left[\frac{(r_1^2 + x^2 - r_2^2)}{2r_1 x}\right] \quad (24)$$

$$\alpha = \pi - \alpha' \tag{25}$$

Again cosine theorem can now be applied to BAO_4 triangle. For finding θ_4:

$$\beta = cos^{-1}\left[\frac{r_4^2 + x^2 - r_3^2}{2r_4 x}\right] \tag{26}$$

$$\theta_4 = \pi - (\alpha + \beta) \tag{27}$$

For finding θ_3:

$$\gamma = cos^{-1}\left[\frac{r_3^2 + r_4^2 - r_3^2}{2r_1 x}\right] \tag{28}$$

$$\theta_3 = \theta_4 - \gamma \tag{29}$$

Equation 19 can be written using both methods as shown, leading to the same result. However, velocity and acceleration equations are shown in next two sections using Raven's method only since as stated before trigonometric equations become too complicated to solve when differentiated.

3.2.2 Angular Velocity of Links

When vector loop (equation 19) is differentiated, the following equation is obtained considering $\theta_1 = 0$:

$$r_1 = r_2 e^{i\theta_2} + r_3 e^{i\theta_3} + r_4 e^{i\theta_4} \tag{30}$$

After differentiating with respect to time:

$$0 = ir_2\omega_2 e^{i\theta_2} + ir_3\omega_3 e^{i\theta_3} + ir_4\omega_4 e^{i\theta_4} \tag{31}$$

After writing the equation 31 in a trigonometric form similar to equation 20 and separating it into real and imaginary components respectively:

$$0 = -r_2\omega_2 sin\theta_2 - r_3\omega_3 sin\theta_3 - r_4\omega_4 sin\theta_4 \tag{32}$$

$$0 = r_2\omega_2 cos\theta_2 + r_3\omega_3 cos\theta_3 + r_4\omega_4 cos\theta_4 \tag{33}$$

Finally, angular velocities of links 3 and 4 are found respectively as:

$$\omega_3 = \frac{-r_2 \sin(\theta_2 - \theta_4)}{r_3 \sin(\theta_3 - \theta_4)} \omega_2 \quad (34)$$

$$\omega_4 = \frac{r_2 \sin(\theta_2 - \theta_3)}{r_4 \sin(\theta_3 - \theta_4)} \omega_2 \quad (35)$$

Using equations 34 and 35, angular velocities of coupler and rocker links can be calculated by plugging in the known variables, which are position and angular velocity of crank θ_2 and ω_2 respectively, previously found angular positions of coupler and rocker links θ_3 and θ_4 and finally link lengths r_1, r_2, r_3, r_4.

3.2.3 Angular Acceleration of Links

Differentiate the vector loop equation again in order to find angular accelerations α_3 and α_4 for links 3 and 4 respectively. Following similar steps as in finding the position and angular velocity equations, when equation 31 is differentiated following equation is obtained:

$$0 = -r_2\omega_2^2 e^{i\theta_2} + ir_2\alpha_2 e^{i\theta_2} - r_3\omega_3^2 e^{i\theta_3} + ir_3\alpha_3 e^{i\theta_3} - r_4\omega_4^2 e^{i\theta_4} + ir_4\alpha_4 e^{i\theta_4} \quad (36)$$

When seperated into real and imaginary parts:

$$0 = -r_2\omega_2^2 cos\theta_2 - r_2\alpha_2 sin\theta_2 - r_3\omega_3^2 cos\theta_3 - r_4\alpha_4 sin\theta_4 - r_4\omega_4^2 cos\theta_4 - r_4\alpha_4 sin\theta_4 \quad (37)$$

$$0 = -r_2\omega_2^2 sin\theta_2 + r_2\alpha_2 cos\theta_2 - r_3\omega_3^2 sin\theta_3 + r_4\alpha_4 cos\theta_4 - r_4\omega_4^2 sin\theta_4 + r_4\alpha_4 cos\theta_4 \quad (38)$$

Finally, angular accelerations are found as:

$$\alpha_3 = \frac{\omega_3}{\omega_2}\alpha_2 - \frac{r_2\omega_2^2 \cos(\theta_2 - \theta_4) + r_3\omega_3^2 \cos(\theta_3 - \theta_4) + r_4\omega_4^2}{r_3 \sin(\theta_3 - \theta_4)} \quad (39)$$

$$\alpha_4 = \frac{\omega_4}{\omega_2}\alpha_2 - \frac{r_2\omega_2^2 \cos(\theta_2 - \theta_3) + r_4\omega_4^2 \cos(\theta_3 - \theta_4) + r_3\omega_3^2}{r_4 \sin(\theta_3 - \theta_4)} \quad (40)$$

Angular accelerations of coupler and rocker links are given by equations 39 and 40 respectively. Angular acceleration of crank ω_2 is plugged into equations along with the initially known variables and previously calculated variables from equations 34

and 35 [72]. From equations 34 and 35, it can be deduced that angular velocities of coupler and rocker links are dependent on the angular acceleration of the crank link. A similar deduction can be made by looking at equations 39 and 40 such that angular accelerations of links 2 and 3 are directly dependent on the angular acceleration of link 2.

3.3 Lemniscate Mechanism Design

To accurately imitate the flapping motion of insects, mechanism design is crucial. From the preliminary design step, the mechanism is intended to be a planar four-bar linkage. For increasing biomimicry, besides only doing a simple plunging motion of the insect wing, pitching is tried to be incorporated into the mechanism as well.

A planar four-bar linkage in the form of a parallelogram mechanism, operating as a crank rocker mechanism is designed based on the lemniscate mechanism shown in figure 3.5 [59]. Lemniscate mechanism can do a figure of eight shapes similar to an infinity curve (∞) as demonstrated by dashed lines in figure 3.5. By performing this figure of eight shapes, it is aimed that a motion similar to the stroke reversal of insect wings is obtained and both plunging and pitching motions are performed.

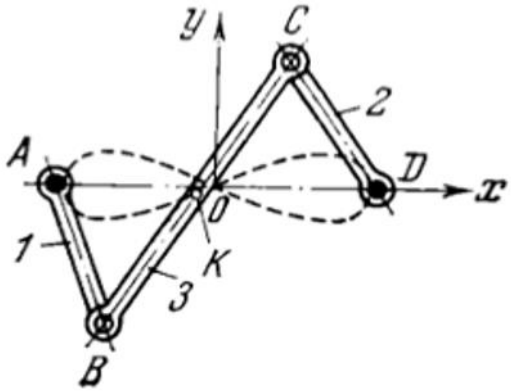

Figure 3.5: Lemniscate Mechanism [60]

In the above figure, point names and link numbers can be seen clearly. Mechanism is driven by link 1. Desired figure of eight shape is traced by the middle point (K) of

link 3 (BC) when links 1 (AB) and 2 (CD) are rotating in opposite directions. In order to obtain the desired figure of eight shape lengths must satisfy the following proportions:

$$AD = BC = 2b \tag{41}$$

$$AB = DC = a \tag{42}$$

$$a = \sqrt{2b} \tag{43}$$

The equation of the lemniscate shape traced by point K is given by the following relation:

$$(x^2 + y^2)^2 = a^2(x^2 - y^2) - 4b^2y^2 \tag{44}$$

Lemniscate mechanism is designed in flexible multibody dynamics software MSC Adams to perform the flapping motion. The mechanism is able to perform plunging and pitching motions as well as stroke reversal because it can trace a figure of eight shape with the middle point of its longest link.

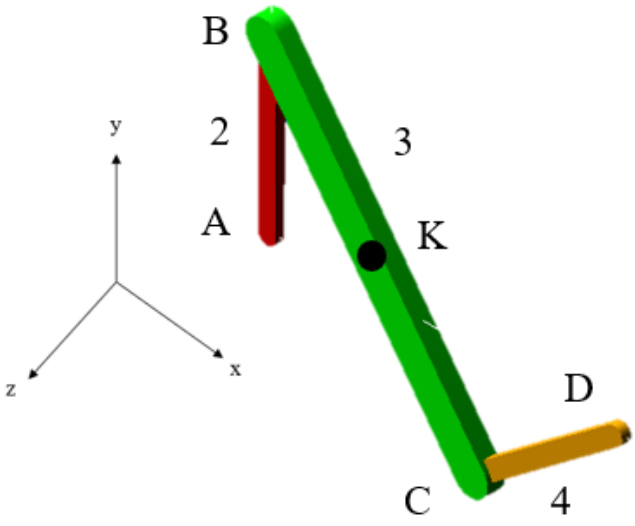

Figure 3.6: Isometric View of the Flapping Mechanism

In figure 3.6, an isometric view of the designed flapping mechanism can be seen along with the coordinate axes and link numbers. Points from figure 3.5 are also denoted in figure 3.6 for clearer demonstration but link numbers are different for the

designed linkage. Red and yellow links (short links) have the same length of 30 millimeters whereas the green link (long link) has a length of 60 millimeters. Distance between the short links' ground joints is also 60 mm. Link lengths are within the limits of FWMAV specifications from table 1. Material for all three links is chosen as steel. Structural and material properties of links taken from Adams software can be seen in table 3.1.

Table 3.1: Material and Structural Properties of Mechanism Links

	Short Links	**Long Link**
Length (x-axis)	30 mm	60 mm
Width (y-axis)	3 mm	6 mm
Depth (z-axis)	1.5 mm	3 mm
Material	Steel	Steel
Density	7801 kg/m^3	7801 kg/m3
Young's Modulus	2.07E+05 N/mm^2	2.07E+05 N/mm^2
Poisson's Ratio	0.29	0.29
Mass	1.135 g	9.075 g
Volume	145.43 mm^3	1163.44 mm^3
I_{xx}	9.97 kg.mm^2	3.19 kg.mm^2
I_{yy}	9.90 kg.mm^2	3.17 kg.mm^2
I_{zz}	1.04 kg.mm^2	3.35 kg.mm^2

3.3.1 Position, Velocity and Acceleration Analyses of the Mechanism

A test simulation is done using Adams software for determining the position, velocity, and acceleration of the center of mass for each link in the mechanism. The center of mass for each link is located at the midpoint of each link since they all have symmetrical shapes and uniformly distributed mass. Simulation is done for one rotation of the crank (red) link with a rotational speed of 60 rpm or 6.28315 rad/s (360 deg/s). Consequently, the duration of the simulation is 1 second and rotation is

in the clockwise direction. The initial angle of the crank is θ_2=90^o. Also, the simulation is conducted in a vacuum so only inertial forces are taken into consideration. Since simulation is done for one full rotation of crank with an elapsed time of 1 second, it corresponds to a flapping frequency of 1 Hz.

Firstly, the crank link (red-colored and labeled 2) is analyzed in terms of position, velocity, and acceleration. It is the driving link of the mechanism so the previously defined initial angle and angular speed input are concerned with this link. Origin is assumed to be at the ground joint of the crank link. As a result, negative values in all graphs indicate the negative regions of the coordinate system for position and negative direction for velocity and acceleration. Position, velocity, and acceleration values are all translational for all plots unless it is explicitly stated as rotational.

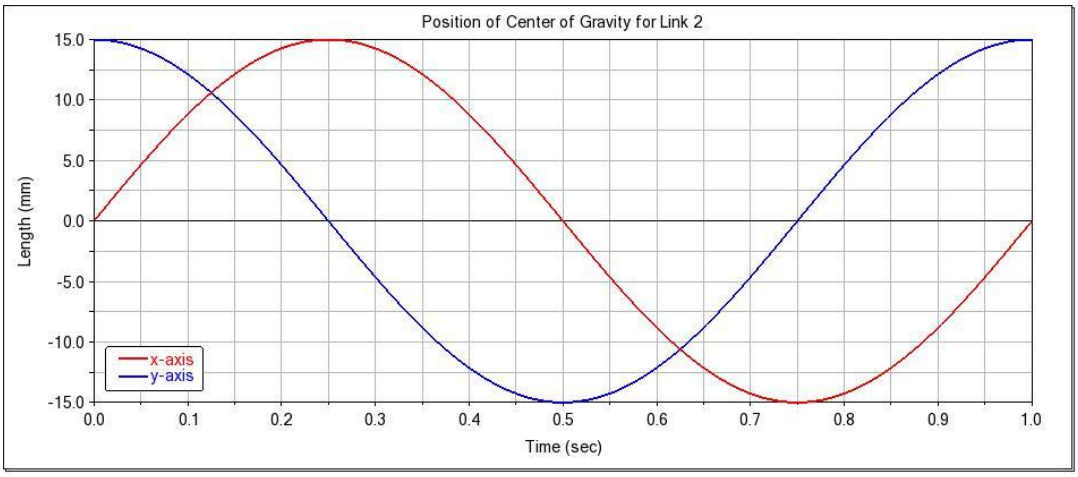

Figure 3.7: Position Analysis of Link 2

In figure 3.7, the x-axis and y-axis positions of the center of mass of link 2 are shown with red and blue lines respectively. Since the link is initially at rest perpendicular to the horizontal axis and the center of gravity is at the midpoint of the link x-axis component of the center of gravity is at zero and the y-axis component is at 15 mm. Crank becomes horizontal at 0.25 seconds since the position of the center of gravity becomes maximum for x-component and zero for y-component. At 0.5 points link is hanging upside down since curves are at the opposite positions with respect to their initial values. After 0.75 elapsed link is again horizontal but towards the opposite

direction and after 1 second it returns to its initial position, completing one full revolution.

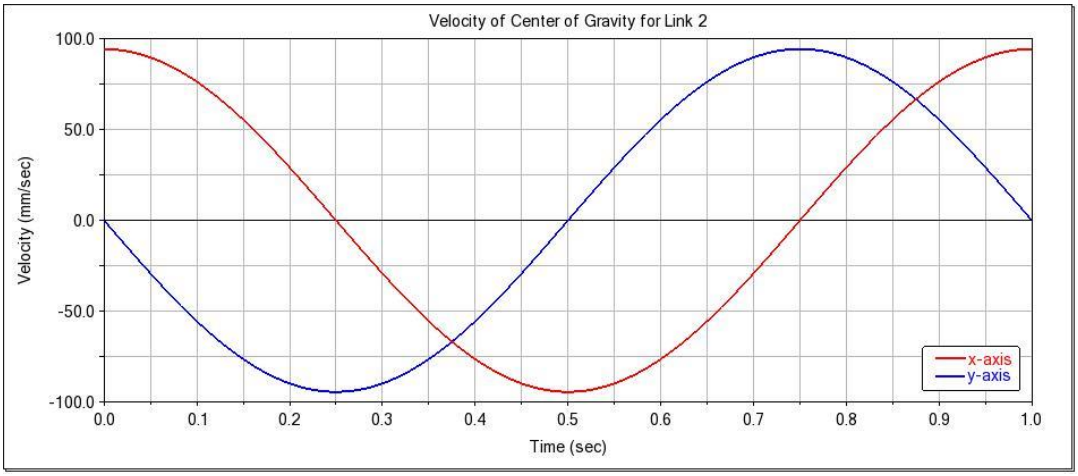

Figure 3.8: Velocity Analysis of Link 2

Next, velocity analysis is done for the crank's center of gravity, which is shown in figure 3.8 above. Again red and blue lines are used to denote x and y axes respectively. It can be seen that the velocity of the x-component is at a maximum amplitude of 100 mm/sec at times 0, 0.5, and 1 second where the y-component is zero consequently. Whereas at times 0.25 and 0.75, y-component is at maximum and x-component is zero. By looking at figures 3.7 and 3.8moses, it is seen that when displacement is maximum, velocity is minimum, and vice versa.

Finally, for link 2, acceleration analysis is done and results are presented in figure 3.9. The maximum amplitude of acceleration is 520 mm/s^2 for both x and y components. There are the local minimum and maximum values at quarter-second periods again in terms of amplitude. Since the mechanism is planar values for the z-component of the center of gravity are all zero. Only angular velocity of z-component is shown -360 deg/s since the revolution occurs around the z-axis in the clockwise direction and angular acceleration is zero since angular velocity is constant.

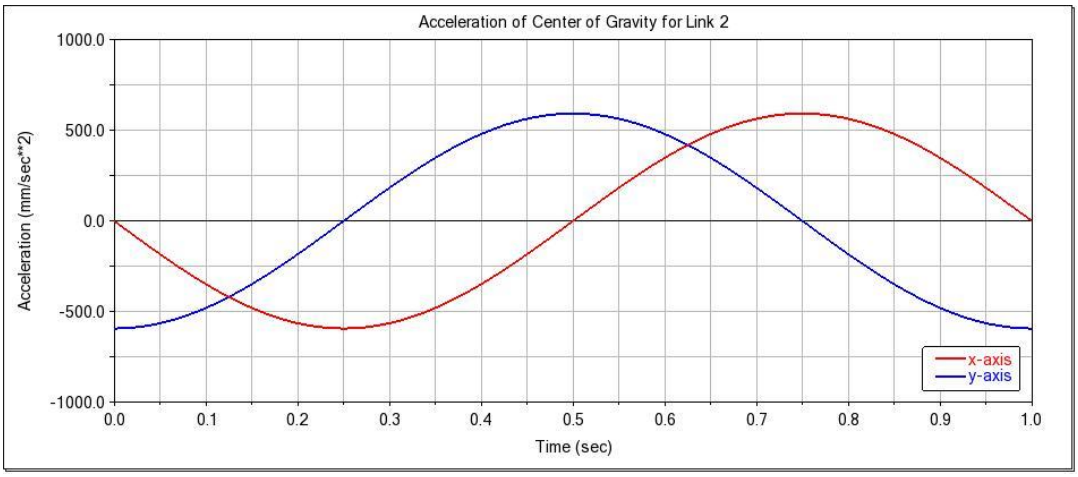

Figure 3.9: Acceleration Analysis of Link 2

The same analyses are done for the coupler link, which is colored green in figures 3.1 and 3.6 and numbered as 3. This link's middle point (center of gravity) traces the figure of eight shape during flapping. In figure 3.10 below, the position of link 3's center of gravity is plotted in both x and y-directions.

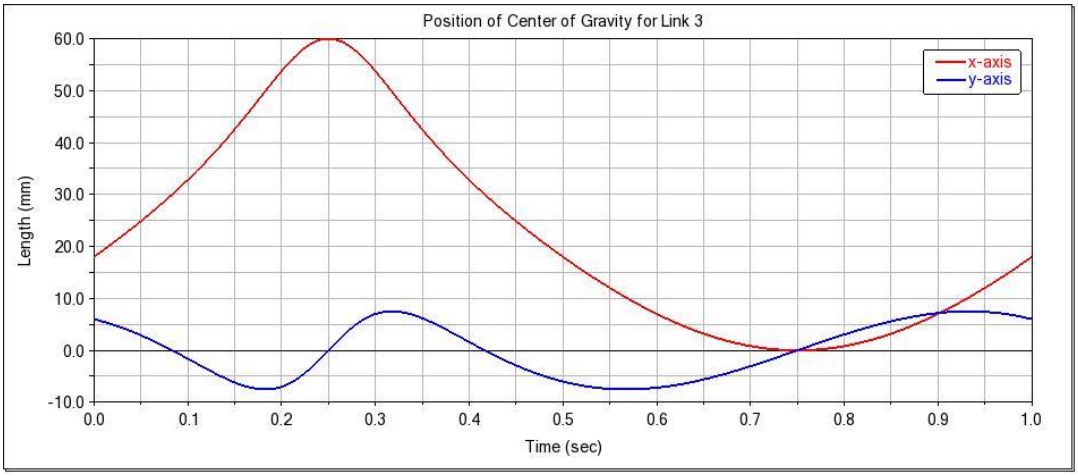

Figure 3.10: Position Analysis for Link 3

By looking at the initial x and y coordinates, it can be said that the coupler link is already inclined. At 0.25 seconds y-axis coordinate is zero. Whereas the x-axis coordinate is at 60 mm, the full length of the link, showing that it is horizontal. It can be deduced that it takes 0.25 (quarter cycle) for link 3 to become horizontal, simulation starts from halfway through the downstroke phase of flapping if a wing had been attached to the mechanism. Fluctuation of y-axis values shows the figure

of eight shape being traced while x-axis values gradually decrease after horizontal position.

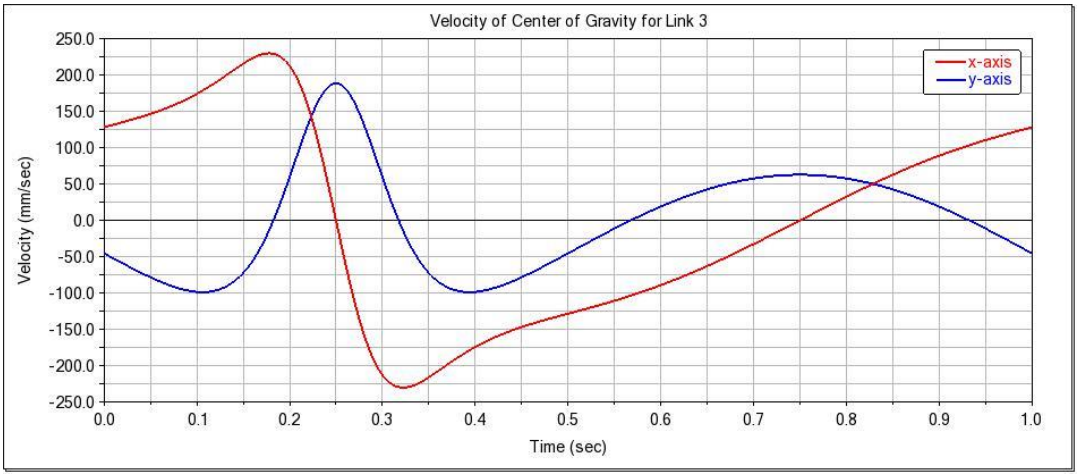

Figure 3.11: Velocity Analysis for Link 3

In figure 3.11, the velocity analysis of the coupler link is shown. By looking at the red line it can be understood that link 3 moves back and forth horizontally similar to the surging motion of the wing. Similarly, the blue line denotes that the center of gravity moves upwards and downwards vertically which resembles the plunging motion of the wing. Taking into consideration these two motions are happening simultaneously, the overall motion of the center of gravity of link 3 starts to resemble the desired figure of eight shape.

Instead of showing the translational acceleration of link 3's center of gravity, angular velocity and angular acceleration around the z-axis, which are more crucial information, are shown in figure 3.12. The vertical axis on the left-hand side is the angular velocity in deg/s and the vertical axis on the right-hand side is angular acceleration in deg/s^2. Since both velocity and acceleration around the z-axis are present for link 3, this indicates that link 3 has a motion like a seesaw. This rocking motion resembles the pitching of insect wings while flapping. The addition of this pitching motion to already present surging and plunging motions results in a smooth figure of eight shape created by all three motions happening at the same time in harmony.

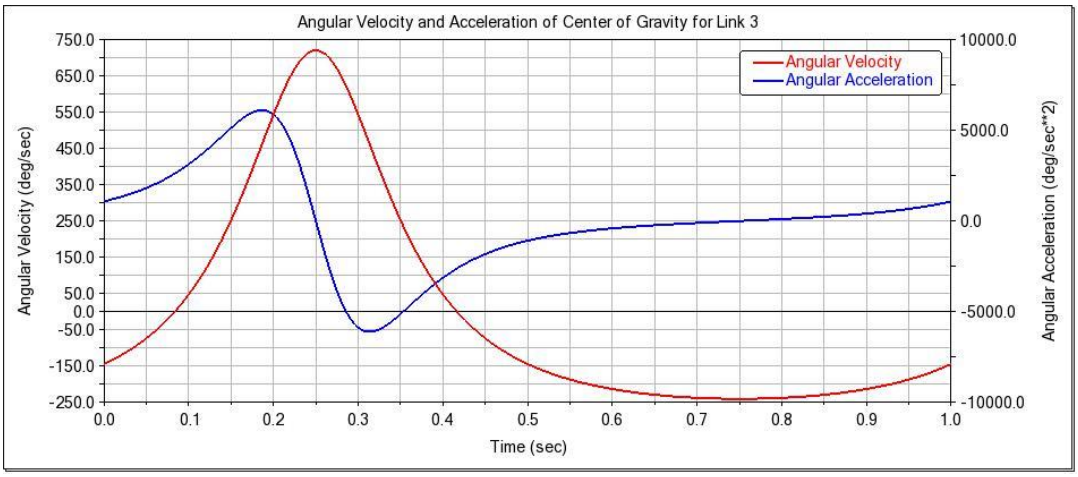

Figure 3.12: Angular Velocity and Acceleration Analyses for Link 3

Finally, results for the yellow link 4 are presented. Position analysis for link 4 is shown in below figure 3.13. It is different from the results from position analysis for link 2 given in figure 3.7 because their initial positions are different. Link 2 has an angle of θ_2=90^o whereas link 4 has an angle of θ_4=225^o approximately at t=0 seconds.

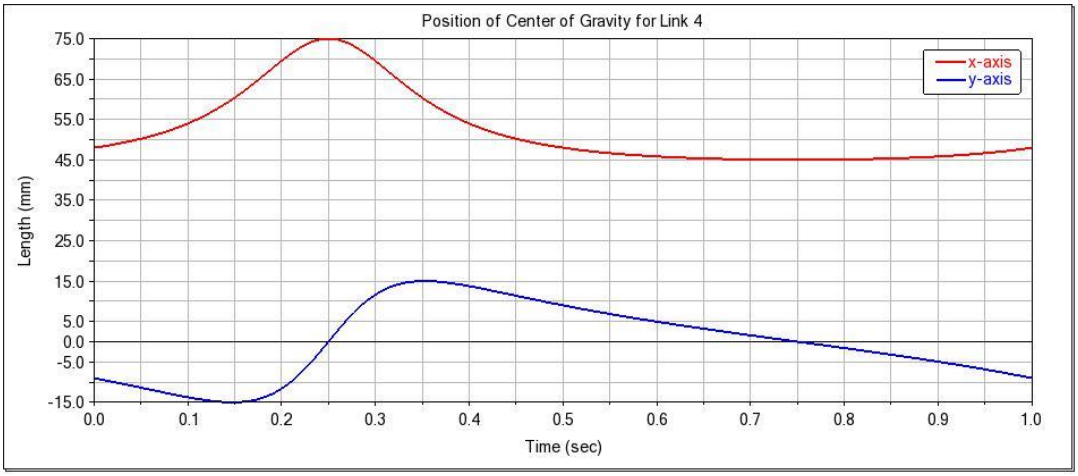

Figure 3.13: Position Analysis for Link 4

Translational velocity and accelerations of the x-axis component and y-axis component of the center of gravity for link 4 are presented in figure 3.14. Results of translational velocity and translational acceleration of the center of gravity of link 4 are very similar to the results of link 3. There is only a proportional change in

magnitudes caused by the length difference between links but other than that, all curves of link 4 have the same behavior as their counterparts from link 3.

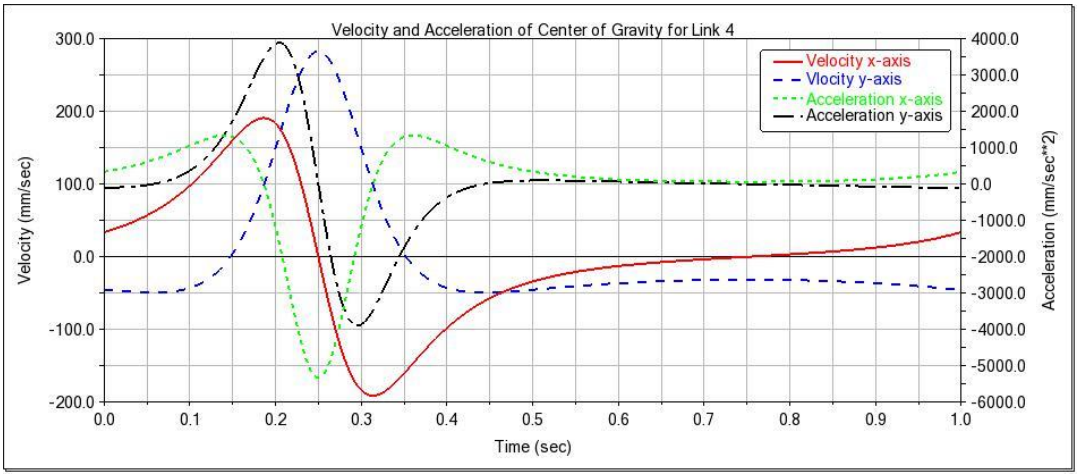

Figure 3.14: Translational Velocity and Acceleration Analyses for Link 4

In figure 3.15, angular velocity and acceleration around the z-axis are presented for link 4. It shows that even though link 2 had constant angular velocity and acceleration around the z-axis, links 3 and 4 have differing values.

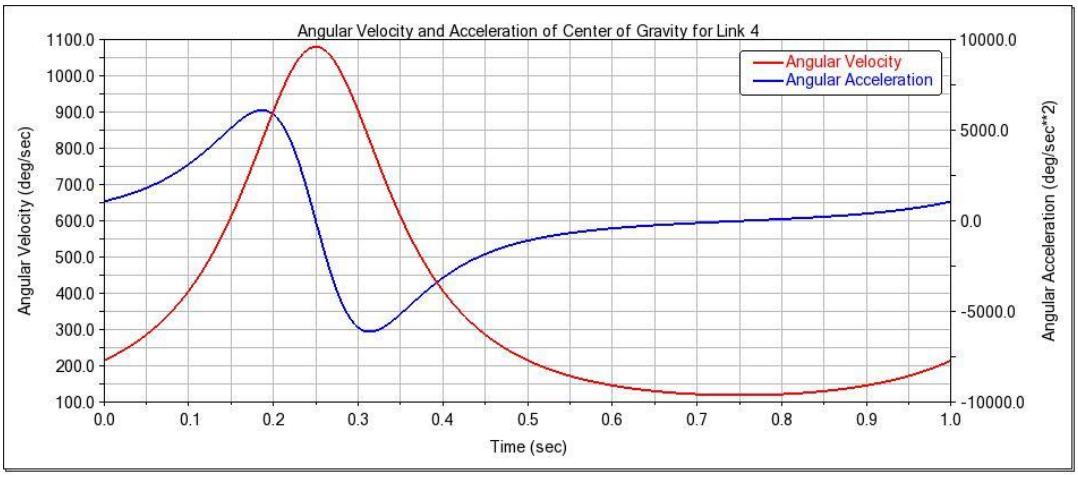

Figure 3.15: Angular Velocity and Acceleration Analyses for Link 4

When the results of figure 3.15 are compared with the results of figure 3.12, a similar correlation is observed. Plots have very similar curves with only different magnitudes as seen in figure 3.14 as well. Thus it can be concluded that translational velocity and acceleration analysis for link 3 yielded similar results.

As a result, by examining the motions of link 3, which the wing will be attached to, it is understood that it can perform surging, plunging, and pitching. Consequently, the center of gravity of the coupler link can successfully perform the desired figure of eight motion to mimic insect flapping.

CHAPTER 4

MODELING OF THE HAWKMOTH WING

The wing is crucial as much as the flapping mechanism for FWMAVs. Before attempting to manufacture a wing, it should be accurately modeled and simulated in a computer environment along with an accompanying mechanism to prevent further challenges, in terms of resources and time, during FWMAV's manufacturing phase.

After verifying that the designed flapping mechanism is capable of performing the desired figure of eight motion by simulations, the wing model is constructed and verified as well to be used alongside the mechanism. The hawkmoth is the chosen species for the wing model to be based upon because of the vast knowledge available in the literature.

The main aim is to make the wing model as accurate as possible. To achieve maximum accuracy to the biological wing, several structural properties are tried to be implemented into the model along with geometrical properties. Structural properties include the material properties of veins and membrane i.e. Young's modulus and Poisson's ratio. Layout and diameters of veins are also considered structural properties of wing whereas geometrical properties can be listed as shape, length, and camber.

The verification of the constructed wing model is done by using modal analysis with finite element method (FEM) and obtained numerical results are compared with other numerical and experimental results from the literature. Several wing models are constructed with different geometrical or structural properties to gain an insight into the effects of different variables on the wing model. These hawkmoth wing models with different structural and geometrical properties include but are not limited to, different vein diameters, presence of camber, carbon fiber veins, and mylar membrane instead of biological materials.

4.1 Species Selection

Manduca sexta, also known more commonly as hawkmoth, is one of the most widely studied insect species for FWMAV designs. They are often studied because they can be easily reproduced in controlled environments. Their large size contributes to their high observability. They are nocturnal insects, which means that they remain dormant during the daytime and become more active during nighttime. In controlled environments such as laboratories, lighting similar to sunlight is used for making the hawkmoth stay dormant which further provides easier observability. Another benefit is that they have a short lifespan, indicating they require little to no care.

Additionally, Ellington and Willmott state that with a stroke amplitude of approximately 120^{o} for hovering, the hawkmoth has a generalized wingbeat. It is also said that their flapping is consistent for both several different individuals and successive wingbeats for the same individual. Wind tunnel tests showed that the flapping frequency of hawkmoths is between 24.8 and 26.5 Hz, supporting the consistency claims [41]. Classification of *Manduca sexta* can be seen in table 4.1 as well as a figure of an adult female hawkmoth in figure 4.1.

Table 4.1: Manduca Sexta Classification

Kingdom	Animalia
Phylum	Arthropoda
Class	Insecta
Order	Lepidoptera
Family	Sphingidae
Genus	Manduca
Species	Manduca Sexta

Figure 4.1: An Adult Female Manduca Sexta [82]

From figure 4.1, it is seen that hawkmoths have four wings composed of 2 forewings and 2 hindwings. However, Jantzen and Eisner say that hindwings are not necessarily vital for flight [83]. The results of Zhao and Deng support this statement by explaining the power distribution focuses mainly on the forewings during flight [84]. Considering the results of these two studies, it is decided that only the forewing of the hawkmoth is to be modeled. Modeling only the forewing has additional benefits such as reducing weight, which is a critical factor for FWMAVs, and making the overall flapping mechanism simpler by eliminating a hindwing component.

4.1.1 Geometrical Study of the Hawkmoth Forewing

The geometrical properties of the hawkmoth wing must be known for the model to be accurate. Ellington and Willmott have investigated the morphological properties of three hawkmoths (two female and one male) [42]. Results are presented in table 4.2. The bodyweight of the specimens is denoted by m and in milligrams. Wing length is denoted by R and in millimeters. Aspect ratio is a dimensionless variable presented in equation 2. Mean aerodynamic chord is denoted by $\bar{c}$ and in millimeters. The final variable is the wing area denoted by S and its unit is millimeter square. Wing area and mean aerodynamic chord are calculated using equations 1 and 2.

Table 4.2: Hawkmoth Morphological Parameters [42]

	m (mg)	**R (mm)**	**AR**	**$\bar{c}$ (mm)**	**S (mm^2)**
M1 (Male)	1579	48.5	5.28	18.4	891
F1 (Female)	1648	51.9	5.65	18.4	953.5
F2 (Female)	1995	52.1	5.52	18.88	983.5

Hawkmoth body is divided into seven anatomical parts by O'Hara and each body part's contribution to overall insect mass is investigated. These seven parts are four individual wings (left and right forewings and hindwings), thorax, abdomen, and head. 30 individual hawkmoths are weighed. The average weight of a hawkmoth is found as 1.55 grams. The average weight of forewings is 34.6 milligrams (mg) and constitutes 2.23% of the total mass whereas hindwings only weigh 12 mg on average and make up 0.78% of the total mass of the insect [53].

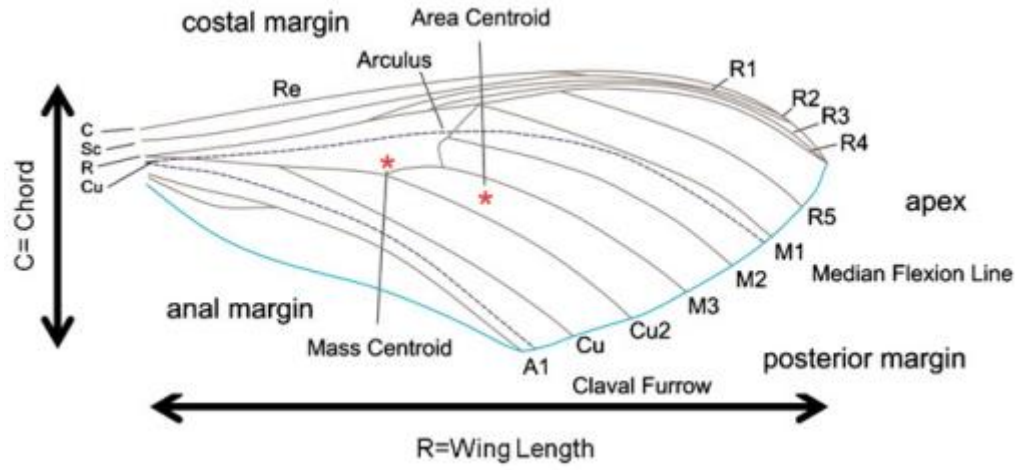

Figure 4.2: Venation Layout of Hawkmoth Forewing [53]

The venation layout of the hawkmoth's forewing is presented in figure 4.2. Veins are named according to the vein grouping presented in figure 2.5. Area and mass

centroids are marked on the wing with red asterisks. The median flexion line is also denoted where the wing cambers around while flapping. Detailed area properties of the hawkmoth forewing are presented in table 4.3 obtained from the same 30 specimens used to determine mass properties.

Table 4.3: Hawkmoth Forewing Area Properties [53]

	AR	**S (mm^2)**	**Centroid X (mm)**	**Centroid Y**	**Length R (mm)**	**Chord C (mm)**
AVG	14.42	702.46	18.61	14.046	50.18	22.97
STD	0.44	99.20	7.65	5.164	3.53	5.31
MAX	15.46	896.06	29.89	20.708	57.85	32.83
MIN	13.82	514	8.61	7.607	42.59	16.64

Aspect ratios, wing areas, wing, and chord lengths are given in table 4.2 as well as the x-axis and y-axis coordinates of the area centroid. Each of these variables has four different values, which are average, standard deviation, maximum and minimum values denoted by AVG, STD, MAX, and MIN respectively.

A different wing reference frame is used by O'Hara rather than the previously defined wing reference frame. Despite the direction of positive x-axis direction being the same, the positive Z_W-axis defined in the wing reference frame is denoted as positive y-axis by O'Hara.

The aspect ratio and total wing area measurements of Ellington and Willmott are different from O'Hara's measurements. Ellington and Willmott measured the entire wing of the hawkmoth including the hindwing whereas O'Hara only measured forewing properties. The total wing area of the hindwing is excluded which lowers S and consequently increases AR.

4.1.2 Structural Study of the Hawkmoth Wing

Elastic modulus (Young's modulus or modulus of elasticity) of the wing veins is tested by using a cost function to optimize the results of both numerical and experimental results by O'Hara. Experimental data is collected by laser vibrometry and modal analysis. Five vein sections are obtained from the leading edge radial or costal veins from five hawkmoth wings. Vein harvest locations are shown in figure 4.3. Three radial and two costal samples are placed in a clamp and inflicting damage to the samples is prevented by using a foam layer between the veins and the clamp. Then the samples are excited by a piezo shaker to find its first natural frequency one by one. Finite element analysis is used for determining the inner vein diameters by optically measuring the outer vein diameters with the help of a microscope, using the same five vein sections, which are previously extracted. Mass and volume of veins are determined afterward to find the density of the veins. Finally, elastic modulus data is obtained numerically from finite element analysis.

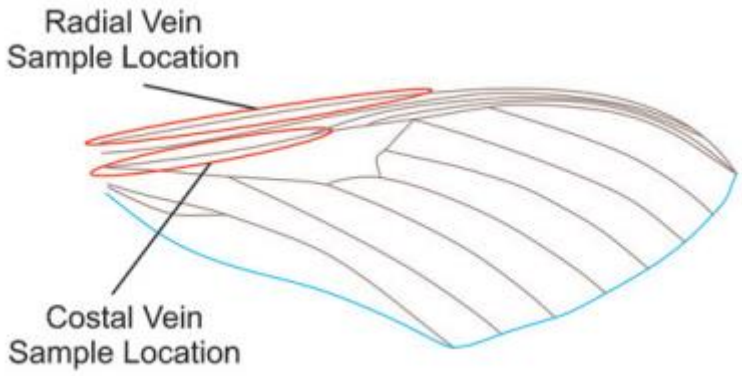

Figure 4.3: Vein Harvest Locations [53]

Minimization of cost function is used to determine the elastic modulus of veins by iteration. Used cost function can be written as:

$$J = \sum_{n=1}^{n_{modes}} \left[\frac{(\omega_{x,n})}{(\omega_{f,n})} - 1\right]^2 \quad (45)$$

Where $\omega_{x,n}$ is the experimental data values and $\omega_{f,n}$ is the numerical data values. Results are presented in table 4.4. Root OD is the outer diameter of the sample's vein

root and consequently, tip OD is the outer diameter of the sample's vein tip. Samples are listed from greatest outer vein diameter to smallest. Omega is the experimental data and density is the numerical data. AVG and STD represent average values and standard deviation respectively. It is concluded that the elastic modulus of the wings is 7.41 GPa and the result is between the expected range for similar insect species [53].

Table 4.4: Venation Elastic Modulus of the Hawkmoth [53]

	Root OD (μm)	**Tip OD (μm)**	**Length (μm)**	**Omega (Hz)**	**Density (g/cm^3)**	**E (GPa)**
Radial	500	476	15724	518	2.6925	6.23
Costal	432	365	13240	558	1.5151	7.82
Radial	418	391	14472	470	2.3956	8.20
Radial	413	337	13385	469	2.8963	7.63
Costal	432	320	15153	436	2.6292	7.17
AVG	-	-	-	-	2.4258	7.41
STD	-	-	-	-	0.5394	0.75

After founding the elastic modulus for the veins, the elastic modulus of the membrane is determined. Five regions on the wing membrane, where veins are not located, are chosen and the nanoindentation process is used. Nanoindentation is a technique used for measuring the hardness of materials with small volumes, in which holes in the scale of nanometers are punched in the material. Chosen regions on the wing are shown in figure 4.4 and a grid size of 5x5 with 25 μm of spacing is applied with a dent depth of 500 nm. Results for determining the membrane's elastic modulus are presented in table 4.5 [53].

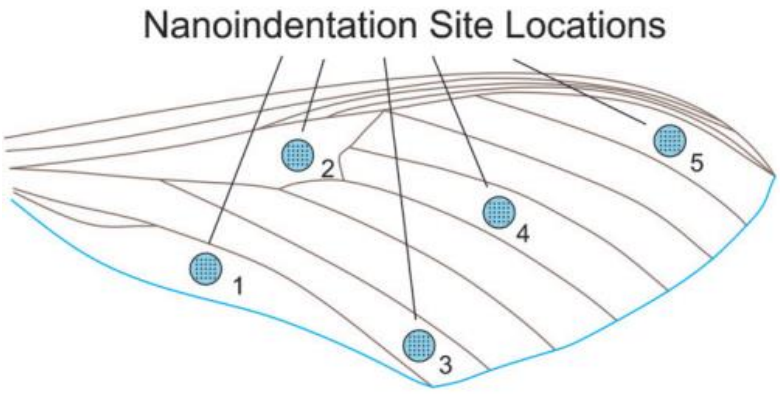

Figure 4.4: Nanoindentations on the Wing [53]

Table 4.5: Membrane Elastic Modulus of the Hawkmoth Wing [53]

Site	Site Mean (GPa)	Site STD (GPa)
1	1.91	1.04
2	4.77	1.21
3	1.49	1.29
4	2.59	0.73
5	1.47	0.98
Global Mean	2.45	-
Global STD	1.38	-

There are 25 different elastic modulus values for wing membrane per site. The mean of these values is taken for each site and presented in the site mean column in table 4.5 along with their corresponding standard deviations. As a result, a global mean membrane elastic modulus with a value of 2.45 GPa is calculated from each site's mean value. Again, this value for membrane elastic modulus is in the normal range for similar insect species [53].

Finding mean values of elastic modulus for both veins and membrane is important because CT (computed tomography) scans indicate that structural properties of hawkmoth wings can be considered homogeneous [85]. This means that once required structural properties such as but not limited to, density, elastic modulus, and

Poisson's ratio, are known, they can be used throughout the entire wing thus considerably facilitating the construction of the wing model.

4.1.3 Wing Kinematics of the Hawkmoth Wing

After gaining an insight into the hawkmoth wing's morphological parameters, wing kinematics while flapping is investigated briefly as a final step before starting to construct the wing model. One complete wingbeat cycle of hawkmoth during hovering is shown in figure 4.5. The cycle begins in figure 4.5a at the middle of the downstroke. The downstroke phase is demonstrated in figures 4.5a through 4.5h. It can be seen that the camber and twist of the wing increase gradually. Between figures 4.5h and 4.5i, stroke reversal occurs where the wing switches to supination from pronation and this concludes the downstroke phase. It is seen that the leading edge of the wing changes direction and starts moving in the opposite direction in figure 4.5i. This indicates that the upstroke phase has started. Wing increases its camber and twist during upstroke as well. The upstroke phase is denoted by figures 4.5i through 4.5m. The shaded wing areas in these depictions are the bottom side of the wing. After that, the first half of upstroke is shown between figures 4.5n to 4.5u. Second stroke reversal and change from supination to pronation occurs in figure 4.5n.

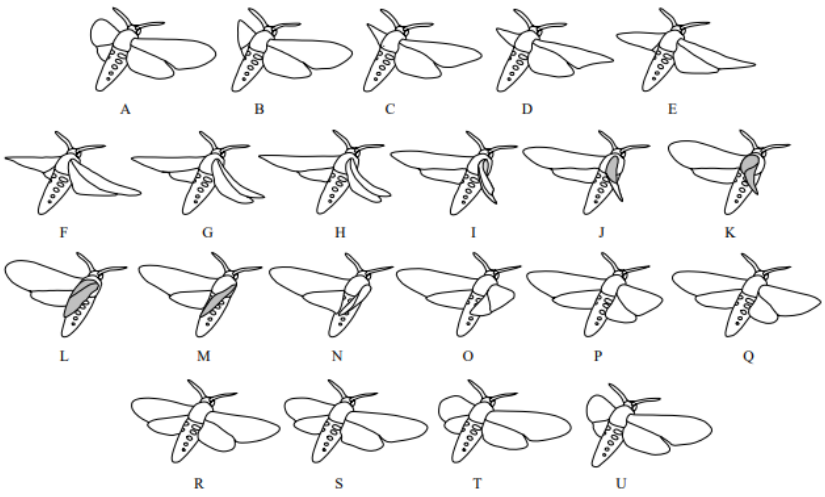

Figure 4.5: Flapping Cycle of Hawkmoth [40]

4.2 Hawkmoth Wing Model

In this section construction of the wing model and its verification case is presented. First, the geometry of the wing is created with appropriate dimensions and shape. Then, material properties are implemented in the constructed geometry. Verification of the constructed hawkmoth wing model is done by conducting a modal analysis using the finite element method and comparing its results with the experimental and numerical data obtained from the literature. Grid refinement study is done to make the results of the constructed model as accurate as possible to the results of verification cases.

In order to see the differences in modal analysis results caused by different morphological parameters such as different vein and membrane materials, different ratios of inner vein diameter to outer vein diameter, cambered or flat geometry, several appropriate models are constructed as well.

4.2.1 Wing Geometry

ANSYS SpaceClaim computer-aided drawing (CAD) program is used to compose the wing's geometry. Every literature source investigated indicates that the length (R) of a single wing of hawkmoth varies between 40-50 mm and chord (c) varies between 23-32 mm. Accordingly, the CAD drawing of the wing has a wing length of 50.03 millimeters and a chord of 23 millimeters while maintaining the overall shape of a hawkmoth forewing.

By using the maximum wing length and minimum chord length found in the literature, an aspect ratio of approximately 14 is obtained similar to the average value presented in table 4.3. The total wing area is of the wing model is calculated as 718.3746 mm^2 which is in good agreement with the literature results. Wing fixed reference frame is used, which is defined in chapter two and shown in detail in figure 2.7. Coordinate axes are slightly visible in figure 4.6 with the red arrow is denoting X_W-axis and the blue arrow is denoting Z_W-axis.

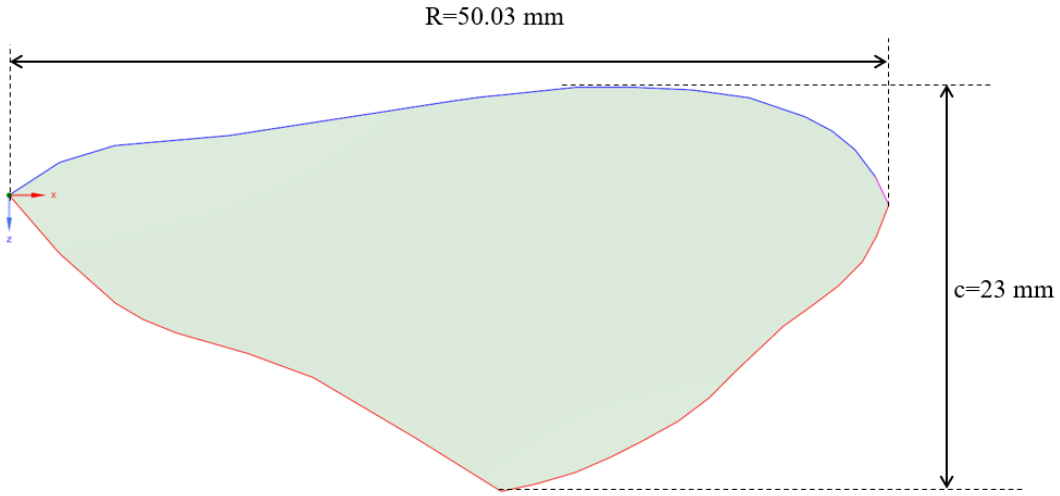

Figure 4.6: Length and Chord of the Wing Model

It is clear that from figure 4.6 that the wing length is the maximum distance between the wing root and wingtip. Both wing root and wingtip lie along the same line and the origin of the wing root has a perpendicular distance of 7 mm from the furthest point of the leading edge.

Wing camber is naturally observed in hawkmoths. Consequently, for increasing the biomimicry of the wing model, a camber is added to the wing. However, the wing camber is varied throughout the wing length. The median flexion line for the camber is the same line that the wing root and wingtip lie on. Camber has a shape of concave down at the wing root (origin point) with a maximum distance of 1 mm. At the wingtip, the camber is shaped as concave up with a maximum distance of 1 mm. Camber distance gradually changes along the centerline for the camber of the wing. The transition from concave down to concave up camber shape occurs approximately at 50% distance in the spanwise direction or approximately at 25 mm (middle point) wing length. The shape of the camber can be seen from the front and side in figure 4.7 and figure 4.8 respectively.

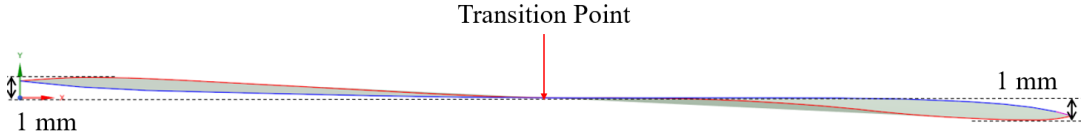

Figure 4.7: Front View of the Wing Camber

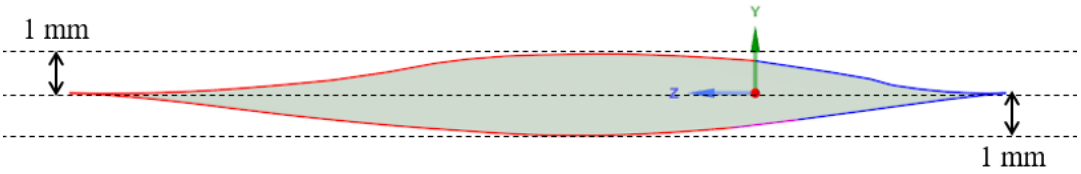

Figure 4.8: Side View of the Wing Camber

4.2.2 Wing Structure

After the initial geometrical shape of the wing, the model is laid out, structural properties are implemented on the wing model. Veins are placed on the wing and the remaining surface of the wing model is designated as the membrane. The nomenclature of the veins is shown in figure 4.9. Veins are named accordingly to figure 4.2. The trailing edge and wingtip have no veins running along the edges. All major veins start from the wing root (origin point) and branch out towards to wingtip laterally along the span.

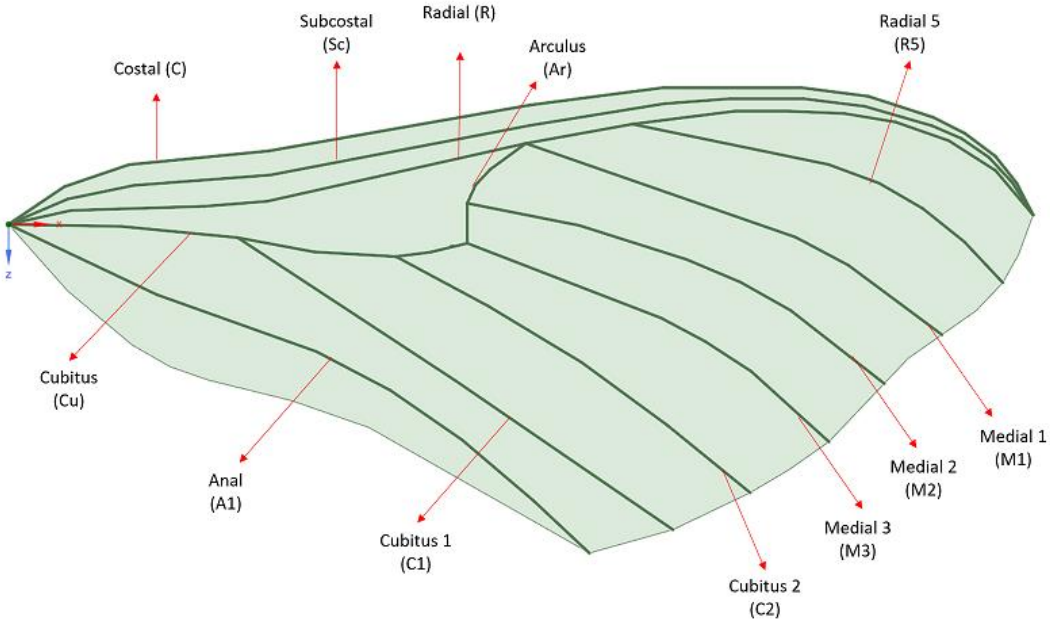

Figure 4.9: Vein Nomenclature of the Hawkmoth Wing Veins

Membrane thickness is decided as 0.05 millimeters (5 μm). Veins of the wing, which are modeled as circular tubes, are tapered from root to tip. Each vein in figure 4.9 has an outer vein wing root diameter and an inner vein wing tip diameter. Inner vein diameter is 70% of the outer vein diameter. The outer root and tip diameters for each vein are shown in table 4.6.

Table 4.6: Outer Vein Diameters

Vein Name	**Root Diameter (μm)**	**Tip Diameter (μm)**
Costal	250	20
Subcostal	250	20
Radial	250	20
Cubitus	250	130
Arculus	130	70
Radial 5	130	20
Medial 1	130	20
Medial 2	130	20
Medial 3	130	20
Cubitus 1	150	20
Cubitus 2	150	20
Anal	150	20

Ten different circular tubes are defined in SpaceClaim for modeling the taper of veins in more detail. Inner vein diameter to outer vein diameter is approximately 70%. Some inner diameter values are rounded off because SpaceClaim software does not allow long digits after a decimal point since the unit is already very small and in millimeter-scale. Each vein has sections of several of the ten circular tube cross-sections in the spanwise direction. For clearer demonstration purposes, circular tube sections are each assigned a color and marked on the wing geometry which can be seen in figure 4.10. Details for defined circular tube cross-sections are depicted in table 4.7 along with the assigned color.

Table 4.7: Circular Tube Cross Sections Information

Number	Outer Diameter (mm)	Inner Diameter (mm)	Color
Circular Tube 1	0.25	0.18	Lime
Circular Tube 2	0.23	0.16	Blue
Circular Tube 3	0.20	0.15	Cyan
Circular Tube 4	0.17	0.12	Magenta
Circular Tube 5	0.15	0.10	Yellow
Circular Tube 6	0.12	0.08	Orange
Circular Tube 7	0.10	0.07	Silver
Circular Tube 8	0.08	0.06	Black
Circular Tube 9	0.05	0.04	Green
Circular Tube 10	0.03	0.02	Red

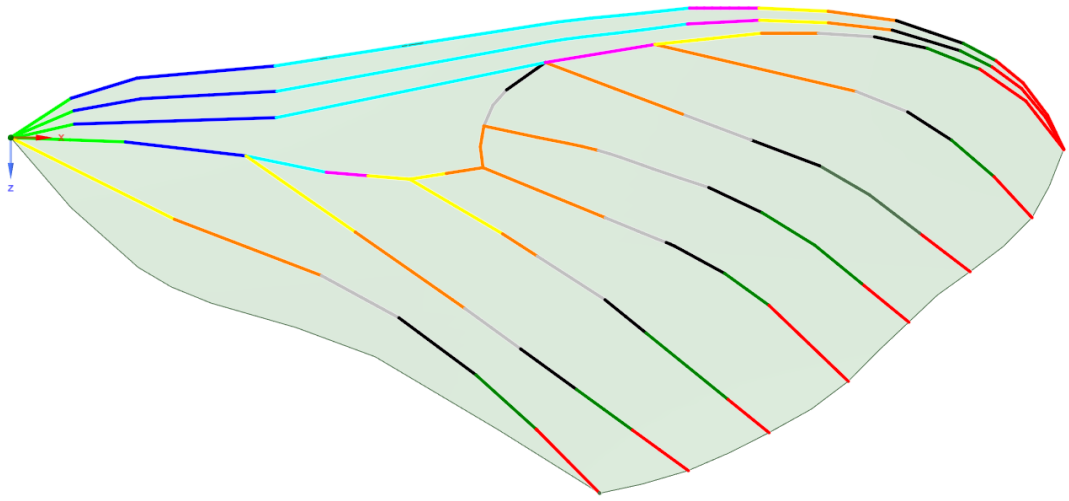

Figure 4.10: Color Index for Circular Cross Sections

Previously, it is stated that the hawkmoth wing is homogeneous in terms of structural properties. Thus, the material selected for representing vein structural properties can be applied to all veins regardless of their inner and outer diameters and positions on

the wing. The same rule applies to membrane material as well, meaning that the material properties are constant at every point on the wing membrane.

Vein and membrane material properties are taken from the morphological study conducted on biological hawkmoth wings by O'Hara, which is discussed in section 4.1.2 for the constructed model to imitate the actual hawkmoth wing. Material properties are given in table 4.7 for both veins and the membrane.

Table 4.8: Material Properties for Wing Veins and Membrane

	Density (kg/m^3)	**Young's Modulus (GPa)**	**Poisson's Ratio**
Wing Veins	2452	7.41	0.3
Wing Membrane	1400	2.40	0.3

4.2.3 Finite Element Model and Modal Analysis

The finite element method is a numerical technique, which is used in computer simulations, for solving the governing partial differential equations of boundary value problems quickly and as much accurately as possible to reality. Boundary value problems can be considered as solid mechanics (i.e. static and dynamic analysis, buckling analysis, and modal analysis), fluid mechanics, heat transfer, and electromagnetism.

Using FEM to solve a problem is called finite element analysis (FEA). There are three steps for FEA. The first step is called preprocessor where a mesh is applied to a previously constructed geometry and boundary conditions are defined. The second step is solver, where numerical calculations are done in nodes of the generated mesh. The final step is called postprocessor and obtained results can be seen.

In the present study, finite element analysis is used for modal analysis. The purpose of modal analysis is to find the natural frequencies of objects. When an object is excited with its natural frequency, the object starts to resonate. Resonance can be considered as small vibrations, which cause deformations over the body of the object over a certain time period. Those deformations are called mode shapes of the object for different natural frequencies. In modal analysis, no external force is applied to the finite element model. Instead, the aim is to obtain information about the natural characteristics of the object.

Modal analysis is used as a verification method in this study. Results of modal analysis (natural frequencies) are compared with other experimental and numerical modal analysis results from the literature to ensure the wing model is accurate. ANSYS Mechanical APDL computer software is chosen for constructing the finite element model and ANSYS Modal package of the software used for conducting the finite element analysis. The equation for calculating the deformation for modal analysis is given as:

$$[M]\{\ddot{\delta}\} + [K]\{\delta\} = 0 \tag{46}$$

In equation 46, M is the mass matrix, K is the rigidity matrix, δ is the displacement vector, and $\ddot{\delta}$ is the acceleration vector.

Veins are modeled using BEAM188 element and membrane is modeled using SHELL181 element in the ANSYS Mechanical APDL. BEAM188 element is suitable for analyzing slender to moderately thick beam structures. It is based on the Timoshenko beam theory, which means that it includes shear deformation effects. It can be a linear, quadratic, or cubic two-node element and has six degrees of freedom (three translational and three rotational) at each node. Additionally, a seventh degree of freedom, which is warping can be added for some cases. Linear, large rotation, and large strain nonlinear applications are suitable for BEAM188 element [86].

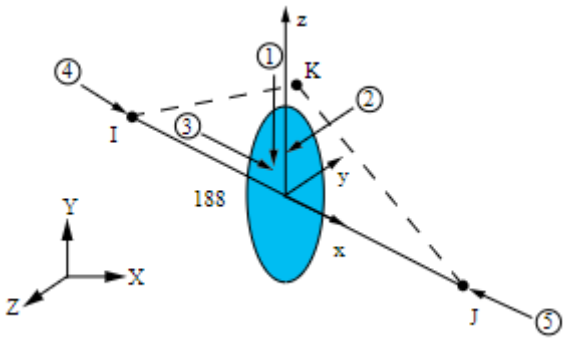

Figure 4.11: BEAM188 Element [86]

SHELL181 element is suitable for analyzing thin to moderately thick structures. It is a four-node element with six degrees of freedom at each node. However, if the membrane option is used each node has only three translational degrees of freedom, losing three rotational degrees of freedom. Like BEAM188 element, linear, large rotation and large strain nonlinear applications are suitable for SHELL181 element. Change in shell thickness is only taken into consideration in nonlinear analyses. Load stiffness effects of distributed pressures are accounted for. It can also be used for layered applications. The element allows for finite stretching [87].

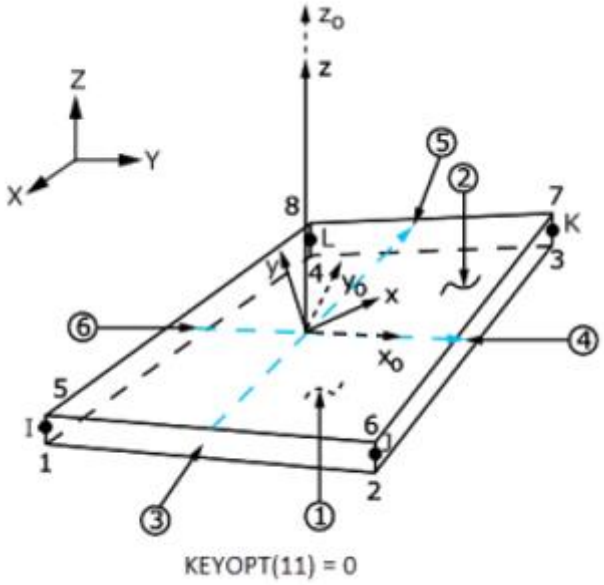

Figure 4.12: SHELL181 Element [87]

The finite element model of the wing has a fixed support at the origin point of the wing as a boundary condition shown in figure 4.13. Fixed support prevents the wing from moving in all of its six degrees of freedom.

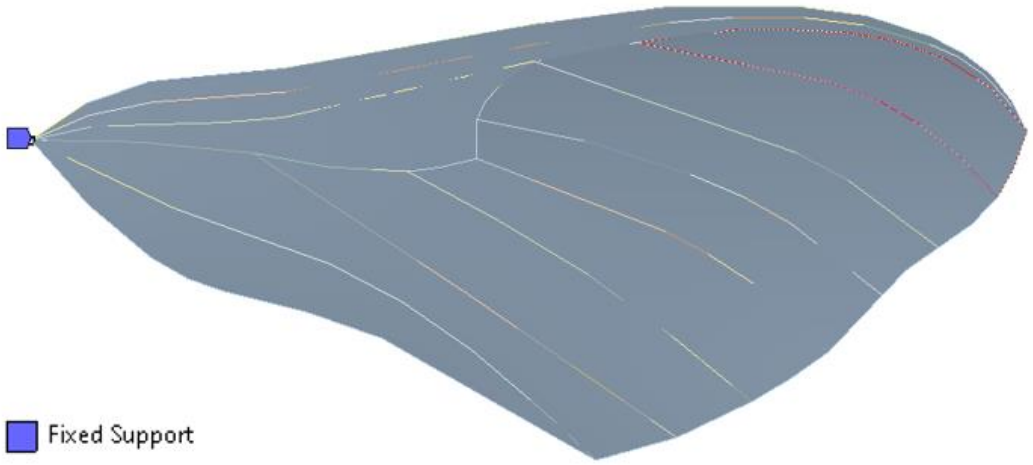

Figure 4.13: Fixed Support Location on the Wing

Modal analysis is conducted with three different meshes defined as fine, medium, and coarse with element sizes of 0.3, 0.4, and 0.5 millimeters respectively for grid refinement. Results of the first natural frequencies for each mesh are presented in Table 4.9. Bounding box dimensions for the FEM model are (50.39, 2.3, 23) mm in (x, y, z) directions respectively.

Table 4.9: Modal Analysis Results

Mesh (mm)	**Natural Frequency (Hz)**
Fine (0.3 mm)	64.946
Medium (0.4 mm)	65.056
Coarse (0.5 mm)	65.212

The results of O'Hara are used as a verification case since the wing model is based on his morphological study of the hawkmoth wing [53]. O'Hara found the first natural frequency of the hawkmoth wing experimentally as 65 Hz., and 65.2 Hz.

numerically [86]. Mode shape comparison of results for both studies is presented in figure 4.14.

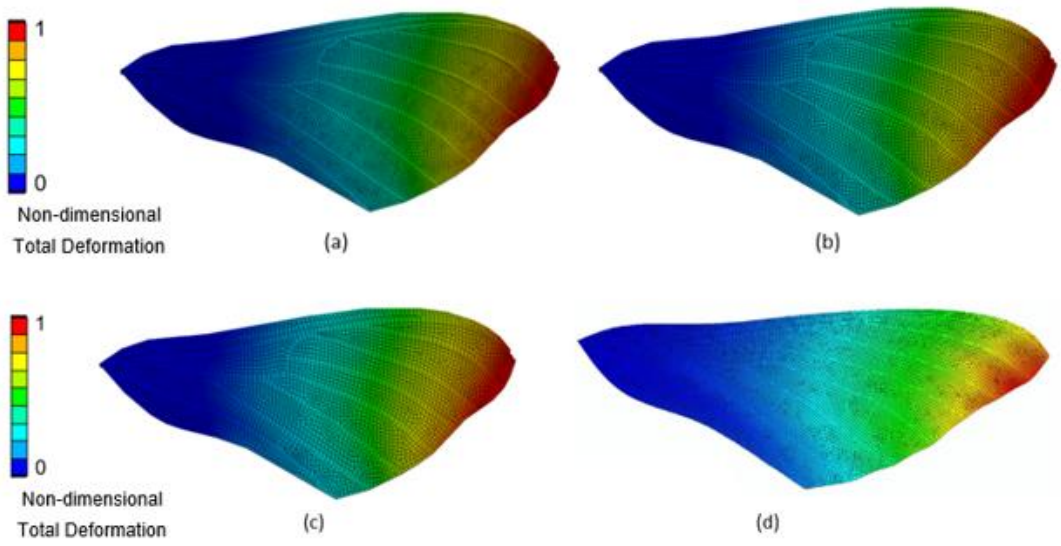

Figure 4.14: Mode Shape Comparison of Element Size (a) 0.3 mm (b) 0.4 mm (c) 0.5 mm (d) O'Hara [88]

Color contours in figure 4.14 denote the non-dimensional total deformation of wings. Total deformation is non-dimensionalized with respect to the maximum deflection at the wingtip. Minimum deflection occurs at the wing root and gradually increases in the spanwise direction towards the wingtip where maximum deflection is observed as expected. Mode shapes and displacement contours of all four models are in good agreement with each other. The natural frequency of medium-sized mesh with 0.4 mm element size is in good agreement with the experimental result of 65 Hz. and within an acceptable margin to the numerical result of 65.2 Hz. Although coarse mesh with 0.5 mm element size is almost identical to the numerical result, it is concluded that medium-sized mesh's result is closer to the experimental result, which implies that the model represents an actual hawkmoth wing more accurately.

Constructed models' wing properties are compared with the wing model of O'Hara's, to further check the accuracy of the model, and shown in table 4.9. It is seen that the masses and second area moments of inertia of the two models are in good agreement. The differences are negligible since values are infinitesimal and

cannot possess a significant influence on the results. Centroids of the models are different because of their orientation. Thus, considering modal analysis results, mode shapes, and wing properties the wing model with the medium-sized mesh (0.4 mm element size) is proved to be reasonably accurate with the existing literature model. Also table 4.10. is useful for seeing the effect of element size on number of elements and nodes of the mesh.

Table 4.10: Properties of Wing Models

Element Size	**0.3 mm**	**0.4 mm**	**0.5 mm**	**O'Hara [88]**
Mass (kg)	2.74e-05	2.74e-05	2.74e-05	2.86e-05
I_{xx} (kg.m^2)	1.28e-10	1.28e-10	1.28e-10	2.99e-10
I_{yy} (kg.m^2)	7.92e-10	7.92e-10	7.92e-10	1.14e-08
I_{zz} (kg.m^2)	6.64e-10	6.64e-10	6.64e-10	1.16e-08
Centroid (X, Y, Z mm)	(26.98, -4.5e-2, 2.9)	(26.98, -4.5e-2, 2.9)	(26.98, -4.5e-2, 2.9)	(22.1, 4, 0)
Nodes	10251	5986	3407	-
Elements	10100	5879	3333	-

Constructed wing model is also compared with the results of Sims as well. Hawkmoth wing's modal identification is carried out experimentally both in air and vacuum. The first natural frequency of the hawkmoth wing is measured as 59 Hz. in air and 80 Hz. in a vacuum. It is stated that the difference is caused by air acting as a damping mechanism [52].

After experimentally measuring the natural frequencies of hawkmoth wing in air and vacuum, numerical methods are explored by Sims. Finite element analysis is done on the wing model and effects of camber and venation are investigated separately.

First camber effects are explored and finite element analysis yielded 22 Hz. for a flat wing's first natural frequency and 159 Hz. for a cambered wing. The flat wing model has a first natural frequency of 41 Hz. with effects of venation considered [52].

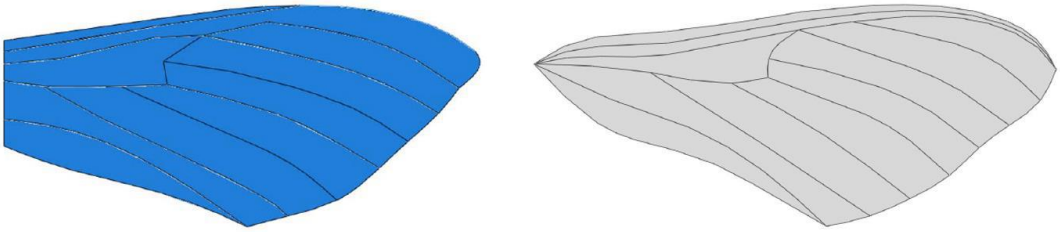

Figure 4.15: (a) Wing Model of Sims [52] Wing Model of O'Hara [53]

In figure 4.15, two different wing models are shown. In figure 4.15a, the wing has a root chord, instead of a single point such as in figure 4.15b. This is because when experimentally measuring the natural frequencies of the wing, Sims clamped the wing slightly further away from the wing root. The finite element model is constructed accordingly as well.

There are a few more differences between the models such as thickness, camber, and material properties. The thickness used by figure Sims is 0.12 mm whereas, the thickness used by O'Hara is 0.005 mm. Model of Sims has a constant camber with a concave down shape throughout the wing and the camber line starts from the middle of the root chord. As stated before the model of O'Hara has a variable camber starting from concave down at wing's origin point to concave up shape at wingtip.

Finally, Sims used 2300 kg/m^3 for density of both membrane and veins with Young's modulus of 1.90 and 3.70 GPa respectively. Both veins and membrane have Poisson's ratio of 0.495. On the other hand, O'Hara used different values for material properties, which can be seen in table 4.8. Considering all differences between models, it is expected that there is a difference between experimental measurements and numerical calculations.

4.2.4 Vein Diameter Ratio Effects

The effect of different inner vein diameter to outer vein diameter ratios is examined as well by performing two additional modal analyses with two new models with inner vein diameters of 60% and 80% of outer vein diameters, changing the initial

value from 70%. However, original vein sections and camber from figure 4.10 are preserved. Both of new models use medium-sized mesh with 0.4 mm element size since it proved to be the most accurate one. Numerical results and mode shapes are shown in table 4.11 and figure 4.16 respectively.

From table 4.11 it is seen that there is a negligible difference between the first natural frequencies (first bending mode) for different vein diameter ratios. However, an increase from 65 to 70 Hz. is observed, making the new models inaccurate and indicates that the 70% ratio must be preserved. The mass difference between models can be attributed to heavier veins of the model with a 60% ratio since as vein diameter ratio decreases, walls of wing veins get thicker.

Table 4.11: Vein Diameter Ratio Effects on First Natural Frequency

Vein Diameter Ratio	**60%**	**80%**
First Natural Frequency (Hz)	70.804	70.828
Mass (kg)	3.82e-05	2.40e-05

Figure 4.16 shows that mode shapes of the wing models with different inner to outer vein diameter ratios are accurate when compared with the original wing model's mode shape from figure 4.14. Locations for maximum and minimum displacement are the same and no significant change to contour bands are observed. Consequently making the results of different vein ratios results are computed correctly.

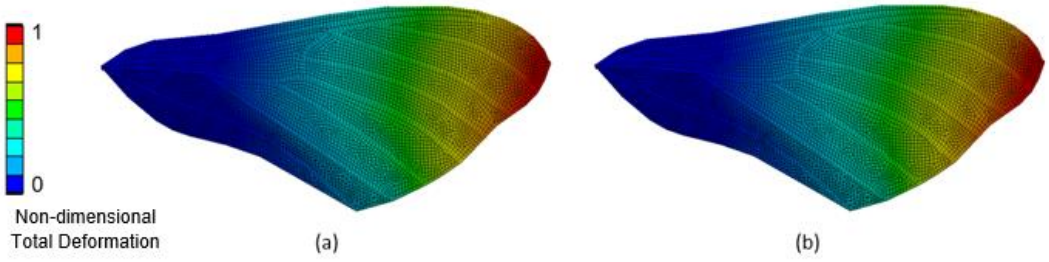

Figure 4.16: Mode Shapes of Different Vein Diameter Ratios (a) 60% (b) 80%

4.2.5 Material Study

The previously constructed wing model is modified for observing its first bending mode when its material is changed. The organic materials defined previously by O'Hara's morphological study [53], and newly chosen composite materials are given in table 4.12.

Table 4.12: Properties of Wing Materials

Material	**Organic**		**Composite**	
	Vein	**Membrane**	**Carbon Fiber**	**Mylar**
Density (kg/m^3)	2452	1400	1600	1250
Young's Modulus (GPa)	7.41	2.4	70	7
Poisson's Ratio	0.3	0.3	0.1	0.25

Values for carbon fiber are taken from Truong et al. [89] and values for mylar are taken from Singh & Chopra [90]. Three different models are used. The first model is flat (no camber) and has no veins. The second model is cambered but without veins. The third and final model is cambered and has veins. Mylar is only used in the third model as membrane material whereas the other two models are entirely made from carbon fiber since they have no veins. The third model's veins are carbon fiber as well.

Element size of 0.4 mm is used again for modal analysis for all three models. The first natural frequency (bending mode) of the flat carbon fiber wing without veins is found as 0.995 Hz. The natural frequency of the second model with camber but no veins is found as 1.345 Hz. Modal analysis of the third model with both camber and veins yielded 227.21 Hz. as the first natural frequency. The large difference between the second and third model's natural frequencies is mainly caused by carbon fiber

veins, adding tremendous structural strength because of carbon fiber's high Young's modulus of 70 GPa. From these results, it can be deduced that camber has a rather small impact on the natural frequency and the main cause of stiffness in the wings comes from venation.

The mode shapes of the three wing models with different materials are in figure 4.17. Similar to the study of vein diameter ratio, mode shapes are in good agreement with both figure 4.14 and 4.16. Camber used in the second and third model is the same with the varying camber from concave down to concave up shape with maximum distances of 1 mm running through the origin point of the wing to wingtip in the original model. Vein sections and diameters are also taken from the initially constructed wing model as well as the thickness of the membrane.

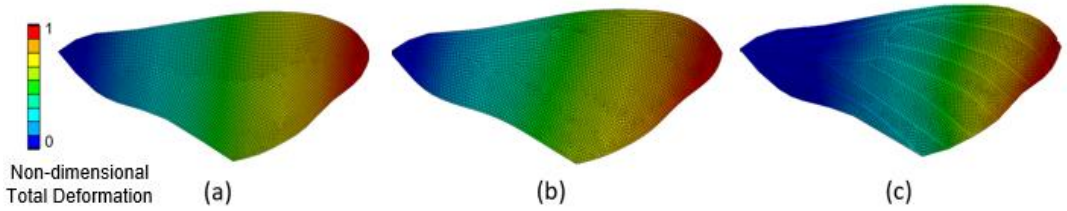

Figure 4.17: Mode Shape Results of Carbon Fiber Wings (a) without Camber and without Veins (b) with Camber and without Veins (c) with Camber and with Veins

CHAPTER 5

FLEXIBLE MULTIBODY DYNAMICS

After the mechanism is designed and initial simulations are carried out and the wing model is constructed and verified, the next step is combining two elements. In this chapter, constructed main wing model is imported from ANSYS/Mechanical software, where the modal analyses are carried out, into the ADAMS software as a flexible part.

A flexible wing part is imported from ANSYS to ADAMS. The flexibility of the wing is determined by previously determined material properties. The imported flexible wing is then coupled with the coupler link (link 3) of the mechanism for simulations. Again, similar to chapter 3, simulations are run in vacuum conditions. Consequently, aerodynamic effects are neglected, and obtained results are purely inertial.

Initially, it is verified again that the wing moves as the desired figure of eight shape by running simulations similar to simulations in chapter 3. After confirming the desired flapping trajectory is followed by the wingtip when the wing is connected to the coupler, different wing attachment points are determined on the coupler link for attaching the wing.

The aim of attaching the wing to different points on the coupler link is to find out the benefits of distinct points. The effects of these distinct points are examined using main wing model. Three points are determined on the coupler link, which are located at the front, middle, and rear of the link. Similar to simulations in chapter 3, duration is 1 second and angle of the crank is 90^{o}. However, rotation of the crank is in the opposite direction which is counter clockwise.

5.1 Importing Flexible Wing Models

ANSYS/Mechanical uses its own programming language named ANSYS Parametric Design Language (APDL). There is a built-in feature in ANSYS/Mechanical for importing the parts into ADAMS. This feature includes a pre-defined macro code written in APDL, named adams.mac, that can be implemented into solver commands by the user if desired.

Wing model is imported to ADAMS by using adams.mac and a method called batch mode. In batch mode, two remote points on the model are defined by the user. Next, in solver commands these two remote points are defined as endpoints and implemented along with adams.mac for creating a modal neutral file of the part, bounded by the defined remote points, titled file.mnf., modal neutral files (MNF) are used by ADAMS to create flexible bodies.

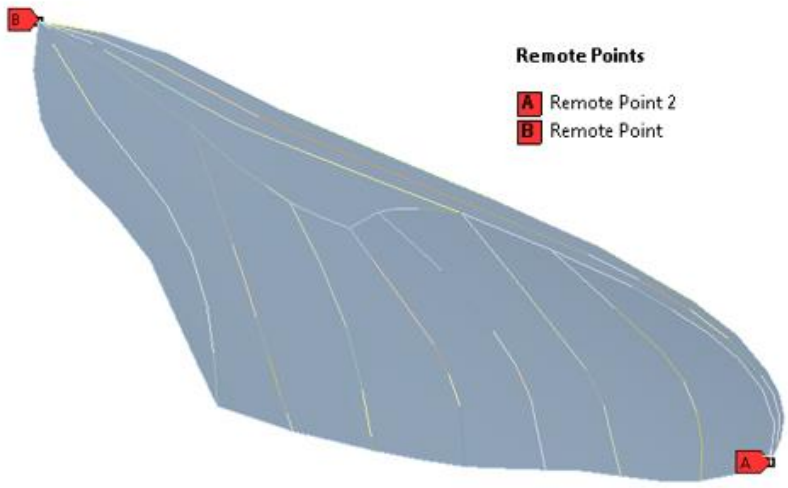

Figure 5.1: Remote Points on the Wing Model

In figure 5.1, two defined remote points bookending the main wing model are shown. The remote point at the wing root is named Remote Point and labeled as B, whereas the remote point at the wingtip is named Remote Point 2 and labeled as A. The flexible part is created between these points by the ANSYS for importing to ADAMS.

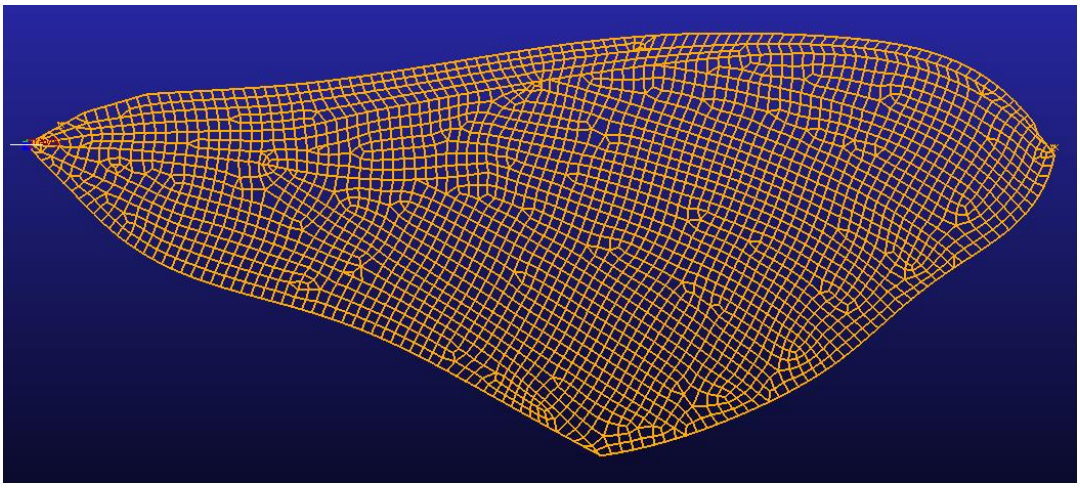

Figure 5.2: Flexible Wing Model in ADAMS

In figure 5.2, the imported flexible part of the main wing model is shown. ADAMS uses its own mesh-like grid (called wireframe) for .mnf files based on the actual mesh done by ANSYS. The flexible part in ADAMS has 4112 nodes within its mesh whereas in ANSYS the wing model has 5986 nodes given in table 4.10 for the main wing model with 0.4 mm element size.

5.2 Main Wing Model Simulations

After the main wing model is imported to ADAMS from ANSYS/Mechanical, it is coupled with the designed mechanism. Three different wing attachment points are chosen on the coupler link. These points are located at the front, middle, and rear of the link. At each point, a different figure of eight shape is drawn by the wing while flapping. Wing attachment points and their corresponding figure of eight shapes are given in figure 5.3.

The mechanism is driven from the short link at the front (-x direction). The wing is placed at the locations denoted by red, blue, and green dots with its tip facing the +z direction. Figure 5.3b shows how the figure of the eight shape is changed according to the wing placement on the mechanism. When the wing is placed at the red dot, the figure of eight's front loop is smaller than the rear. When the wing is placed at the green dot, figure of eight's rear loop is smaller than the front. Finally, if the wing is

placed at the blue dot (middle point of the long link as well as its center of mass) both sides of the figure of eight shape are equal. This enables collecting data from multiple points and optimizing the wing placement accordingly. The long link (coupler) rotates around its middle point while short links of the mechanism are rotating in opposite directions thus performing a passive pitching motion. At the same time, the tip of the wing is drawing an 8 shape corresponding to its place on the long link.

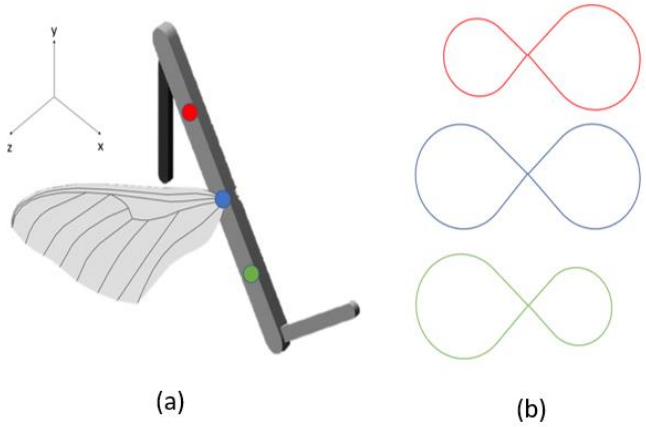

Figure 5.3: (a) Wing Attachment Points (b) Corresponding Figure of Eight Shapes

Three markers are placed on the flexible wing model to act as probes for data collecting. Marker locations are at wingtip, wing root and center of mass which can be seen in figure 5.4 below. Data is collected from three locations and three markers.

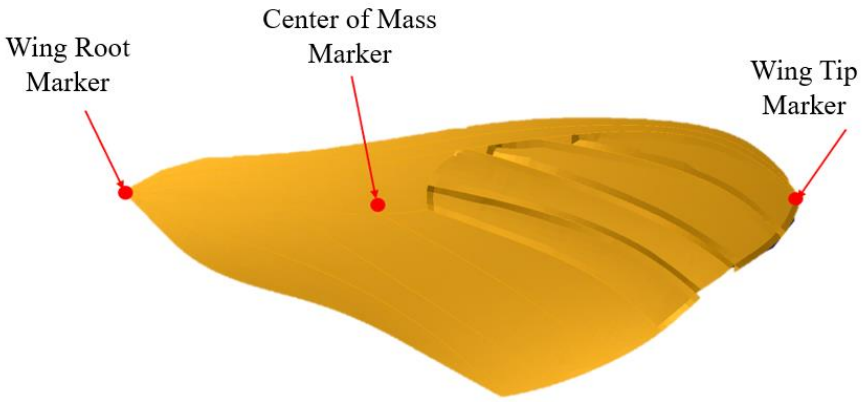

Figure 5.4: Marker Locations on the Shaded View of the Wing

5.2.1 Displacement and Angular Velocity Results

Simulations are performed at center of mass, wing root and, wing tip for all three wing attachment locations. Displacements in the x-direction and y-directions are obtained as well as the angular velocity around the z-axis. Durations of the simulations are 12 seconds which correspond to two flapping cycles of the mechanism. One flapping cycle of 6 seconds is very slow when compared to real hawkmoth flapping, which flaps around 24-26 times in one second. However, these simulations are for verification of the wing trajectories thus frequency is irrelevant at this point. Additionally, the simulations are done in vacuum conditions again, so every result is purely inertial, and aerodynamic effects are absent.

For all simulations, flapping motion starts from the middle point of the lemniscate shape as depicted in figure 5.5. Figure 5.5a shows the flapping trajectories from figure 5.3 and flapping motion start locations and directions are indicated by black dots and black arrows whereas figure 5.5b shows the wing attachment points on the mechanism corresponding to the flapping trajectory.

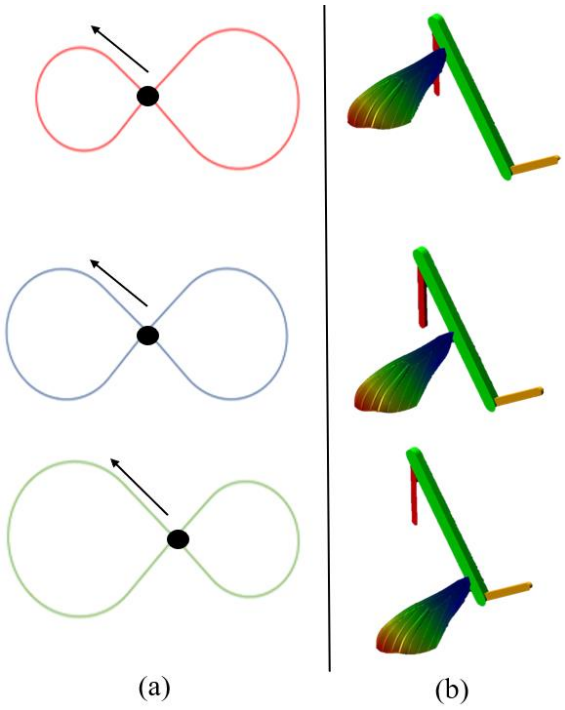

Figure 5.5: (a) Flapping Trajecetory and Direction (b) Wing Placement

Initially, wing root values are obtained. Figure 5.6a depicts that the long link of the mechanism, which the wing is attached, is performing plunging motion by showing translational displacement in the x-direction (red line) and in the y-direction (dashed blue line). Figure 5.6b depicts that there is an angular velocity around the z-axis. This shows while the mechanism is in motion, long link rotates around its center of mass (middle point) which means the wing is pitching. Wing root is attached to middle (blue point in figure 5.3) in this case.

Dividing the flapping motion into four equal parts, maximum displacement of approximately 55 mm for the positive x direction occurs at just before the 5 second mark, at the end of third quarter of the motion when the mechanism is horizontal. On the other hand, maximum displacement in the negative x-direction occur after approximately 2 seconds is elapsed and has a value of 20 mm, considering the wing moves from an initial position of 20 mm towards the origin point (located at the base of the crank link) it is decreasing as the graph shows. Displacements for y-direction is considerably smaller and it varies between 5 and -10 mm during flapping cycle starting with an initial position of 5 mm and dipping to a minimum of -10 mm when x-axis displacement is maximum.

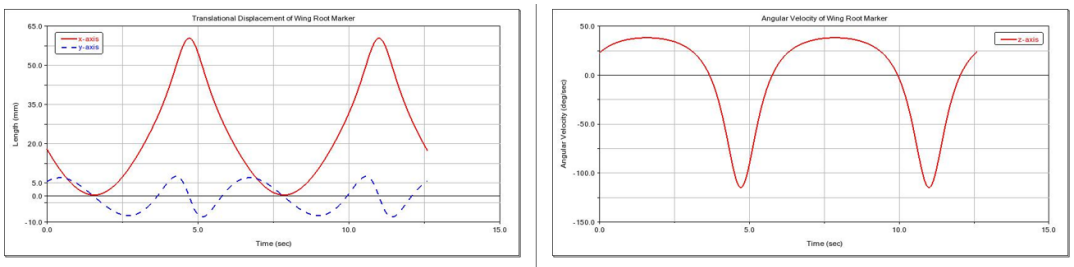

(a) (b)

Figure 5.6: (a) Displacement of the Wing Root in x-axis (red line) and y-axis (dashed blue line) (b) Angular Velocity of the Wing Root Around z-axis when the Wing is Attached to Middle (Blue) Point

In Figure 5.7a, translational displacement in the x and y directions are shown with red and dashed blue lines again respectively. In Figure 5.7b, angular velocity around the z-axis is shown. However, in figure 5.7 the wing is attached to the mechanism at the front (red point shown in figure 5.3a) instead of the middle point (blue point

shown in figure 5.6). It is seen that the displacement in the y-direction is increased at the front point when compared to the middle point while the angular velocity remains unchanged between two points with maximum value of 45 deg/s for first and fourth quarters of flapping motion, whereas it has minimum values of 110 deg/s for second and third quarters for both cases. This indicates that plunging motion is stronger at the red point than at the middle point. However, displacement in the x-direction is smaller as expected since the distance is shortened between the wing root and front point of the link. Maximum displacement location is 40 mm and minimum is -20 mm considering an initial position of 5 mm. As surging motion gets weaker, plunging gets stronger. Displacement of y-direction varies between 20 and -22 mm with an initial position of 20 mm, indicating maximum displacement point is the initial position.

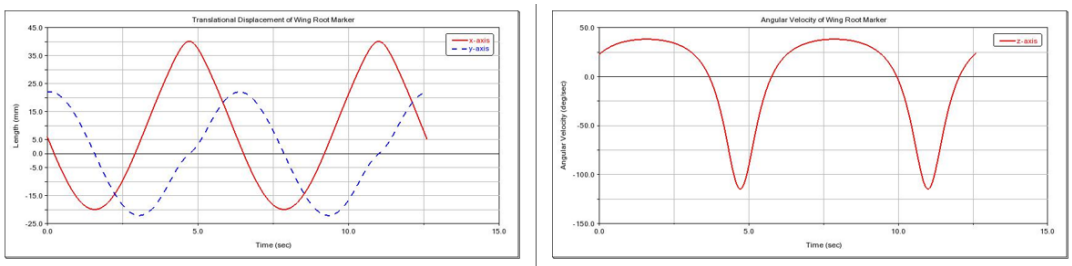

(a) (b)

Figure 5.7: (a) Displacement of the Wing Root in x-axis (red line) and y-axis (dashed blue line) (b) Angular Velocity of the Wing Root Around z-axis when the Wing is Attached to Front (Red) Point

Similarly, figure 5.8 shows the translational displacement in the x-axis and y-axis as well as angular velocity around the z-axis. Again, the angular velocity is the same as the other two points. Displacement in the y-direction remains same with when the wing is attached to the front, resulting in a change in only initial positions. Angular velocity around z-axis remains unchanged when compared with previous two cases. Considering x-direction displacement, initial position is 25 mm and maximum value is 75 mm, thus resulting in a change of 50 mm for rear wing attachment. Comparing with front wing attachment's maximum displacement of 60 mm, it is smaller.

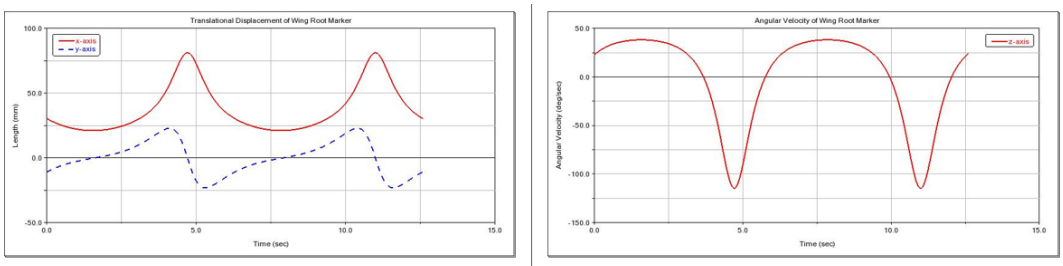

(a) (b)

Figure 5.8: (a) Displacement of the Wing Root in x-axis (red line) and y-axis (dashed blue line) (b) Angular Velocity of the Wing Root Around z-axis when the Wing is Attached to Rear (Green) Point

After obtaining and evaluating values from the wing root, values from center of mass of the wing is obtained and plotted with the same order of wing placement of middle, front and rear.

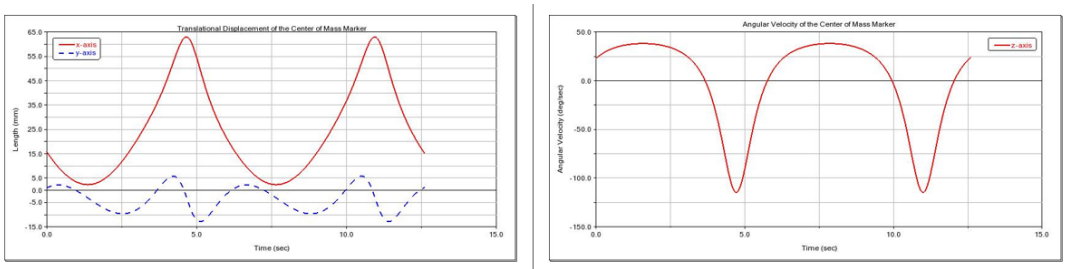

(a) (b)

Figure 5.9: (a) Displacement of the Center of Mass of the Wing in x-axis (red line) and y-axis (dashed blue line) (b) Angular Velocity of the Center of Mass of the Wing Around z-axis when the Wing is Attached to Middle (Blue) Point

As expected, x and y-direction displacement of the center of mass of the wing are very similar to the wing root when the wing is attached to the middle of the flapping mechanism. Only initial positions are different in both cases. Center of mass has initial points for x and y-directions as 15 and 0 mm respectively shown in figure 5.9a. On the other hand, wing root has initial points of 20 and 5 mm for initial points for x and y-directions respectively as well. Figure 5.9b shows that the angular velocity remains unchanged.

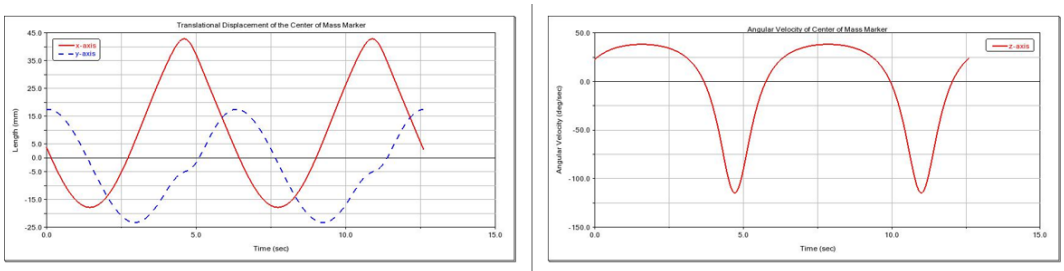

(a) (b)

Figure 5.10: (a) Displacement of the Center of Mass of the Wing in x-axis (red line) and y-axis (dashed blue line) (b) Angular Velocity of the Center of Mass of the Wing Around z-axis when the Wing is Attached to Front (Red) Point

Figure 5.10 depicts the displacements and angular velocity of the center of mass of the wing when it is placed at the front of the mechanism. Again, only initial positions of displacement values are different which is caused by the distance between the wing root and center of mass of the wing. In this case, initial positions for x and y-directions before flapping motion starts is 5 mm and 20 mm respectively.

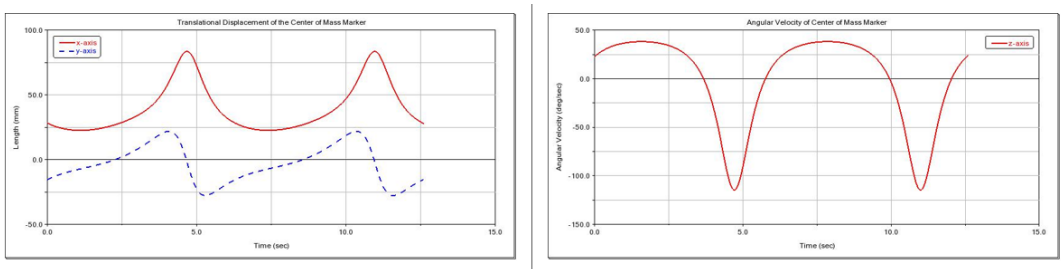

(a) (b)

Figure 5.11: (a) Displacement of the Center of Mass of the Wing in x-axis (red line) and y-axis (dashed blue line) (b) Angular Velocity of the Center of Mass of the Wing Around z-axis when the Wing is Attached to Rear (Green) Point

The displacements and angular velocity, which are shown in figure 5.11 closesly resemble the results from figure 5.8. However, there are minor differences for center of mass of the wing when it is attached to the rear of the flapping mechanism such as, a higher minimum x-displacement value and red line seems to shift towards left hand side, making a tighter curve and indicating a faster response of the center of mass than the wing root. It can be concluded that flexibility effects play a part and

cause the location of center of mass of the wing to flex more than wing root when flapping.

Finally, results from wing tip are collected and evaluted for each of the three designated wing attachment locations. In figure 5.12, displacements and angular velocity graphs are shown. Closely inspecting figure 5.12a, effects of flexibility is becoming more dominant when compared with the center of mass and wing root results. Maximum x-direction displacement of the wing tip is 60 mm (between 10 and 70 mm), more than two other cases. This is an expected result since maximum deflection occurs at the wing tip as shown in modal analysis results from previous chapter. Also, by looking at the vertical axis of displacement graph, wing tip has a higher minimum x-displacement value than mass center. Additionally, the displacement increase of wing tip is slower than other two points.

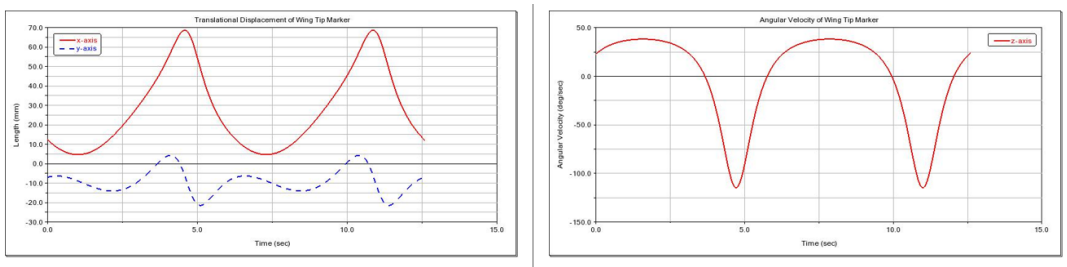

(a) (b)

Figure 5.12: (a) Displacement of the Wing Tip in x-axis (red line) and y-axis (dashed blue line) (b) Angular Velocity of the Wing Tip Around z-axis when the Wing is Attached to Middle (Blue) Point

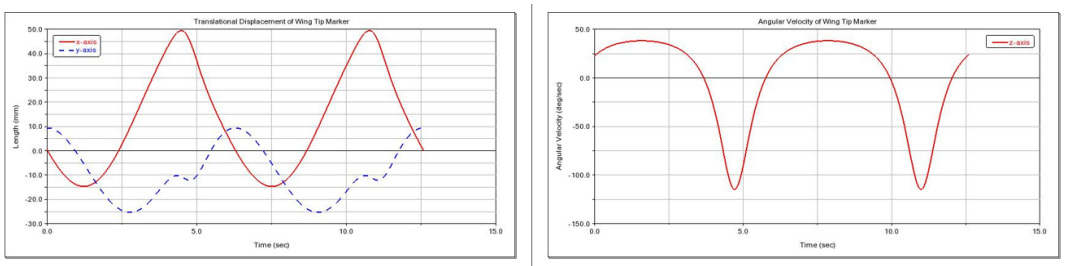

(a) (b)

Figure 5.13: (a) Displacement of the Wing Tip in x-axis (red line) and y-axis (dashed blue line) (b) Angular Velocity of the Wing Tip Around z-axis when the Wing is Attached to Front (Red) Point

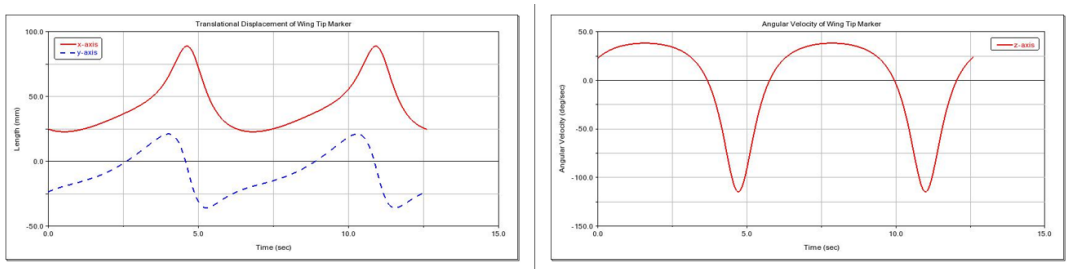

(a) (b)

Figure 5.14: (a) Displacement of the Wing Tip in x-axis (red line) and y-axis (dashed blue line) (b) Angular Velocity of the Wing Tip Around z-axis when the Wing is Attached to Rear (Green) Point

In figure 5.13a, x-displacement of wing tip is 5mm higher than center of mass' x-displacement when placed at the front of the mechanism, denoted in figure 5.10a. Additionally, x-displacement curve is again slightly distorted, meaning a slower increase as a reulst of flexiblity effects. However, by looking at results when the wing is attached to the rear, wing tip has no significantly different results from other cases. Finally, angular velocity around z-axis yields the same graph for all nine cases, indicating the passive pitching of the wing is present and constant at all times.

5.2.2 Force Results

Force is measured in both x and y directions, from one node located at the wing root when the wing is attached to three designated points on the mechanism for further evaluation.

First, results are obtained from wing root when the wing is attached to the middle point (blue point in figure 5.3) of the coupler link. Simulation is run for 1 second again with a corresponding flapping frequency of 1 Hz. for determining the maximum and minimum forces. Results are shown in figure 5.15 below. Continuous red line depicts the force in the x-direction and dashed blue line represents the force in the y-direction. Negative sign in front of the force values indicate direction according to the coordinate system given in figure 5.3 with the origin being the base of the crank link.

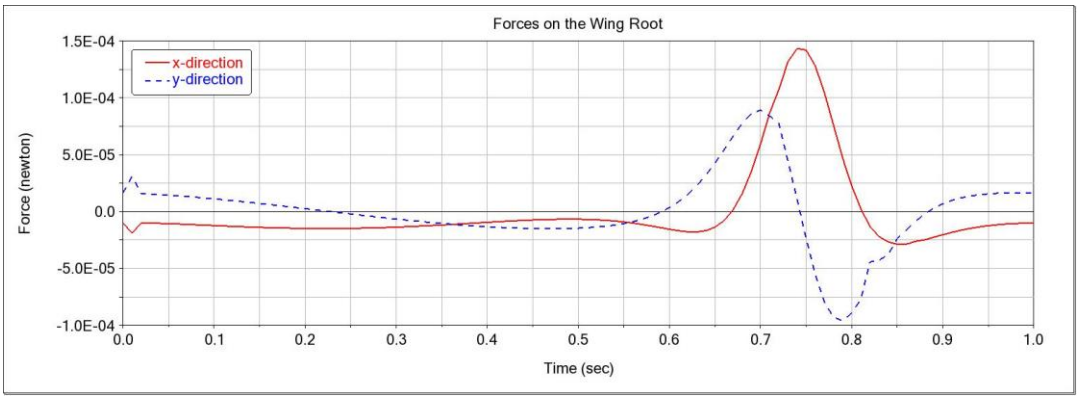

Figure 5.15: Forces on the Wing Root When the Wing is Attached to the Middle Point

Maximum forces are 0.00015 and 0.0001 Newtons for x and y-directions respectively with a negative coutnerpart in the y-direction indicating stroke reversal occuring at 0.75 seconds rather than after 1 second is elapsed. This is caused by the initial position of the wing shown in figure 5.5.

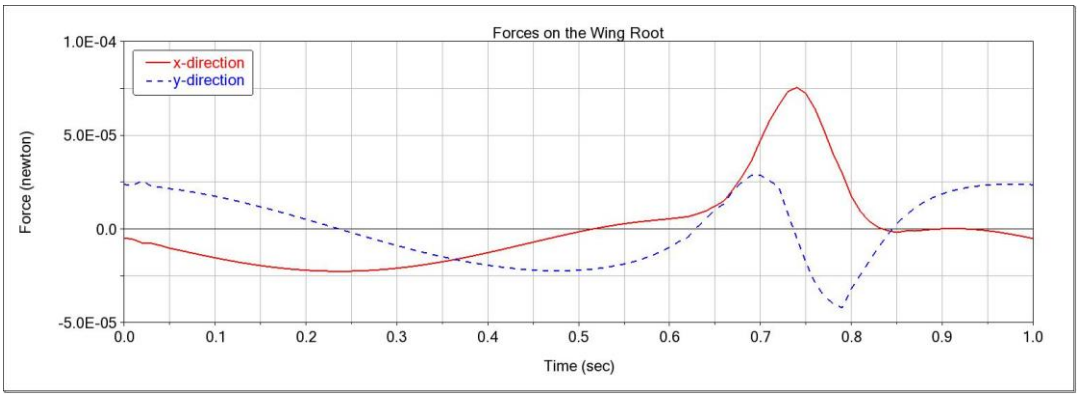

Figure 5.16: Forces on the Wing Root When the Wing is Attached to the Front Point

In figure 5.16, force measurements of the wing root is obtained when the wing is connected to the red point (middle) of the coupler link. Maximum forces are much smaller when compared with the middle point for both directions. Also, by observing the y-direction plot around when the stroke reversal occurs, it is seen that maximum and minimum values are different from each other. Consequently, this indicates that stroke reversal happens differently than the middle point's stroke reversal.

Finally, force measurements obtained from the rear (green point) of the coupler link is presented in figure 5.17. Forces in both directions are both greatest for all three cases with values of 0.0002 and 0.0015 Newtons in x and y-directions respectively. Meaning that both surging and plunging motions are stronger in this location. This result is in good agreement with displacement and angular velocity graphs as well. It is seen that a stroke reversal similar to the middle point occurs around 0.75 seconds.

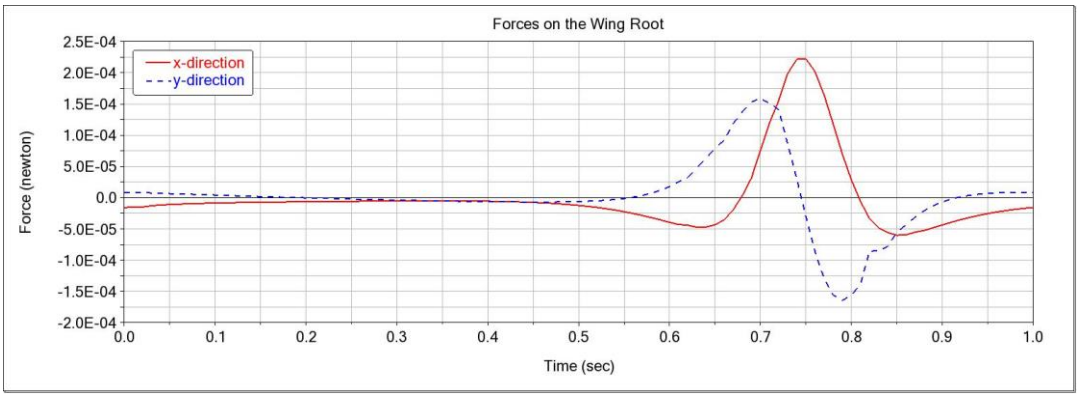

Figure 5.17: Forces on the Wing Root When the Wing is Attached to the Rear Point

Finally, for all three cases it is seen that greatest forces are generated around the stroke reversal period in both directions. Force measurements are done for only one node out of possible 4000 other nodes of the flexible wing model while only inertial forces are taken into consideration and aerodynamic forces are neglected, small values are considered normal. Consequently, results show that a considerable portion of required total force to lift a 1.5 gram hawkmoth can be gathered with the inertial forces generated by the designed flapping mechanism.

5.2.3 Torque Results

As a next step, torque measurements are obtained from the wing root for three wing attachment points. Similar to force measurement, torque values for x and y-directions are obtained from a single node.

First torque measurement is done at the middle point on the coupler link of the mechanism and duration of the simulation is 1 second. Torque measurement results are presented in the below figure 5.18. Continuous red line is the torque in x-direction and dashed blue line is torque in y-direction. In both directions, torques have approximately the same maximum value of 0.002 Nm. Fluctuation in the values near 0.75 indicate stroke reversal phase.

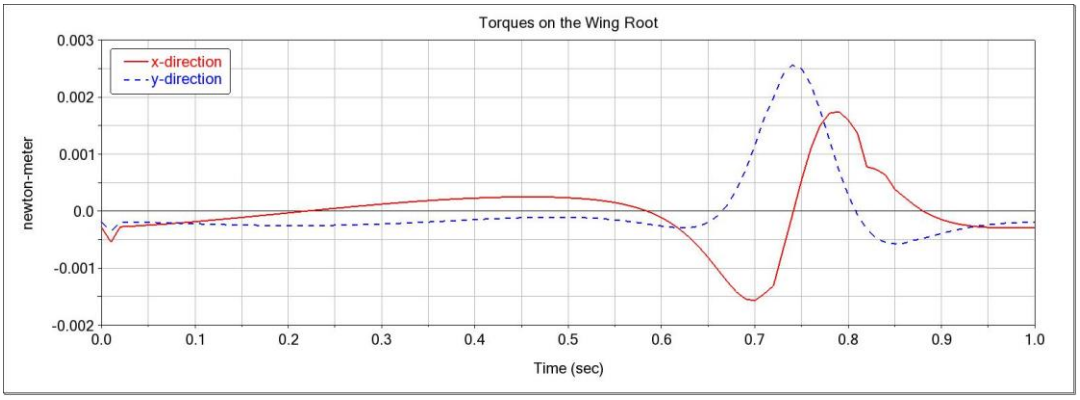

Figure 5.18: Torques on the Wing Root When the Wing is Attached to the Midde Point

In figure 5.19 below, torque measurements in x and y-directions taken from the wing root when the wing is attached to the front of the coupler link of the flapping mechanism is presented. Again, continuous red line depicts x-direction and dashed blue line denotes y-direction.

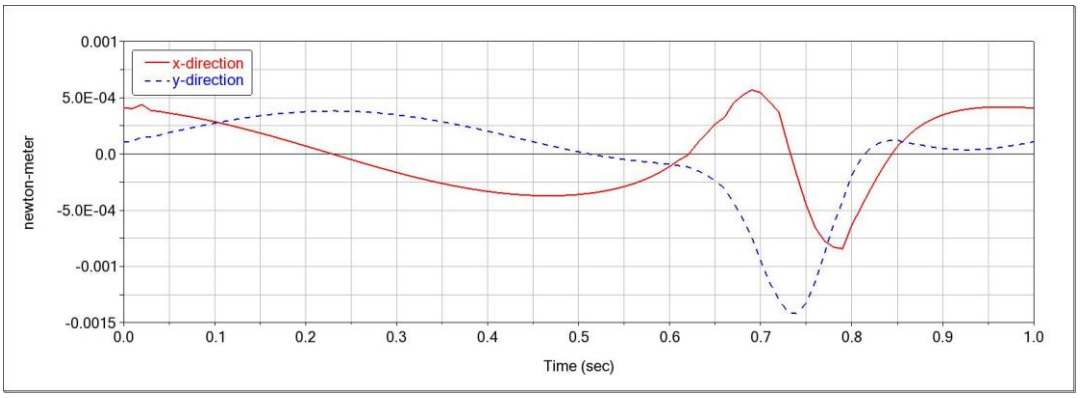

Figure 5.19: Torques on the Wing Root When the Wing is Attached to the Front Point

Since the mechanism is driven from the crank link, when the wing is attached to the front of the coupler link, it gets closer to the origin point of the mechanism. Cosnequently, length between wing attachment point and mechanism's driving point gets shorter which results in reduced torque values compared to the middle point.

Finally in figure 5.20, torque values obtained from the rear attachment point is presented. When the wing is attached to the rear point of the mechanism, the length of the load arm is longest. As expected highest torque values are obtained from rear point which can be seen in below figure.

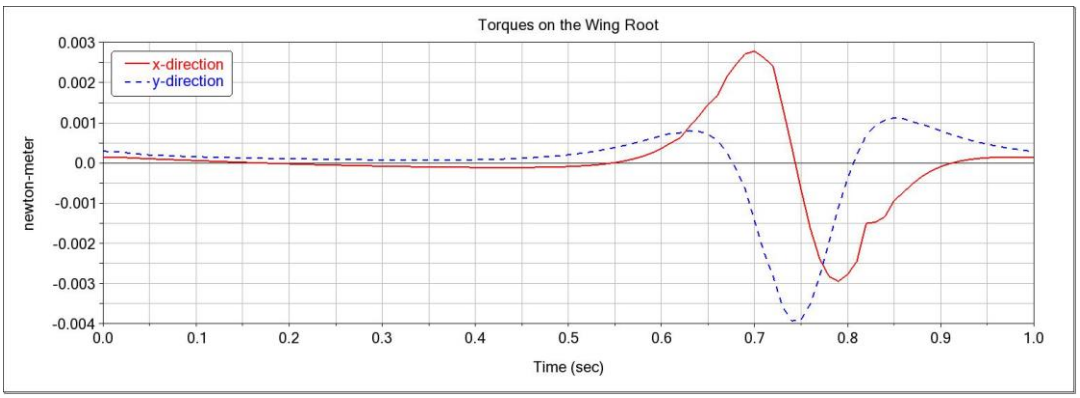

Figure 5.20: Torques on the Wing Root When the Wing is Attached to the Rear Point

Maximum torque at the middle point is 0.002 Nm whereas, at the rear maximum torque value is 0.004 Nm. Notice that the torque in y-direction has a negative sign which shows that it is occurring in the opposite direction during stroke reversal.

Force and torque measurements are crucial for choosing an appropriate motor for driving the mechanism which affects the overall performance of the whole FWMAV as a result.

CHAPTER 6

DISCUSSION AND CONCLUSION

The main aim of this study is to design and simulate a flapping wing mechanism that can perform complex flapping motions done by insects despite being rather simple. The wing of the hawkmoth (Manduca sexta) is chosen to be used since it has been studied thoroughly and there is vast knowledge about its morphological characteristics.

First, a brief literature survey is conducted about the flapping aerodynamics, biological properties of hawkmoth wing and, flapping-wing mechanisms. After that, the wing is modeled as a flexible finite element model. The accuracy of the constructed model is verified by performing modal analysis to find its natural frequency and compare it to the data present in the literature. Several different morphological properties of the wing are changed and modal analyses are done again to see the effects of modified parameters on the natural frequency response of the wing model. Constructed wing model can also be used for further simulations with different mechanisms.

After the wing model is verified, a planar, four-bar lemniscate mechanism is designed which can mimic the pitching and plunging of the wing by drawing a figure of eight shape with the wingtip. Three distinct locations are chosen on the long link and three simulations are run for the wing root, wing tip and center of mass of the wing model.

Obtained displacement, angular velocity, force and torque data from different locations are compared with each other, providing an insight into the optimum wing attachment location. The modularity of the mechanism is achieved through the availability of different wing placement locations along with the long link of the mechanism. Simulation results indicate promising results for a FWMAV application with the use of a wing with biologically accurate specifications.

REFERENCES

1. Ward, T. A., Fearday, C. J., Salami, E., & Binti Soin, N. (2017). "A Bibliometric Review of Progress in Micro Air Vehicle Research." *International Journal of Micro Air Vehicles, 9*(2), 146-165. doi:10.1177/1756829316670671
2. S. R. Pappu, V., Steck, J., & Ramamurthi, G. (2016). "Turbulence Effects on Modified State Observer-Based Adaptive Control: Black Kite Micro Aerial Vehicle"
3. Duranti, S., Conte, G., Lundström, D., Rudol, P., Wzorek, M., & Doherty, P. (2007). "LINKMAV, a Prototype Rotary Wing Micro Aerial Vehicle." *IFAC Proceedings Volumes, 40(7), 473-478*. doi:10.3182/20070625-5-fr-2916.00081
4. Rosen, M. H., Le Pivain, G., Sahai, R., Jafferis, N. T., & Wood, R. J. (2016). "Development of a 3.2g Untethered Flapping-Wing Platform for Flight Energetics and Control Experiments." *2016 IEEE International Conference on Robotics and Automation (ICRA)*. doi:10.1109/icra.2016.7487492
5. Kurtuluş, D.F., (2011a). "Introduction to micro air vehicles: concepts, design, and applications, Recent Developments in Unmanned Aircraft Systems (UAS, including UAV and MAV)", Von Karman Institute for Fluid Dynamics, 187-217.
6. Tobias, A., "Experimental Methods to Characterize Nonlinear Vibration of Flapping Wing Micro Air Vehicles", Master's Thesis, Air Force Institute of Technology, 2005.
7. Keennon, M., Klingebiel, K., & Won, H. (2012). "Development of the Nano Hummingbird: A Tailless Flapping Wing Micro Air Vehicle." *50th AIAA Aerospace Sciences Meeting including the New Horizons Forum and Aerospace Exposition*. doi:10.2514/6.2012-588
8. Seshadri, P., Benedict, M., & Chopra, I. (2009). "Understanding Insect-Based Flapping Flight from a Micro Air Vehicle Perspective." *Proceedings*

of the American Helicopter Society International Specialists' Meeting on Unmanned Rotorcraft. Scottsdale, AZ.

9. Helbling, E. F., Fuller, S. B., & Wood, R. J. (2017). "Altitude Estimation and Control of an Insect Scale Robot with an Onboard Proximity Sensor." *Springer Proceedings in Advanced Robotics, 57-69*. doi:10.1007/978-3-319-51532-8_4
10. Zhang, J., Tu, Z., Fei, F., & Deng, X. (2017). "Geometric Flight Control of a Hovering Robotic Hummingbird." *2017 IEEE International Conference on Robotics and Automation (ICRA)*. doi:10.1109/icra.2017.7989638
11. Sane, S. P. (2003). "The Aerodynamics of Insect Flight*." Journal of Experimental Biology, 206(23), 4191–4208.* doi:10.1242/jeb.00663
12. Frank, S. (2011). "Vortex Tilting and the Enhancement of Spanwise Flow in Flapping Wing Flight", *University of Central Florida,* Honors in the Major Thesis (HIM) 1990-2015, 1218.
13. Kurtulus, D. F. (2021). "Vortex flow aerodynamics behind a symmetric airfoil at low angles of attack and Reynolds Numbers", *International Journal of Micro Air Vehicles*, doi: 10.1177/17568293211055653
14. Kurtulus, D.F. (2019). "Unsteady Aerodynamics of a Pitching NACA 0012 Airfoil at Low Reynolds Number", *International Journal of Micro Air Vehicles, Vol 11, pp 1-21,* November 2019 doi:10.1177/1756829319890609
15. Kurtulus, D.F. (2018). "Aerodynamic loads of small amplitude pitching NACA 0012 airfoil at Reynolds Number of 1000", *AIAA Journal, Technical Note, Vol. 56, No. 8, pp. 3328-3331.*
16. Kurtulus, D.F. (2016). "On the wake pattern of symmetric airfoils for different incidence angles at Re=1000", *International Journal of Micro Air Vehicles, Vol 8, No:2, pp. 109-139.*
17. Kurtulus, D.F. (2015). "On the unsteady behavior of the flow around NACA 0012 airfoil with steady external conditions at Re=1000", *International Journal of Micro Air Vehicles, Vol 7, No 3, pp 301-326,* September 2015

18. Kurtulus, D.F. (2009). “Ability to forecast unsteady aerodynamic forces of flapping airfoils by Artificial Neural Network”, *Neural Computing & Applications, Vol. 18, Issue 4, pp.359-368.*
19. Kurtulus, D.F., David L., Farcy, A., Alemdaroglu, N. (2008) “Aerodynamic Characteristics of Flapping Motion in Hover”. *Experiments in Fluids, Vol. 44, pp. 23–36*
20. Ahmed, T., Kurtulus, D.F., (2021). “Unsteady Aerodynamics of Cambered Airfoils at Low Reynolds Number”. *11th Ankara International Aerospace Conference.*
21. T. Weis-Fogh, “Quick Estimates of Flight Fitness in Hovering Animals, Including Novel Mechanisms for Lift Production," *Journal of Experimental Biology*, vol. 59 no. 1, pp. 169-230, 1973.
22. Ellington, C. P. (1984). “The Aerodynamics of Hovering Insect Flight. I. the Quasi-Steady Analysis.” *Philosophical Transactions of the Royal Society of London Series. B, Biological Sciences, 305(1122*), 1-15. doi:10.1098/rstb.1984.0049
23. Ellington, C. P. (1984). “The Aerodynamics of Hovering Insect Flight. II. Morphological Parameters.” *Philosophical Transactions of the Royal Society of London Series. B, Biological Sciences, 305(1122),* 17-40. doi:10.1098/rstb.1984.0050
24. Ellington, C. P. (1984). “The Aerodynamics of Hovering Insect Flight. III. Kinematics.” *Philosophical Transactions of the Royal Society of London Series. B, Biological Sciences, 305(1122),* 41-78. doi:10.1098/rstb.1984.0051
25. Ellington, C. P. (1984). “The Aerodynamics of Hovering Insect Flight. IV. Aerodynamic Mechanisms.” *Philosophical Transactions of the Royal Society of London Series. B, Biological Sciences, 305(1122),* 79-113. doi:10.1098/rstb.1984.0052
26. Ellington, C. P. (1984). “The Aerodynamics of Hovering Insect Flight. V. A Vortex Theory.” *Philosophical Transactions of the Royal Society of London*

Series B, Biological Sciences, 305(1122), 115-144. doi:10.1098/rstb.1984.0053

27. Ellington, C. P. (1984). "The Aerodynamics of Hovering Insect Flight. VI. Lift and Power Requirements." *Philosophical Transactions of the Royal Society of London Series B, Biological Sciences, 305(1122),* 145-181. doi:10.1098/rstb.1984.0054
28. Dickinson, M. H. (1999). "Wing Rotation and the Aerodynamic Basis of Insect Flight." *Science, 284(5422),* 1954-1960. doi:10.1126/science.284.5422.1954
29. Shyy, W., Lian, Y., Tang, J., Liu, H., Trizila, P., Stanford, B., Lernal, B., Cesnik, C., Friedman, P., Ifju, P. (2008). "Computational Aerodynamics of Low Reynolds Number Plunging, Pitching and Flexible Wings for MAV Applications." *46th AIAA Aerospace Sciences Meeting and Exhibit*. doi:10.2514/6.2008-523
30. Mao, S., & Gang, D. (2003). "Lift and Power Requirements of Hovering Insect Flight." *Acta Mechanica Sinica, 19*(5), 458-469. doi:10.1007/bf02484580
31. Jane Wang, Z. (2000). "Two-Dimensional Mechanism for Insect Hovering". *Physical Review Letters, 85*(10), 2216-2219. doi:10.1103/physrevlett.85.2216
32. Doman, D., Oppenheimer, M., & Sigthorsson, D. (2009). "Dynamics and Control of a Minimally Actuated Biomimetic Vehicle: Part I - Aerodynamic Model." *AIAA Guidance, Navigation, and Control Conference*. doi:10.2514/6.2009-6160
33. Doman, D., Oppenheimer, M., & Sigthorsson, D. (2009). "Dynamics and Control of a Minimally Actuated Biomimetic Vehicle: Part II-Control." *AIAA Guidance, Navigation, and Control Conference*. doi:10.2514/6.2009-6161
34. Sun, M., Wang, J., & Xiong, Y. (2007). "Dynamic Flight Stability of Hovering Insects." *Acta Mechanica Sinica, 23*(3), 231-246. doi:10.1007/s10409-007-0068-3

35. Orlowski, C. T., & Girard, A. R. (2011). “Modeling and Simulation of Nonlinear Dynamics of Flapping Wing Micro Air Vehicles.” *AIAA Journal, 49*(5), 969-981. doi:10.2514/1.j050649
36. Nguyen, A. T., Le, V. D. T., Tran, T. H., Duc, V. N., & Phung, V. B. (2020). “Study of Vertically Ascending Flight of a Hawkmoth Model.” *Acta Mechanica Sinica*. doi:10.1007/s10409-020-00993-w
37. Lua, K. B., Lai, K. C., Lim, T. T., & Yeo, K. S. (2010). “On the Aerodynamic Characteristics of Hovering Rigid and Flexible Hawkmoth-like Wings.” *Experiments in Fluids*, 49(6), 1263–1291. doi:10.1007/s00348-010-0873-5
38. Chu, Y.-J., Liew, H.-L., & Ganesan, P. B. (2021). “Aerodynamics of a Wing Under Figure-of-Eight Flapping Motion: FSI Simulations”. *The Aeronautical Journal, 1–25*. doi:10.1017/aer.2021.35
39. Bhat, S. S., Zhao, J., Sheridan, J., Hourigan, K., & Thompson, M. C. (2019). “Effects of Flapping Motion Profiles on Insect Wing Aerodynamics.” *Journal of Fluid Mechanics*, 884. doi:10.1017/jfm.2019.929
40. Kang, C.-K., Aono, H., Cesnik, C. E. S., & Shyy, W. (2011). “Effects of Flexibility on the Aerodynamic Performance of Flapping Wings.” *Journal of Fluid Mechanics,* 689, 32–74. doi:10.1017/jfm.2011.428
41. Ellington, C. P. Willmott, A. P., & (1997). “The Mechanics of Flight in the Hawkmoth Manduca Sexta. I. Kinematics of Hovering and Forward Flight.” *Journal of Experimental Biology, 200*(21), 2705-2722. doi:10.1242/jeb.200.21.2705
42. Ellington, C. P. Willmott, A. P., & (1997). “The Mechanics of Flight in the Hawkmoth Manduca Sexta. II. Aerodynamic Consequences of Kinematic and Morphological Variation.” *Journal of Experimental Biology, 200 (21),* 2723-2745. doi:10.1242/jeb.200.21.2723
43. Kurtulus, D. F., David, L., Farcy, A., & Alemdaroglu, N. (2007). “Aerodynamic Characteristics of Flapping Motion in Hover.” *Experiments in Fluids, 44(1), 23–36.* doi:10.1007/s00348-007-0369-0

44. Hu, H., Tamai, M., & Murphy, J. T. (2008). “Flexible-Membrane Airfoils at Low Reynolds Numbers.” *Journal of Aircraft, 45(5), 1767–1778.* doi:10.2514/1.36438
45. Cleaver, D. J., Calderon, D. E., Wang, Z., & Gursul, I. (2016). “Lift Enhancement Through Flexibilitynal of Plunging Wings at Low Reynolds Numbers.” *Journal of Fluids and Structures, 64, 27–45.* doi: 10.1016/j.jfluidstructs.2016.04.004
46. Agrawal, A., & Agrawal, S. K. (2009). “Design of Bio-Inspired Flexible Wings for Flapping-Wing Micro-Sized Air Vehicle Applications.” *Advanced Robotics, 23(7-8), 979–1002.* doi:10.1163/156855309x443133
47. Ramamurti, R., & Sandberg, W. C. (2002). “A Three-Dimensional Computational Study of the Aerodynamic Mechanisms of Insect Flight.” *Journal of Experimental Biology, 205*(10), 1507-1518. doi:10.1242/jeb.205.10.1507
48. Bai, P., Cui, E., Li, F., Zhou, W., & Chen, B. (2007). “A New Bionic MAV’s Flapping Motion Based on Fruit Fly Hovering at Low Reynolds Number.” *Acta Mechanica Sinica, 23*(5), 485-493. doi:10.1007/s10409-007-0102-5
49. Yoon, S.-H., Cho, H., Lee, J., Kim, C., & Shin, S.-J. (2020). “Effects of Camber Angle on the Aerodynamic Performance of Flapping-Wing Micro Air Vehicle.” *Journal of Fluids and Structures*, 97, 103101. doi: 10.1016/j.jfluidstructs.2020103101
50. Reid, H., Zhou, H., Maxcer, M., Peterson, R. K., Deng, J., & Jankauski, M. (2021). “Toward the Design of Dynamically Similar Artificial Insect Wings.” *International Journal of Micro Air Vehicles*, 13, 175682932199213. doi:10.1177/1756829321992138
51. Shahzad, A., Tian, F.-B., Young, J., & Lai, J. C. S. (2018). “Effects of Hawkmoth-like Flexibility on the Aerodynamic Performance of Flapping Wings with Different Shapes and Aspect Ratios.” *Physics of Fluids,* 30 (9), 091902. doi:10.1063/1.5044635

52. Sims, T. W., Palazotto, A. N., & Norris, A. (2010). “A Structural Dynamic Analysis of a Manduca Sexta Forewing.” *International Journal of Micro Air Vehicles*, 2(3), 119–140. doi:10.1260/1756-8293.2.3.119
53. O’Hara, R. P., & Palazotto, A. N. (2012). “The Morphological Characterization of the Forewing of the Manduca Sexta Species for the Application of Biomimetic Flapping Wing Micro Air Vehicles.” *Bioinspiration & Biomimetics, 7(4), 046011.* doi:10.1088/1748-3182/7/4/046011
54. Nakata, T., & Liu, H. (2011). “Aerodynamic Performance of a Hovering Hawkmoth with Flexible Wings: A Computational Approach.” *Proceedings of the Royal Society B: Biological Sciences, 279(1729), 722–731.* doi:10.1098/rspb.2011.1023
55. Analooee, A., & Ghayour, M. (2020). “Flowchart-Aided Design of a Novel Spatial Flapping Wing Mechanism.” *Proceedings of the Institution of Mechanical Engineers, Part C: Journal of Mechanical Engineering Science,* 095440622092469. doi:10.1177/0954406220924695
56. Khan, Z. A., Agrawal, S. K., (2007). **“**Design and Optimization of a Biologically Inspired Flapping Mechanism for Flapping Wing Micro Air Vehicles”, *2007 IEEE International Conference on Robotics and Automation Roma, Italy, 10-14 April 2007*
57. Burgess, S. C., Alemzadeh K., Zhang, L., (2004). “The Development of a Miniature Mechanism for Producing Insect Wing Motion”, *Design and Nature II pp. 237-248*
58. Çalış, Ö., Arıkan, K. B., Kurtuluş, D. F., (2021). “Modeling the Flapping Motion via Quasi-Steady Approach and Controlling the Longitudinal Dynamics of a Flapping Wing MAV”, *11th Ankara International Aerospace Conference.*
59. Moses, K., Willis, M., & Quinn, R. (2020). “Biomimicry of the Hawk Moth, Manduca sexta (L.), Produces an Improved Flapping-Wing Mechanism.” *Biomimetics*, 5(2), 25. doi:10.3390/biomimetics5020025

60. Artobolevsky, I. I., & Weinstein, N. (1976). *Mechanisms in modern engineering design: A handbook for engineers, designers, and inventors.* Moscow: Mir Publ.
61. Rehmat, Z., Lee, J. S., Roll, J., Yim, W., Trabia, M., B., 2009. "Design of "Figure-8" Spherical Motion Flapping Wing for Miniature UAV", *Proceedings of the ASME 2009 International Design Engineering Technical Conferences & Computers and Information in Engineering Conference, August 30-September 2, 2009, San Diego, California, 2009*
62. Żbikowski, R., Knowles, K., Pedersen, C. B., & Galiński, C. (2004). "Some Aeromechanical Aspects of Insect-like Flapping Wings in Hover." *Proceedings of the Institution of Mechanical Engineers, Part G: Journal of Aerospace Engineering, 218*(6), 389-398. doi:10.1243/0954410042794948
63. Nguyen, Q. V., Chan, W. L., & Debiasi, M. (2014). "Design, Fabrication, and Performance Test of a Hovering-Based Flapping-Wing Micro Air Vehicle Capable of Sustained and Controlled Flight." *International Micro Air Vehicle Conference and Competition (IMAV 2014).*
64. Phan, H. V., Au, T. K., & Park, H. C. (2016). "Clap-and-fling Mechanism in a Hovering Insect-like Two Winged Flapping-Wing Micro Air Vehicle." *Royal Society Open Science, 3*(12), 160746. doi:10.1098/rsos.160746
65. Galiński, C., & Żbikowski, R. (2005). "Insect-like Flapping Wing Mechanism Based on a Double Spherical Scotch Yoke." *Journal of The Royal Society Interface, 2*(3), 223-235. doi:10.1098/rsif.2005.0031
66. Combes, S. A. (2003). "Into Thin Air: Contributions of Aerodynamic and Inertial-Elastic Forces to Wing Bending in the Hawkmoth Manduca Sexta." *Journal of Experimental Biology, 206(17), 2999–3006.* doi:10.1242/jeb.00502
67. Hemsley, A. (2020, March 26). Amazing picture of rare white stork in flight over Hastings. Retrieved May 13, 2021, from https://www.hastingsobserver.co.uk/news/people/amazing-picture-rare-white-stork-flight-over-hastings-2519120

68. Hernandez, D. (2021, April 05). Hummingbirds can see colors that the human eye can't. Retrieved May 13, 2021, from https://www.popularmechanics.com/science/animals/a33322346/hummingbird-vision-see-new-colors/
69. (n.d.). Retrieved May 13, 2021, from https://www.biologicaldiversity.org/species/invertebrates/monarch_butterfly/
70. Dragonfly enzymes point to how they interact in the ecosystem: U of t research. (n.d.). Retrieved May 13, 2021, from https://www.utoronto.ca/news/dragonfly-enzymes-point-how-they-interact-ecosystem-u-t-research
71. O'Neill, M. (2019, December 20). Falcons see prey at over 200 mph – speed of a formula 1 race car. Retrieved May 13, 2021, from https://scitechdaily.com/falcons-see-prey-at-over-200-mph-speed-of-a-formula-1-race-car/
72. Revell, T. (2017, July 25). Maths explains how bees can stay airborne with such tiny wings. Retrieved May 13, 2021, from https://www.newscientist.com/article/2141802-maths-explains-how-bees-can-stay-airborne-with-such-tiny-wings/
73. Mao, S., Gang, D. "Lift and Power Requirements of Hovering Insect Flight." *Acta Mech Sinica* 19, 458–469 (2003). https://doi.org/10.1007/BF02484580
74. Rege, A. A. (2012). "CFD-based Aerodynamic Modeling to Study: Flight Dynamics of a Flapping Wing Micro Air Vehicle" (Unpublished doctoral dissertation).
75. Lehmann, F.-O., & Pick, S. (2007). "The Aerodynamic Benefit of Wing-Wing Interaction Depends on Stroke Trajectory in Flapping Insect Wings." *Journal of Experimental Biology, 210(8), 1362–1377.*
76. Wikimedia Foundation. (2021, September 3). Insect wing. Wikipedia. Retrieved October 2021, from https://en.wikipedia.org/wiki/Insect_wing.

77. Bug Basics: Wings. Bob's bugs. (n.d.). Retrieved October 2021, from https://www.bobs-bugs.info/bug-basics-wings/.
78. Hartenberg, R.S. & J. Denavit (1964). Kinematic synthesis of linkages, New York: McGraw-Hill
79. Four-bar linkage. Wikiwand. (n.d.). Retrieved October 2021, from https://www.wikiwand.com/en/Four-bar_linkage.
80. Simón Mata, A., Bataller Torras, A., Cabrera Carrillo, J. A., Ezquerro Juanco, F., Guerra Fernández, A. J., Nadal Martínez, F., & Ortiz Fernández, A. (2016). "Analytical Methods for the Kinematic Analysis of Planar Linkages. Raven's Method." *Mechanisms and Machine Science*, 111–141. doi:10.1007/978-3-319-31970-4_3
81. Söylemez Eres. (2013). Mechanisms (4th ed.). METU.
82. Hanrahan, S., Photo of a *Manduca Sexta*, Texas A&M University, Department of Entomology, Insect Collection in College Station, Texas 2006.
83. Jantzen, B., Eisner, T. (2008). "Hindwings are Unnecessary for Flight but Essential for Execution of Normal Evasive Flight in Lepidoptera." *Proceedings of the National Academy of Sciences*, 105(43), 16636–16640. https://doi.org/10.1073/pnas.0807223105
84. Zhao, L., Deng, X. (2009). "Power Distribution in the Hovering Flight of the Hawk Moth Manduca Sexta." *Bioinspiration & Biomimetics*, 4(4), 046003. https://doi.org/10.1088/1748-3182/4/4/046003
85. Sims, T. "A Structural Dynamic Anaysis of a Manduca Sexta Forewing." Master's thesis, Air Force Institute of Technology, Wright-Patterson AFB, OH, March 2010. AFIT/GAE/ENY/10-M22.
86. BEAM188. (2017, July 14). Retrieved November 2021, from https://www.mm.bme.hu/~gyebro/files/ans_help_v182/ans_elem/Hlp_E_BEAM188.html
87. Shell181. (2017, July 14). Retrieved November 2021, from https://www.mm.bme.hu/~gyebro/files/ans_help_v182/ans_elem/Hlp_E_SHELL181.html

88. O'Hara, R. P. (2012). “The Characterization of Material Properties and Structural Dynamics of the Manduca Sexta Forewing for Application to Flapping Wing Micro Air Vehicle Design” Master’s Thesis, Air Force Institute of Technology.
89. Truong, T. V., Nguyen, Q.-V., & Lee, H. (2017). “Bio-Inspired Flexible Flapping Wings with Elastic Deformation.” *Aerospace, 4(3), 37.* doi:10.3390/aerospace4030037
90. Singh, B., & Chopra, I. (2008). “Insect-Based Hover-Capable Flapping Wings for Micro Air Vehicles: Experiments and Analysis.” *AIAA Journal, 46(9), 2115–2135*. doi:10.2514/1.28192